Circulation Aspects, Dynamical Mechanisms, and the Predictability of Summer Heatwaves over Iraq

Hasanain AL-Shamarti

München 2025

Circulation Aspects, Dynamical Mechanisms, and the Predictability of Summer Heatwaves over Iraq

Hasanain AL-Shamarti

Dissertation
der Fakultät für Physik
der Ludwig-Maximilians-Universität
München

vorgelegt von
Hasanain AL-Shamarti
aus Bagdad (Irak)

München, den 16. September 2025

Erstgutachter: Prof. Dr. Thomas Birner
Zweitgutachter: Dr. Hella Garny
Tag der mündlichen Prüfung: 14. November 2025

Contents

Abstract

Heatwaves are responsible for increased mortality, heightened energy demand, economic disruption, and other serious societal impacts. While heatwave events are a global concern, those affecting the Middle East, particularly Iraq, have received relatively little scientific attention. Understanding the dynamics and predictability of extreme summer heatwaves over Iraq presents a significant challenge due to the region's persistently high background temperatures and limited day-to-day variability. This thesis employs a comprehensive dynamical framework to identify the large-scale and regional drivers of heatwaves, classify their dominant circulation patterns, and evaluate their representation in Subseasonal to Seasonal (S2S) forecast models. The analysis emphasizes the complex interactions between midlatitude and tropical systems, Iraq's topographic complexity, and their combined role in shaping extreme temperature events over the region.

Using ERA5 reanalysis, heatwave events were found to be associated with the attenuation of the low-level jet (Shamal winds), which is maintained by strong pressure gradients between regional high- and low-pressure systems and shaped by the Zagros Mountains. Most of these events were linked to Rossby wave activity, which disrupts these pressure patterns. Additionally, the upper-level high-pressure systems embedded within these waves can enhance down-slope (Foehn-like) winds on the leeward side of the Zagros Mountains, contributing to localized surface warming.

The UNprecedented Simulated Extremes using ENsembles (UNSEEN) approach, which utilizes the large number of possible atmospheric evolutions generated by ensemble forecasts, facilitates the identification of numerous potential heatwave events. By investigating atmospheric chaos in S2S data, this approach further confirms the association between heatwaves and Rossby wave activity. It highlights that while baroclinic Rossby wave trains are often linked to heatwaves by disturbing the local pressure systems driving the Shamal winds, more barotropic configurations intensify surface temperatures through stronger subsidence and increased solar irradiation. In some cases, these barotropic patterns also strengthen the Shamal wind, advecting warmer air into the region and further reinforcing heatwave conditions. The UNSEEN analysis also identifies a tropical influence: the Indian summer monsoon (ISM) can indirectly modify upper-level flow and regional pressure gradients across the Middle East, reducing the cooling influence of the Shamal winds. Although ISM-related heatwave events are less common than those driven by Rossby wave activity, they still contribute significantly to extreme temperature episodes by altering the regional circulation and thermodynamic structure.

This thesis evaluates the representation of heatwave drivers in S2S models. Results show that events associated with large-scale circulation features, particularly Rossby waves, are predicted with moderate skill at extended lead times. The findings highlight the need to improve the representation of mesoscale and smaller-scale processes and their interaction with large-scale circulation in order to enhance heatwave forecasts in Iraq and the broader Middle East.

Zusammenfassung

Hitzewellen sind verantwortlich für erhöhte Sterblichkeit, gesteigerten Energiebedarf, wirtschaftliche Störungen und andere gravierende gesellschaftliche Auswirkungen. Während Hitzewellen ein globales Problem darstellen, haben Ereignisse im Nahen Osten, insbesondere im Irak, bisher relativ wenig wissenschaftliche Aufmerksamkeit erhalten. Das Verständnis der Dynamik und Vorhersagbarkeit extremer Sommerhitzewellen im Irak stellt aufgrund der dauerhaft hohen Hintergrundtemperaturen und der geringen tageszeitlichen Variabilität der Region eine besondere Herausforderung dar. Diese Arbeit verwendet einen umfassenden dynamischen Rahmen, um die großräumigen und regionalen Treiber von Hitzewellen zu identifizieren, ihre dominanten Zirkulationsmuster zu klassifizieren und ihre Abbildung in Subseasonal-to-Seasonal-(S2S)-Vorhersagemodellen zu bewerten. Die Analyse betont die komplexen Wechselwirkungen zwischen außertropischen und tropischen Systemen, der topografischen Komplexität des Irak und deren kombinierter Rolle bei der Entstehung extremer Temperaturereignisse in der Region.

Unter Verwendung der ERA5-Reanalyse wurde festgestellt, dass Hitzewellenereignisse mit einer Abschwächung des bodennahen Jets (Shamal-Winde) verbunden sind, der durch starke Druckgradienten zwischen regionalen Hoch- und Tiefdrucksystemen aufrechterhalten und durch das Zagros-Gebirge geformt wird. Die meisten dieser Ereignisse stehen im Zusammenhang mit Rossby-Wellen-Aktivität, die diese Druckmuster stört. Darüber hinaus können die in diese Wellen eingebetteten Hochdrucksysteme in höheren Atmosphärenschichten abwärtsgerichtete (Föhn-ähnliche) Winde auf der Leeseite der Zagros-Berge verstärken und so zu einer lokalen Erwärmung der Oberfläche beitragen.

Der Ansatz 'UNprecedented Simulated Extremes using ENsembles' (UNSEEN), der die große Anzahl möglicher atmosphärischer Entwicklungen aus Ensemblevorhersagen nutzt, ermöglicht die Identifizierung zahlreicher potenzieller Hitzewellenereignisse. Durch die Untersuchung atmosphärischen Chaos in S2S-Daten bestätigt dieser Ansatz zusätzlich die Verbindung zwischen Hitzewellen und Rossby-Wellen-Aktivität. Er zeigt, dass barokline Rossby-Wellenzüge oft mit Hitzewellen in Verbindung stehen, indem sie lokale Drucksysteme stören, die die Shamal-Winde antreiben, während barotrope Konfigurationen die Oberflächentemperaturen durch stärkere Subsidenz und erhöhte Sonneneinstrahlung intensivieren. In einigen Fällen verstärken diese barotropen Muster auch die Shamal-Winde, indem sie wärmere Luft in die Region transportieren und die Hitzewellenbedingungen weiter verstärken. Die UNSEEN-Analyse identifiziert zudem einen tropischen Einfluss: Der indische Sommermonsun (ISM) kann indirekt den Strömungsverlauf in höheren Atmosphären-

schichten und regionale Druckgradienten im Nahen Osten verändern und dadurch die kühlende Wirkung der Shamal-Winde reduzieren. Obwohl Hitzewellenereignisse, die mit dem ISM zusammenhängen, seltener sind als solche, die durch Rossby-Wellen-Aktivität verursacht werden, tragen sie dennoch wesentlich zu extremen Temperaturepisoden bei, indem sie die regionale Zirkulation und thermodynamische Struktur verändern.

Diese Arbeit bewertet die Abbildung der Hitzewellentreiber in S2S-Modellen. Die Ergebnisse zeigen, dass Ereignisse, die mit großräumigen Zirkulationsmustern, insbesondere Rossby-Wellen, verbunden sind, über längere Vorhersagezeiträume mit moderater Genauigkeit prognostiziert werden. Die Ergebnisse unterstreichen die Notwendigkeit, die Abbildung mesoskaliger und kleinerer Prozesse sowie deren Wechselwirkung mit der großräumigen Zirkulation zu verbessern, um die Vorhersage von Hitzewellen im Irak und im weiteren Nahen Osten zu optimieren.

Acronyms

AMO Atlantic Multidecadal Oscillation

AZM Atlantic Zonal Mode

ECMWF European Centre for Medium-Range Weather Forecasts

ENSO El Niño–Southern Oscillation

EDA Ensemble of Data Assimilation

EFS Ensemble Forecast Systems

ERA5 ECMWF Reanalysis V5

ETCCDI Expert Team on Climate Change Detection and Indices

GHI Geopotential Height Anomalies Index

HWDI Heat Wave Duration Index

HWMID Heatwave Magnitude Index Daily

IOD Indian Ocean Dipole

IFS Integrated Forecast System

IPCC Intergovernmental Panel on Climate Change

ISM Indian Summer Monsoon

ITCZ Intertropical Convergence Zone

JJA June, July, and August

LLJ Low-Level Jet

MENA Middle East and North Africa

MJO Madden–Julian Oscillation

MSLP Mean Sea Level Pressure

NAO North Atlantic Oscillation

NWP Numerical Weather Prediction

PDO Pacific Decadal Oscillation

PV Potential Vorticity

QSAH Quasi-Stationary Anticyclonic High

RMSE Root Mean Squared Error

RST Red Sea Trough

RWB Rossby Wave Breaking

RWP Rossby Wave Propagation

S2S Subseasonal-to-Seasonal

SL Sudanese Low

SNAO Summer North Atlantic Oscillation

SST Sea Surface Temperature

SWI Shamal Wind Index

TEJ Tropical Easterly Jet

TCC Total Cloud Cover

TLI Thermal Low Index

Tmax Daily Maximum Temperatures

MSLP Mean Sea Level Pressure

UNSEEN UNprecedented Simulated Extremes using ENsembles

WYMI Webster and Yang Monsoon Index

Chapter 1

Introduction

This chapter presents an overview of the atmospheric processes contributing to heatwave evolution, including upper-level circulation patterns relevant to the Middle East, Rossby waves, large-scale teleconnections, subsidence, radiative forcing, and land-atmosphere feedbacks.

1.1 Relevance

Heatwaves can have a massive impact on the economy, agriculture, infrastructure, energy, natural ecosystems, and human health (Barriopedro et al., 2023; IPCC, 2022; Hirsch and King, 2020; WMO, 2020; Raymond et al., 2020; Perkins, 2015; Kovats and Hajat, 2008). They are sometimes referred to as 'silent killer' since their effects can substantially raise mortality and morbidity (Loughnan, 2014). For instance, heatwaves in Western Europe in 2003 and Russia in 2010 caused approximately 70,000 and 54,000 deaths, respectively (Rousi et al., 2022; Zhang et al., 2020; Christidis et al., 2015).

Similarly, just as heatwaves have had devastating impacts in Europe, they also pose significant challenges in the Middle East, leading to severe societal consequences (Hochman et al., 2022).

The Middle East and North Africa (MENA) region stands among the most vulnerable areas to climate change impacts, as various reports from the Intergovernmental Panel on Climate Change (IPCC) emphasize. This vulnerability is exemplified by the increasing frequency, duration, and intensity of heatwaves across the region, with daily maximum temperatures reaching up to 56° C by model projections for the "business-as-usual" climate change scenario in some Gulf cities (Zittis et al., 2021; Almazroui, 2020). Furthermore, Ntoumos et al. (2020) found that regional annual mean temperature increases by about 0.2°C per decade, based on historical (1950–2005) and scenario simulations (2006–2018

under RCP2.6, RCP4.5, and RCP8.5), compared with observations and reanalysis data for 1980–2018.

According to Francis and Fonseca (2024), shifts in atmospheric circulation have significantly impacted boreal summer climate changes in the MENA region over the past four decades and are likely to continue. For example, increasing temperatures tend to be associated with higher levels of moisture and dust, resulting from the Arabian Peninsula and Sahara thermal lows being closer and a northward migration of the Intertropical Convergence Zone (ITCZ). With the intensified thermal low around the Gulf, these shifts enhance the pressure gradient with the subtropical high over the northern Arabian Peninsula strengthening local low-level jet (Francis and Fonseca, 2024).

The climate-change-related increases in temperature extremes are associated with socio-economic implications, like a projected increase in mortality risks in MENA regions. Projections based on the Coupled Model Intercomparison Project-sixth phase (CMIP6) and Shared Socioeconomic Pathways (SSPs) suggest that by 2100, heat-related mortality rates could increase significantly, presenting a substantial risk to public health (Hajat et al., 2023, Fig.2). Similarly, the Coordinated Regional Climate Downscaling Experiment (CORDEX) in RCP4.5 and RCP8.5 scenarios for the period 2006-2010 suggest that excessive heat stress substantially increases the risk of mortality (Ahmadalipour and Moradkhani, 2018). For Iraq specifically, these projections under RCP8.5 scenarios estimate maximum temperatures to average 46.1 $\pm$ 1.3° C between 2020–2049 and 49.8 $\pm$ 1.6° C between 2070–2099 (Varela et al., 2020, Table S2). In response, researchers are actively examining the risks of extreme heat, aiming to address the environmental and public health challenges posed across the region (Neira et al., 2023; Waha et al., 2017; Feitelson and Tubi, 2017; Sowers et al., 2011).

1.2 Physical drivers of Heatwave

Numerous atmospheric processes can influence the conditions of heatwave events and severity, as well as intensify heatwaves, including large-scale teleconnections, planetary waves, synoptic systems, interactions with soil moisture and land surfaces, land-ocean interactions, and climate variability (Horton et al., 2016; Perkins, 2015). Barriopedro et al. (2023) summarized the major heatwave processes in the mid-latitudes, which are associated with large-scale atmospheric circulation patterns, as illustrated in the schematic shown in Figure 1.1. We summarize the main processes relevant to our study as follows:

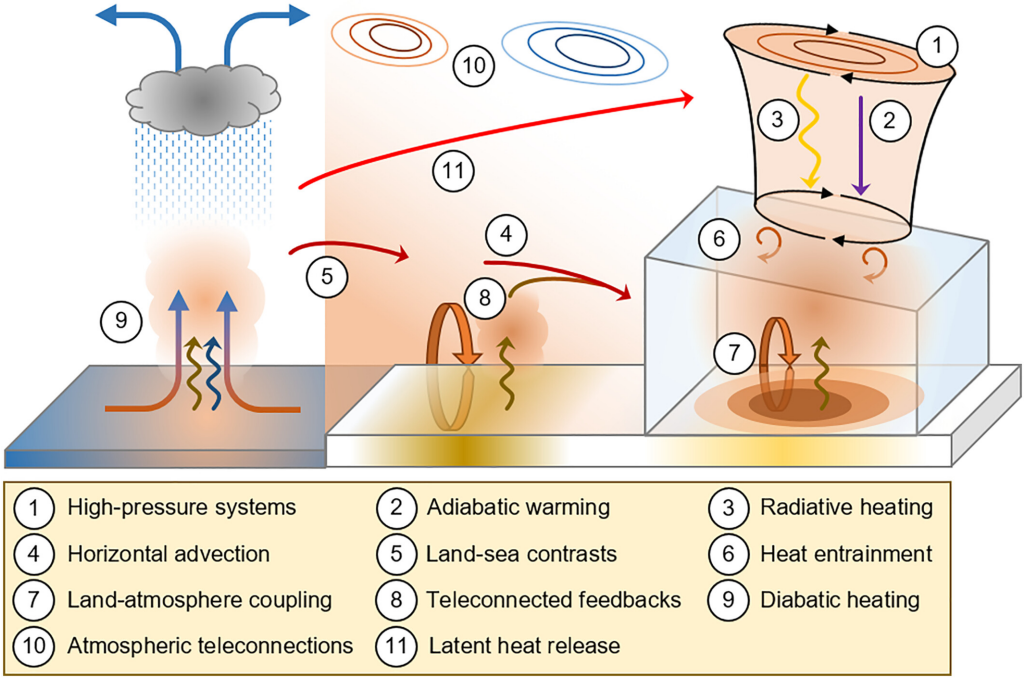

Figure 1.1: Schematic summarizing the large-scale to regional drivers of heatwaves. On the right side, the red shading within the box represents the regional heatwave, while the box itself outlines the spatial domain and the atmospheric boundary layer. High-pressure systems such as blocking highs, subtropical ridges, or Rossby wave packets (1, black anticyclonic vortices in the figure) contribute to heatwave development through several interacting processes. They induce adiabatic warming via large-scale subsidence (2, purple arrow), increase radiative heating due to clear skies (3, yellow arrow), and promote warm air advection (4, dark red arrow), often influenced by land–sea temperature contrasts (5, dark red arrow). These processes drive near-surface warming and enhance the deep and warm atmospheric boundary layers, which adjust heat exchange with the overlying free troposphere (6, spiral arrows). Heatwaves could be further amplified by local land–atmosphere interactions, particularly soil moisture feedbacks (7, orange loop), where dry soils (brown shading) reduce latent heat flux and enhance sensible heating (brown arrow). Additionally, warm air advection may be intensified by upwind drought conditions through teleconnected feedbacks (8, brown-red arrow), supplying even hotter air masses to the region. Remote diabatic heating sources, such as tropical convection, Sea Surface Temperature (SST) anomalies, and associated latent heat fluxes (9, blue arrow), can initiate Rossby wave trains or Circumglobal Teleconnection patterns (10, colored contours) that reinforce the high-pressure system linked to the heatwave. Latent heat release from moist ascending air and atmospheric rivers also contributes to diabatic heating, strengthening the upper-tropospheric anticyclone collocated with the heatwave (11, light red arrow) (Barriopedro et al., 2023).

1.2.1 Atmospheric Circulation as a Driver of Heatwaves

Atmospheric circulation plays a central role in driving heatwave events (Barriopedro et al., 2023; Faranda et al., 2023). Large-scale circulation patterns influence a range of atmospheric phenomena across various scales, and understanding their physical mechanisms is crucial for identifying the drivers of heatwave events. The most relevant circulation features linked with heatwaves include:

High-Pressure Systems (Anticyclones, Blocking, Ridges)

Persistent high-pressure systems (anticyclones) are a main source of many heatwave events (Wang et al., 2018). These anticyclones, characterized by upper-level convergence and subsiding air, lead to surface warming through adiabatic compression (Dai et al., 1997). The associated subsidence with this feature suppresses cloud formation, enhancing incoming solar radiation and reinforcing extreme surface heating. When such systems persist for several days, they prolong heatwave conditions.

In particular, blocking highs (quasi-stationary high-pressure systems associated with a meandering jet stream) can inhibit the usual west-to-east flow of weather systems, leading to a stable structure of the atmosphere (Woollings et al., 2018; Egger, 1978). These structures are linked to some of the most severe heatwaves in recent decades, such as those in Europe (2003) and Russia (2010) (Wolf et al., 2018).

These high-pressure systems are mostly embedded in Rossby waves, which are large-scale meanders in the mid-latitude westerlies that transport energy and heat. When these waves amplify and become quasi-stationary, they often lead to long-lasting high-pressure ridges that promote warm air advection, thereby contributing to heatwave evolution (Rodwell and Hoskins, 1996; Hoskins and Woollings, 2015). During summer, the Atlantic and African-Asian jets act as waveguides, trapping these waves within certain latitude bands (Screen and Simmonds, 2014; Ambrizzi and Hoskins, 1997).

Amplified Rossby waves with zonal wavenumbers 5–8 can form slow-moving anticyclones, which suppress cloud formation and increase surface heating (Fragkoulidis et al., 2018; Fragkoulidis, 2022). These ridges enhance subsidence and block cooler air, intensifying and prolonging heatwaves. Regional features like mountain ranges can strengthen these stationary patterns, while dry soils under these ridges reduce evaporative cooling, further amplifying temperatures.

Overall, amplified Rossby waves guide persistent high-pressure systems that play a key role in driving intense and long-lasting heatwave events in the Northern Hemisphere.

Synoptic Systems and Boundary Layer Processes

Synoptic-scale systems such as upper-level ridges and cut-off highs modulate mesoscale boundary layer processes, thereby influencing surface temperature extremes (McGregor, 2024). When these systems persist, they can reinforce local high-pressure structures, enhancing vertical motion and adiabatic warming near the surface. These upper patterns could be producing pressure gradients between persistent highs and lows, strengthening low-level wind flow, which can lead to warm-air advection into the region (Ventura et al., 2023). In addition, moisture transported by these flows from adjacent water bodies can increase long-wave radiation absorption, further elevating surface temperatures (Yang et al., 2020).

1.2.2 Climate Variability and Teleconnections

Initially, **climate variability** spans a range of time scales—from weekly to decadal fluctuations—and can modulate the frequency, intensity, and duration of heatwaves. Meanwhile, the term **teleconnections** describes statistically significant correlations between large-scale atmospheric circulation patterns and regional climate variability on timescales ranging from seasonal to interdecadal (IPCC, 2023; Alexander et al., 2002; Trenberth and Hurrell, 1994). These concepts are widely applied in heatwave research to assess how remote phenomena, such as sea surface temperature anomalies or tropical convection shifts, influence regional atmospheric dynamics and extreme temperature events. Below, we highlight the major teleconnection patterns that have received considerable attention in the literature and are significantly associated with heatwave evolution in this thesis:

North Atlantic Oscillation (NAO)

The North Atlantic Oscillation (NAO) is widely discussed in this thesis due to its significant role in climate variability and its relevance to our analytical perspective, particularly regarding the timescales of atmospheric features such as Rossby waves, which are considered key drivers of heatwaves. It is considered an important teleconnection in the mid-latitudes due to its association with changes in wind direction, heat and moisture transport, and the frequency and intensity of storms (Lehmann and Coumou, 2015). As a result of the seesaw between the Icelandic low and Azores high atmospheric systems, NAO index is defined by the normalized Sea Level Pressure (SLP) anomalies between these pressure systems (Barnston and Livezey, 1987). When the meridional pressure gradient over the North Atlantic is strong, in particular, a strong high-pressure system over the Azores, and a deep low-pressure system near Iceland, the NAO index is NAO^+ which enhances eastward flow across the North Atlantic. This pressure gradient strengthens the westerly winds, which channel

storms from the Atlantic across North America and Europe. As a result, during the winter season, northern Europe and the eastern United States typically experience milder, wetter conditions with increased storm activity. In contrast, regions such as northern Canada, Greenland, and southern Europe often face colder and drier winters (Luo and Cha, 2012). This NAO phase during the summer is more often associated with weakened westerlies and a meandering jet stream, favoring the development of blocking highs over Europe. These persistent high-pressure systems can lead to clear skies, subsidence and reduced atmospheric circulation, all of which are conducive to heatwave conditions (Luo et al., 2023; Kautz et al., 2022; Kueh and Lin, 2020). During the summertime, the northward shift of subtropical high-pressure systems can lead to drier conditions across the Middle East by inhibiting large-scale moisture transport into the region (Cullen et al., 2002).

Conversely, with NAO^-, the pressure gradient between the Azores high and the Icelandic low is reduced, leading to weakened west-to-east zonal flow across the North Atlantic. During this phase in wintertime, the weather tends to be cold and dry in northern Europe, while warm and wet conditions are more likely in southern Europe (Hurrell and Deser, 2009). In summer, the NAO pattern shifts into what is commonly referred to as the Summer North Atlantic Oscillation (SNAO), which exhibits spatial and temporal variability between early and late summer. The SNAO is displaced poleward and tilted with more action over Greenland and north-western Europe. In general, the variant phases of SNAO correspond to a northward (southward) shift of the jet stream, which extends its impact across Eurasia and East Asia (Dunstone et al., 2023). In the late summer, the SNAO tends to be associated with the surface temperature anomalies and local pressure systems over the eastern Mediterranean, which could extend their influences over the Arabian Peninsula (Chronis et al., 2011). These influences are linked to a southward shift of the southern center of the SNAO, positioned farther east. This southward shift enhances low-level convergence near the Asian jet entrance, triggering a quasi-stationary Rossby wave train that alters East Asian summer circulation and leads to temperature anomalies across the region (Sun et al., 2008).

Other Relevant Teleconnections

The Indian Ocean Dipole (IOD), Pacific Decadal Oscillation (PDO), Atlantic Multidecadal Oscillation (AMO), and Atlantic Zonal Mode (AZM) are widely recognized as major climate drivers influencing large-scale coupled ocean–atmosphere phenomena (Wang et al., 2024; Singh et al., 2020). These oscillations play a crucial role in modulating the Indian Summer Monsoon (ISM) as well as convection and rainfall patterns in other tropical regions, such as the ITCZ (Madolli et al., 2022). By modifying the Surface Temperature SST conditions and circulation features over the Indo-Pacific domain; these climate drivers significantly affect the variability of ISM. For example, the oscillating phases of IOD are significantly linked with ISM activity through variations in SST between the western and

eastern Indian Ocean (Madolli et al., 2022). During a positive IOD phase, warmer water in the western Indian Ocean and cooler water in the eastern Indian Ocean lead to increased convection and enhanced rainfall over India. Conversely, a negative IOD phase, characterized by cooler water in the west and warmer water in the east, can inhibit ISM activity, contributing to drought and heatwave conditions (Chakraborty and Singhai, 2021; Pothapakula et al., 2020).

Indeed, the interaction between the ISM and Rossby waves tends to enhance heatwave occurrence. One proposed mechanism involves the anticyclonic systems embedded within these Rossby waves, typically manifest in the mid-troposphere, effectively blocking the northward transport of moist air from the Indian Ocean (Fragkoulidis, 2022). During ISM break periods, the low-level ISM trough shifts northward, reducing moisture convergence and rainfall over the Indian subcontinent, resulting in less cloud cover and increased solar radiation at the surface (Rao et al., 2016). Concurrently, persistent high-pressure systems further develop in the mid-troposphere, which inhibit convective activity and enhance subsidence (Roxy et al., 2015). This combination of factors promotes surface heating and contributes to heatwave conditions during the monsoon season.

This interaction between the ISM and Rossby waves could influence spanning toward the Middle East. As a result, Iraq may experience anomalous subsidence, clear skies, and warm air advection, particularly during ISM break phases, thereby favoring the development and persistence of heatwaves over the region.

1.2.3 Local Factors and Modifiers

Topography and Local Geography

Iraq's complex topography—including mountain ranges, valleys, and desert basins (see Section 1.3 for more details)-plays a crucial role in modulating the intensity of heatwaves. These features can generate localized wind patterns, such as down-slope (foehn-like) winds, that generate heat in basins and valleys, amplifying temperature extremes (Keikhosravi et al., 2020).

The mountain locations can significantly influence atmospheric circulation patterns, thereby affecting the intensity and distribution of heatwave across regions. In the mid-latitudes, mountains that lie along or near the jet stream axis interact with upper-level atmospheric flow and contribute to the formation of stationary wave patterns. In this context, mountains may redirect the jet stream either equatorward or poleward (Jiménez-Esteve and Domeisen, 2022). Upstream of high elevation mountain ranges (like Zagros Mountains), the interaction often leads to a deceleration of zonal winds and an increased frequency of atmospheric blocking events—conditions favorable for the development and

persistence of heatwaves. Conversely, downstream or equatorward of midlatitude topography, the upper-level jet typically accelerates, which results in more transient weather patterns and a reduced likelihood of prolonged heat extremes (Jiménez-Esteve and Domeisen, 2022).

Coastal regions also experience modified heatwave dynamics due to the moderating effect of sea breezes and land–sea thermal contrasts (Du et al., 2024). These circulations, driven by daytime heating differences between land and sea, can reduce daytime temperatures near the coast by transporting cooler marine air inland. However, weakened sea breezes or suppressed circulation may lead to stronger net surface heat flux over coastal waters, mainly due to increased shortwave radiation and reduced latent heat loss in arid or semi-arid regions like southern Iraq, which ultimately contributes to sea surface temperature warming (Chatterjee et al., 2022). This mechanism effectively prolongs and intensifies the heatwave over countries surrounding the Arabian/Persian Gulf (Shaltout and Eladawy, 2024).

1.3 Geographical and Climate Characteristics of Iraq

Iraq is characterized by a diverse topography, with mountains in the north and northeast forming a crescent shape and covering around 5% of the country's land area (Fig. 1.2a). The region extending from the mountains in northern Iraq to the central areas is classified as an island plateau. The region between the Euphrates and Tigris rivers, known as Mesopotamia, is classified as an alluvial plain (Muslih, 2014). Further, the south and west areas are classified as desert areas, which cover around 40% of the Iraqi land area. This final area has serious hazards that are caused by poor drainage and salinity (FAO, 2008).

This topographic variation strongly influences the climate characterizations. In summer, a strong subtropical high-pressure system dominates with hot and dry weather when the mean maximum temperature is approximately 48-50°C in the hottest months. Due to the qualitative variation of pressure systems throughout the year, the Köppen classification of climate has divided Iraqi climate into three types: Mediterranean climate in mountain regions, Subtropical Steppe climate in high terrain regions, which locate southern mountain regions, and Subtropical Desert climate in the middle and south of Iraq (Malinowski, 2002).

1.4 Summer Climatology Aspects

The seasonal variability of Iraq's climate is a critical driver of its weather patterns, particularly in shaping extreme events such as heatwaves. Beyond the direct influence of Iraq's topography, large-scale atmospheric circulation systems also play a substantial role

in modulating mesoscale weather patterns over Iraq and its surrounding regions. The main pressure system important for the Iraqi climate is the low-level thermal low-pressure system (in some literature called the **Zagros Mountains trough**), which may be intensified by the ISM extending to further north of the Arabian peninsula (Fig. 1.2b, see contour lines). This combination of thermal low pressure and orographic effects contributes to the intensification of surface temperatures in southern Iraq during the summer months (Fig. 1.2b, see shading). Further, the topographical features surrounding Iraq, such as the Zagros Mountains to the east and the deserts to the west, facilitate the development of Low-Level Jet (LLJ), particularly the **Shamal wind** (Figure 1.2 c). The Shamal* winds, a regional phenomenon characterized by strong northwesterly winds, play a crucial role in transporting heat and moisture, significantly impacting Iraq's summer climate. Under certain circumstances, Shamal winds can either advect hot air masses, exacerbating heatwaves, or inhibit ventilation, leading to stagnant conditions that intensify dust storms, reduce visibility, and prolong extreme heat events. Indeed, the strengthening pressure gradient between the local high-pressure system (associated with persistent subsidence) over the Levant and the thermal low over southern Iraq, typically the primary driver of the Shamal winds, along with the region's complex topography, further contributes to the intensification of the Shamal winds (Yu et al., 2016; Rao et al., 2003; Perrone, 1979, see Chapter 3 for more details).

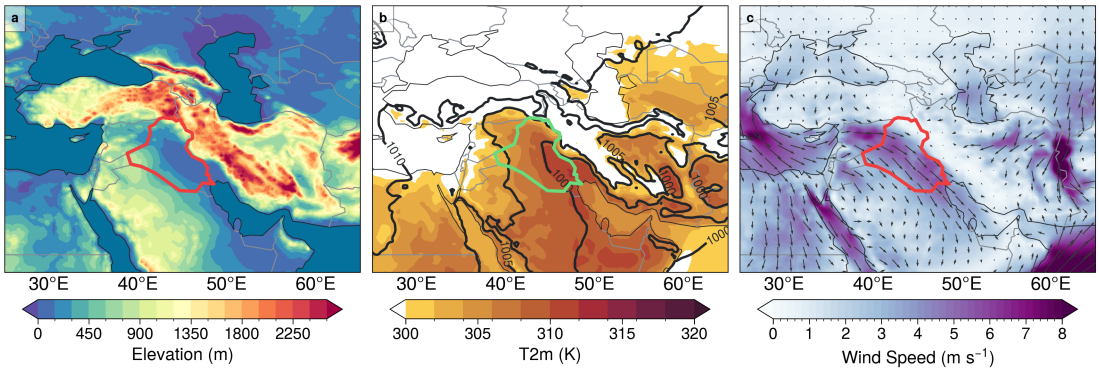

Figure 1.2: The climatology of the summer season (June, July, and August) over Iraq for the period 1980–2022 is presented as follows: a) Elevation of topography; b) Daily mean temperature (shading) and the Mean Sea Level Pressure (MSLP) (contours, units: hPa); c) Wind speed (shading) and wind direction (arrows). These figures were generated using reanalysis data from ERA5 [see section 2.1]. The daily means were calculated by resampling the hourly data.

Indeed, these characterizations are associated with the dominant features of summer atmospheric circulation that govern the climate of Iraq. Figure 1.3 illustrates these features that influence Iraq and the surrounding regions during summer.

*Shamal is Arabic and means north, thereby referring to the general northerly flow in the region.

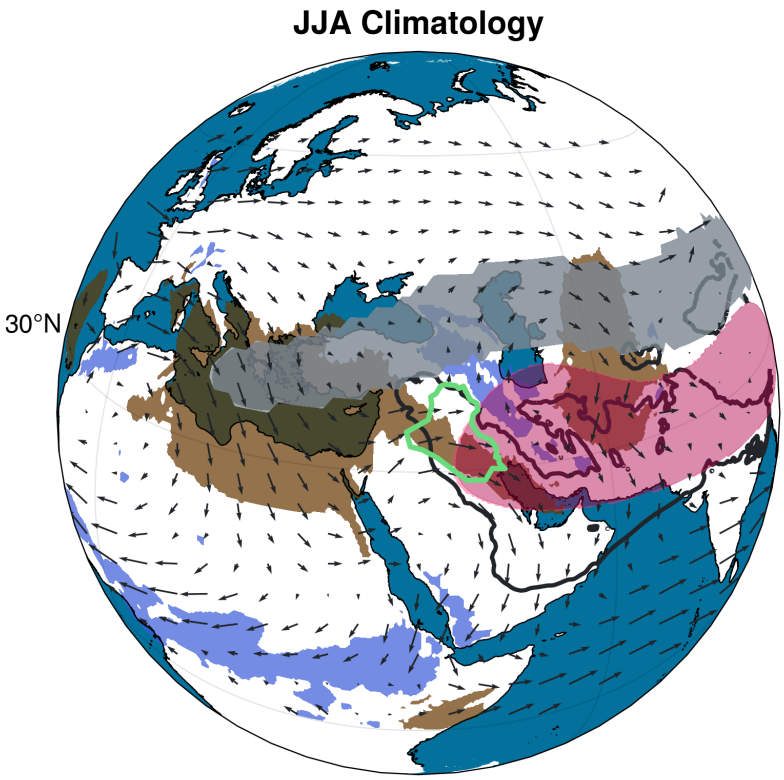

Figure 1.3: Climatology of the summer season (June, July, and August) showing the following variables: red shading shows zonal anomalies of geopotantial height at 200 hPa exceeding 98 m indicating the monsoon anticyclone, the black contour line shows -8 hPa value of the zonal anomalies of MSLP indicating the low-level monsoon system, gray shading shows the latitudinal differentiation of Potential Vorticity (PV) (PV, units: 1 PVU) at the 350K level indicating Subtropical jet stream, arrows show the total horizontal wind components (u and v) at 700 hPa, and blue/brown shading show vertical velocity with units: Pa/s at 700 hPa, blue refers the ascending indicating ITCZ region and brown refers to descending indicating subtropical subsidence. Spatial rolling means are used for (PV) and (w) to smooth the values that are shown in the plot. The green border indicates Iraq, and the dark blue indicates oceans. All data were sourced from ERA5 reanalysis [see section 2.1].

The figure highlights the **Hadley cell**, represented by ascending and descending air masses (blue and brown shading). The Hadley cell extends from the equator to approximately 30–40° latitudes. On its poleward edge, subsidence dominates over regions such as Iraq, the Levant, and North Africa. This descending motion is a key driver of **adiabatic warming**, whereby air compresses as it sinks, increasing surface temperatures and contributing to the extreme heat experienced in these regions during the summer.

In contrast, near the equator, the ascending branch of the Hadley cell promotes convective

activity. Here, the convergence of trade winds triggers thunderstorms along the ITCZ. This convective zone strengthens the rising air masses (blue shading) in the tropics, which then move poleward in the upper troposphere. As these air masses move poleward, Earth's rotation causes them to deflect to the right in the Northern Hemisphere due to the **Coriolis effect**, contributing to the formation of the **Subtropical Jet Stream** (gray shading). During the summer, this jet stream weakens and expands across Eurasia (Chen et al., 2017; LU, 2004), creating conditions that favor the development and propagation of Rossby waves. These large-scale planetary waves are guided by the jet stream and play a pivotal role in steering mid-latitude weather systems.

The subtropical high-pressure belt, a lower-tropospheric feature formed by large-scale subsidence due to the conservation of angular momentum and the Coriolis effect, dominates the subtropics. During the summer, deep convective heating over South Asia associated with the monsoon circulation leads to the development of the **upper-level monsoon anticyclone** (highlighted in red), which significantly influences upper-tropospheric circulation. The monsoon system, a major synoptic feature of the Northern Hemisphere summer, is characterized by cyclonic circulation in the lower troposphere and anticyclonic flow in the upper troposphere. It generates expansive **thermal low-pressure systems** (contour lines), which significantly impact the regional climate. These upper-level circulation features play a critical role in shaping atmospheric patterns across the Middle East, while orographic effects, particularly those associated with surrounding high terrain, contribute to the intensification of surface temperatures in southern Iraq during the summer months.

1.5 Scope of this Thesis

This thesis examines the physical mechanisms and predictability of summer heatwaves in Iraq. Previously, we introduced the main factors that could have a crucial role in heatwave evolution. In winter, large-scale circulation features—such as the upper-level jet stream—play a dominant role in mid-latitude atmospheric dynamics, often interacting with variability modes like the NAO, planetary wave, and troposphere-stratosphere coupling. In contrast, during summer, the influence of these features becomes less pronounced in subtropics due to the poleward shift and weakening of the upper-level jet, while tropical dynamics exert a greater influence on subtropical weather patterns. To investigate these summertime dynamics and their connection to regional heatwave events, this thesis employs ERA5 reanalysis data and S2S forecast datasets from the European Centre for Medium-Range Weather Forecasts (ECMWF) model.

The geographical scope of this study is centered on Iraq and its surrounding regions, particularly those influenced by large-scale dynamics such as Rossby waves and the Indian summer monsoon, as well as local features like the Shamal winds or downsloping winds that contribute to regional heatwave evolution. This focus aligns well with the horizontal

resolution (≈33 km) of the reanalysis and forecast datasets used, which is sufficient to capture both large-scale circulation and regional meteorological phenomena.

For the ERA5 reanalysis data, atmospheric variables at multiple pressure levels were utilized to investigate the vertical structure of large-scale circulation, to examine baroclinic and barotropic wave characteristics. Cross-sectional analyses were also conducted along high-elevation areas, particularly the Zagros Mountains, to examine vertical advection, the role of orographic subsidence in the adiabatic warming process, and horizontal flow structure. In addition, key thermodynamic variables such as surface net thermal radiation were analyzed to assess their interaction with dynamic atmospheric mechanisms.

For the S2S data, our approach aligns with the primary objective of the S2S initiative, to improve forecasting skill on the sub-seasonal to seasonal timescale, which bridges the gap between short- to medium-range weather forecasts (up to 10 days) and seasonal predictions. We use this dataset both to assess the sub-seasonal forecast skill for heatwave events over the region and to compare the large-scale circulation structures with reanalysis data. Additionally, the natural atmospheric chaos, which is present in the ensemble spread, is further exploited through the UNSEEN approach, which provides a much larger sample size, to identify and better understand potential large-scale physical drivers of heatwaves. This approach provides a coherent view of Rossby wave patterns and their structures, as well as their interaction with the Indian Summer Monsoon. It also highlights how the evolution of the monsoon system can contribute to the evolution of the dominant pressure patterns over Iraq.

While the influence of large-scale teleconnection patterns, such as the NAO, is considered in this thesis, ocean-atmosphere feedbacks are not explored in detail. Additionally, due to data constraints, the study does not employ regional climate models or high-resolution simulations, though these are recommended for future research.

1.6 Major research question

What are the dynamical drivers and predictability characteristics of extreme heatwave events over Iraq, and how do large-scale and regional processes interact to produce these events?

The analysis of heatwaves over Iraq is particularly challenging because the region experiences extremely high summer temperatures combined with relatively low day-to-day variability. This makes it more difficult to distinguish extreme heatwave events from the already hot background when using percentile-based thresholds. Moreover, Iraq's complex topography enhances mesoscale circulations, which shape low-level atmospheric conditions. These small-scale dynamics add complexity to analyzing heatwaves within a dy-

namical framework. However, this region is influenced by multiple interacting phenomena that contribute to heatwave evolution, including latitudinal energy transmission by Rossby waves, upper-level anticyclones associated with the high-elevation Zagros Mountains, and ISM activity modifying synoptic-scale pressure patterns. Consequently, the main question arises: What are the primary dynamical drivers of summer heatwaves over Iraq?.

However, the predictability of extreme heatwave events over Iraq remains challenging due to the interaction between large-scale and mesoscale processes. For example, features like Rossby wave patterns and subtropical anticyclones influence the broader circulation and are generally associated with longer predictability timescales. In contrast, regional factors (i.e., Iraq's complex topography) such as Shamal winds, terrain-induced flows, and localized subsidence, strongly influence the local temperature response tends to have less predictable timescales. This combination of drivers, each with distinct spatial and temporal characteristics, results in a range of predictability timescales. Therefore, assessing the predictability of the dynamical features associated with heatwaves is essential for evaluating forecast model performance and improving our understanding of heatwave evolution. This leads to the key question: what are the predictability characteristics of extreme heatwave events over Iraq?.

Indeed, large-scale circulation arises from numerous interacting phenomena that dynamically influence weather patterns across multiple scales (Vallis, 2017; Wallace and Hobbs, 2006; Holton, 2004). This motivates an exploration of how key heatwave drivers, such as Rossby waves and the ISM, interact with regional features like the Shamal winds. This leads to the central question: how do large-scale and regional processes interact to produce these events?.

However, this primary question gives rise to additional research questions, which will be addressed in the final chapter as their answers are closely linked to the resolution of this main question.

Thesis outline The thesis is structured into the following chapts:

- **Definition and Detection of Heatwaves**
  This chapter defines heatwaves within the selected target area and introduces both reanalysis and observational datasets. The reliability and consistency of detected events are evaluated against station data, establishing a robust climatology of extreme heat events.
- **Characterization and Classification**
  The third chapter explores the duration, intensity, and spatial extent of ERA5-based heatwave events. Events are classified based on dynamic features, including anticyclonic anomalies and Rossby wave structures, using clustering techniques.
- **Predictability and Case Study Analysis**

This chapter evaluates the forecast skill of ECMWF S2S data using root mean square metric and threshold-based approaches. A selected case study is analyzed in depth, comparing S2S forecasts with ERA5 to assess predictive accuracy and underlying dynamics.

- **UNprecedented Simulated Extremes using ENsembles (UNSEEN) Approach and Mechanism Filtering**

  This chapter investigates S2S ensemble forecasts using the UNSEEN approach to identify possible and historically unobserved heatwave events. By the atmospheric chaos that is represented in the ensemble spread, UNSEEN method reveals alternative physical drivers and circulation patterns that may not appear in the ERA5 reanalysis. The goal is to provide a coherent understanding of heatwave variability beyond the primary mechanisms identified from past observations.

- **Conclusion and Discussion**
  The final chapter summarizes the key findings, highlights the dominant physical drivers and limitations of the study, and outlines recommendations for future research directions.

Chapter 2

Data and Methodology

In this chapter, we present the datasets used in the first part of this thesis and outline the methodology for identifying heatwaves. Additionally, we provide an overview of key findings from the observational data analysis.

2.1 Reanalysis Data

Our analyses are based on ERA5 reanalysis data produced by the European Center for Medium-Range Weather Forecasts (ECMWF, see Hersbach et al., 2020). ERA5 is built on the Integrated Forecast System (IFS) Cy41r2, which was introduced in 2016. This system integrates a decade of advancements in model physics, dynamics, and data assimilation. A major improvement is the enhanced horizontal resolution of 31 km, significantly higher than the 80 km of ERA-Interim. Additionally, ERA5 provides hourly outputs and includes an uncertainty estimate derived from an ensemble, updated every three hours at half the horizontal resolution. The ERA5 system features an improved data assimilation methodology, utilizing a hybrid incremental 4D-Var system (Bonavita et al., 2016).

To diagnose heatwaves, we use hourly 2-metre temperatures (T2m) at a horizontal resolution of $0.25° \times 0.25°$ for the months May through September within the period 1980-2022. The highest daily temperatures were recorded during July and August at approximately 318 K and averaged around 310 K. To study the large-scale circulation environment of the heatwaves, we also use 6-hourly data of geopotential heights and wind fields at multiple pressure levels, as well as mean sea level pressure (MSLP). These data are complemented by thermodynamic fields, including surface radiation and heat fluxes, sea surface temperature (SST), total cloud cover, and total column water.

2.2 Methodology

2.2.1 Background of Heatwave Definitions

Heatwaves are prolonged periods of exceptionally high temperatures that exceed extreme thresholds, posing significant environmental and societal challenges. According to the International Meteorological Vocabulary of the World Meteorological Organization (WMO), a heatwave is characterized by a significant warming of the air or an invasion of warm air over a large area, persisting for several days to a few weeks (WMO, 1992). Similarly, the Glossary of Meteorology by the American Meteorological Society (AMS) defines a heatwave—also referred to as a hot wave or warm wave—as a period associated with thermal discomfort, often exacerbated by high humidity (AMS, 2025). The IPCC offers a more precise definition, describing a heatwave as an extended period of unusually hot weather relative to a reference temperature threshold, with durations ranging from two days to several months (IPCC, 2023).

Based on these definitions, various indices and metrics have been developed to categorize heatwaves in terms of their frequency, intensity, and duration. One of the early investigators, Frich et al. (2002), introduced 10 climate metrics to assess climatic extremes across different regions and sectors, five of which focused specifically on temperature extremes. Expanding on this work, the Joint CCl/CLIVAR/JCOMM Expert Team on Climate Change Detection and Indices (ETCCDI) developed additional indices to monitor warm and cold temperature extremes (Alexander et al., 2006). These indices remain widely used in IPCC assessments and broader climate studies.

While some ETCCDI indices capture extreme temperatures (e.g., TXx for monthly maximum daily maximum temperature and TXn for monthly minimum daily maximum temperature), others focus on broader temperature trends. However, absolute threshold-based metrics may not always account for regional differences in climate variability. To address this limitation, percentile-based indices provide a more adaptive framework for analyzing heatwaves. For example, TX90p quantifies the percentage of days when the daily maximum temperature exceeds the 90th percentile of the climatological distribution for that calendar day, based on a reference period. These percentile-based approaches are particularly useful in climate change studies, as they account for local climatological variations and enable more reliable trend assessments.

However, using percentile-based thresholds presents several challenges. The selection of percentile levels and reference periods involves a degree of subjectivity, making it difficult to determine appropriate thresholds, particularly in regions with limited data. Higher percentile thresholds require extensive datasets to maintain statistical robustness, whereas lower percentiles may include less severe warm spells that do not necessarily qualify as heatwaves. Additionally, small sample sizes can lead to unreliable threshold calculations,

potentially introducing artificial discontinuities in heatwave detection at the boundaries of the study period (Zhang et al., 2005).

Employing multi-dimensional heatwave metrics—those that integrate intensity, duration, and frequency—provides a more comprehensive and standardized framework for comparing heatwaves across different regions and time periods. This approach mitigates sampling biases and improves cross-regional comparability of heatwave characteristics. For example, Frich's Heat Wave Duration Index (HWDI) defines a heatwave as a period of more than five consecutive days with temperatures exceeding the local average by at least 5°C (Frich et al., 2002). However, this fixed threshold may be unsuitable for certain regions, such as the tropics, where temperature variability is lower, while the five-day duration criterion may be overly restrictive in capturing short but intense heatwaves.

To address these limitations, Russo et al. (2014) introduced the Heat Wave Magnitude Index (HWMI), which accounts for both the magnitude and duration of heatwaves, providing a more flexible and regionally adaptive metric. Russo et al. (2015) further refined this index into the Heatwave Magnitude Index Daily (HWMID), which eliminates the need to segment prolonged heatwave episodes into sub-events. Additionally, the HWMID could take on any value ≥ 0, unlike the original index's empirical cumulative distribution function (ECDF), which was constrained to the [0,1] interval. This refinement ensures a more continuous representation of heatwave intensity, making it suitable for comparative climate studies across different timescales and regions.

2.2.2 Heatwave definition used in this thesis

Our definition of heatwaves over Iraq represents a modified version of that introduced by Russo et al. (2015). Specifically, we remove both the long-term trend and the seasonal cycle from the daily maximum temperature before applying the percentile threshold. This modification was investigated to mitigate the influence of long-term warming and seasonality, making it easier to identify heatwaves as short-term relative extremes, as follows:

1. **Identification of the Target Area:** We first identify the daily maximum T2m at each grid point within the heatwave area over southern Iraq. This target area is defined to extend over 42°- 48°E and 29°- 34°N, which covers 546 grid points and approximately 341,635 km^2 (see the green box in Figure 3.3b) and covers the region with generally highest surface temperatures. This number of grid points provides a robust statistical basis to minimize the sensitivity to data resolution.

2. **Climatological Mean Seasonal Cycle:** To isolate the seasonal fluctuations from long-term trends, we apply a linear detrending procedure to the Daily Maximum Temperatures (Tmax) data for the period 1980-2022. The trend is removed by fitting

a linear regression model to the Tmax values and subtracting the fitted trend. The detrended Tmax data is then used to compute the mean seasonal cycle based on a 31-day running mean for each day of the year:

$$T_{\text{clim}}(d) = \frac{1}{31} \sum_{i=-15}^{15} T_{\max}(d+i) \tag{2.1}$$

where $T_{\text{clim}}(d)$ is the climatological mean for day d, and $T_{\max}(d+i)$ represents the daily maximum temperature within the 31-day window centered on day d.

3. **Tmax Anomalies:** Daily anomalies of the Tmax are computed by subtracting the climatological mean seasonal cycle:

$$T'_{\max}(d) = T_{\max}(d) - T_{\text{clim}}(d) \tag{2.2}$$

where $T'_{\max}(d)$ is the Tmax anomaly for day d, $T_{\max}(d)$ is the daily maximum temperature, and $T_{\text{clim}}(d)$ is the climatological mean.

4. **90th Percentile Threshold:** The 90th percentile (P_{90}) is computed over the full period (1980–2022) for each calendar day:

$$P_{90}(d) = \text{percentile}_{90}(T'_{\max}(d)) \tag{2.3}$$

where $P_{90}(d)$ is the threshold value of the 90th percentile for day d.

5. **Heatwave Event Criteria:** A heatwave is identified if at least 50% of the heatwave area shows Tmax anomalies exceeding the 90th climatological percentile for at least three consecutive days within the June-July-August (JJA) period.

We evaluated the sensitivity of heatwave occurrences to different percentile thresholds (90th, 92th, 95th, and 97.5th) under 60%, 50%, and 40% spatial coverage conditions (Fig. 2.1). While fewer events are detected at higher thresholds (Fig. 2.1a), the events tend to have similar intensity (Fig. 2.1b). Specifically, the standard deviation of the peak Tmax anomalies across the events remains relatively stable across the tested thresholds (ranging from 0.92K to 1.05K). Ultimately, our choice of thresholds represents a trade-off between the severity of events and the available sample size for our statistical analyses.

Figure 2.2 shows the temporal distribution and the length of all heatwave events based on our event definition. We find the events to be fairly evenly distributed across the years but with a tendency of more intense and longer-lasting events to occur more likely during either early or late summer and less frequent event occurrence during early/mid July (Fig. 2.3). Most events last 3-5 days, although two long-lived events lasting 11 days occurred in 1981 and 2001, respectively. Several events exceed an anomaly of 9 K and the year with

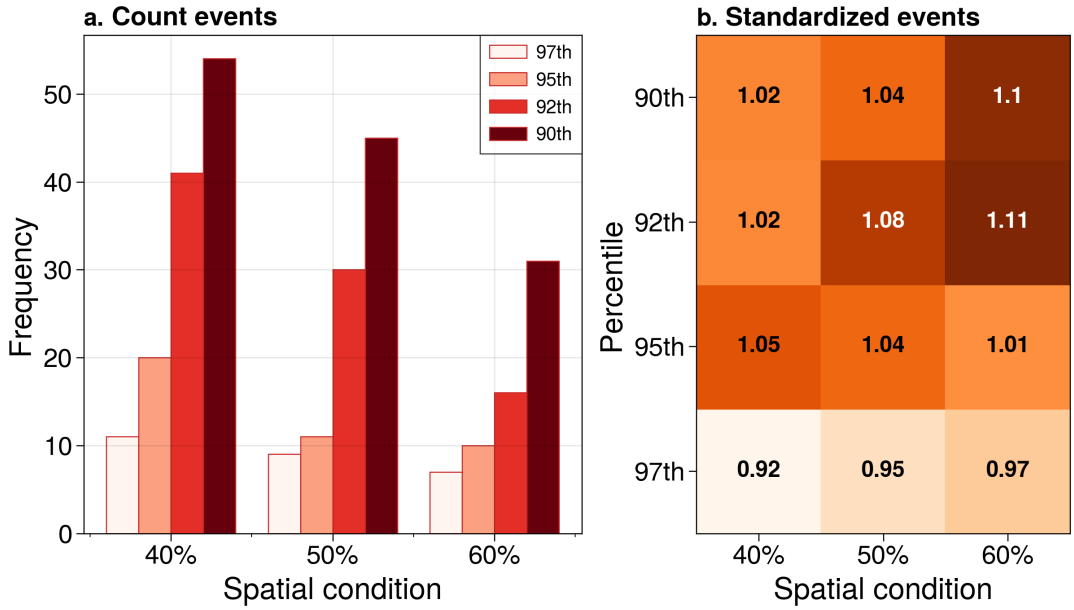

Figure 2.1: Impact of spatial condition and percentile thresholds on heatwaves events identification. a): The bar chart shows the frequency of detected heatwave events under different spatial conditions (40%, 50%, 60%) and percentile thresholds (90th, 92nd, 95th, and 97th). b): Standard deviation of the peak Tmax anomalies across the events of different spatial conditions and percentile thresholds, shading color is proportional to the value shown inside each box.

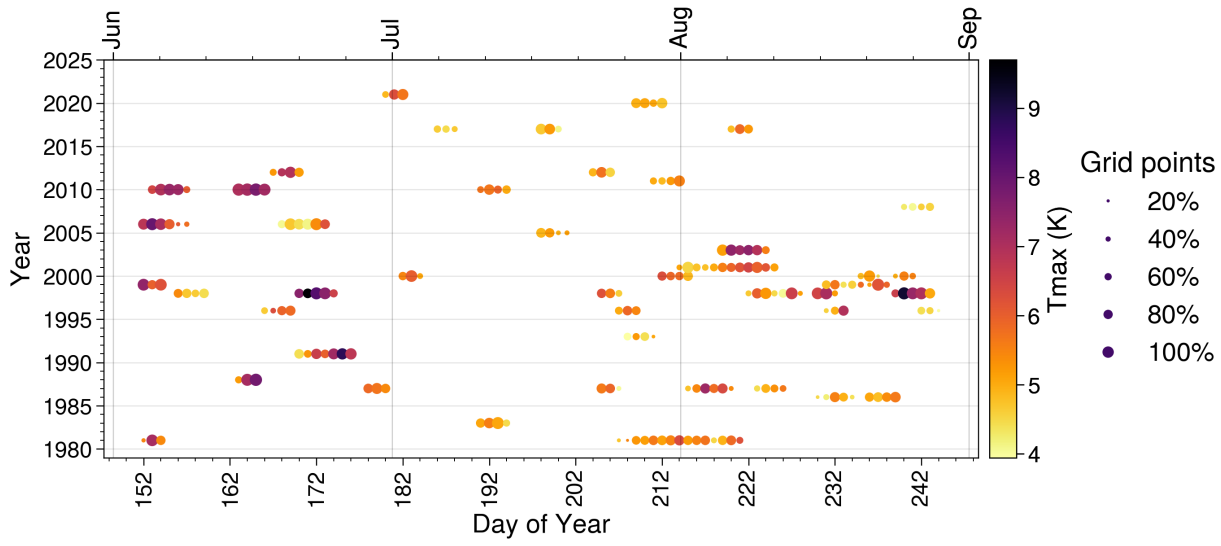

Figure 2.2: Occurrence of heatwave events for the months June through August within 1980 - 2022. The color shading indicates the Tmax anomalies (K) averaged over the target area (42°- 48°E and 29°- 34°N), the symbol size is proportional to the number of grid points that have values above the threshold.

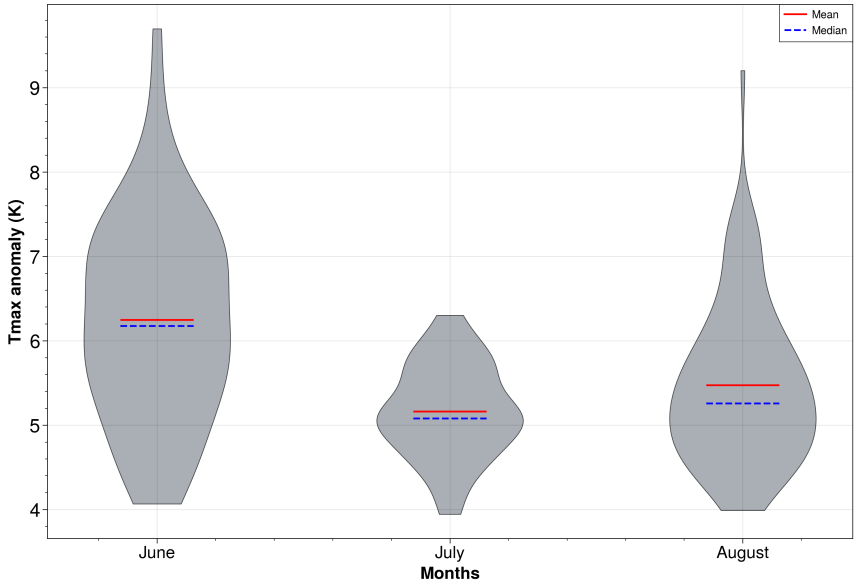

Figure 2.3: Distribution of ERA5-based Tmax anomalies during heatwave events, averaged over the target area. The violin plots represent the distribution of Tmax anomalies (K) for each summer month (June, July, and August) individually. The width of each violin reflects the density of events at different anomaly values. The red solid line denotes the mean Tmax anomaly, while the blue dashed line represents the median.

the highest number of events is 1998. Moreover, the strongest events coincide with the largest area coverage within our target region (Fig. 2.2).

2.3 Observational Data

We obtained observational daily Tmax data through direct communication with the **Iraqi Meteorological Organization and Seismology** of stations within our target area. However, significant portions of the data are missing across multiple years, which is a challenge for detrending and removing seasonal cycles. Even for years with available records, many daily observations are missing.

Despite these data gaps, we applied a detrending and removing seasonal cycle process similar to that used for the reanalysis data (see section 2.2.2). Heatwave events were then identified using the same criteria (90th percentile) and at least three consecutive days. However, because events were identified for each station individually, the spatial condition was excluded. The primary goal of using observational data was to assess how well ERA5 captures heatwave events compared to real measurements which could enhance the reliability of our heatwaves definition and their occurrence.

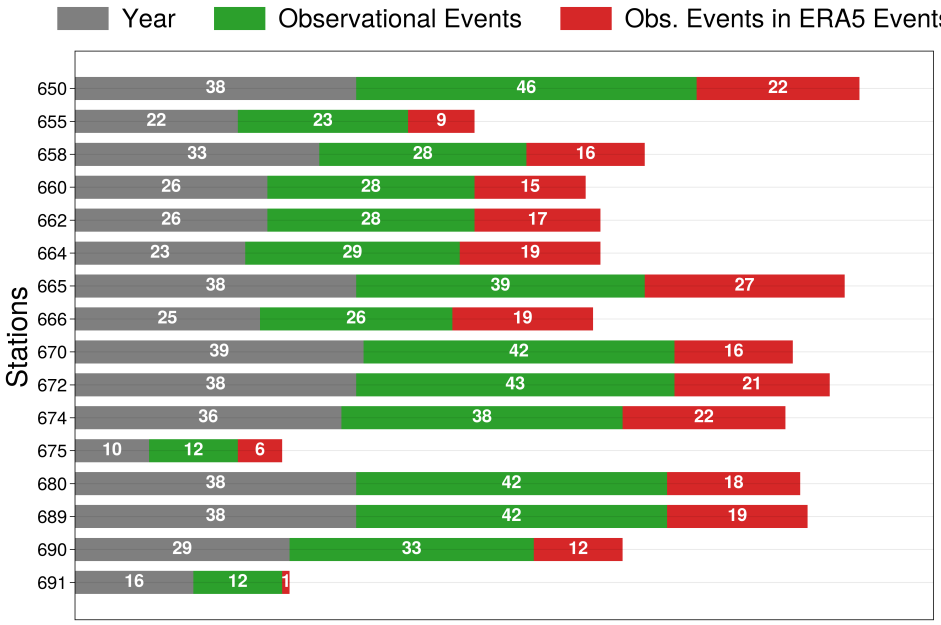

Figure 2.4: Statistical summary of observational data for each station. Gray indicates the number of available years of observational data corresponding to reanalysis data, green indicates heatwave events identified in the observational data, and red indicates observational events whose central day or ±1 day matches with ERA5 events.

Figure 2.4 illustrates the availability of yearly observational data (gray bars), revealing that some stations, such as Baghdad station (650), have relatively good samples of datasets. The green bars represent heatwave events identified in the observational data, while the red bars indicate events that match with ERA5 events in terms of central day or ±1 day margin. The high frequency of matching events (red bars) suggests that many reanalysis events are reliable. For example, AL-HAi station (665), which is more influenced by topography as it is located on the leeward side of the Zagros Mountains, shows observational events more than half of ERA5 events. However, comparing heatwave intensity between these datasets is more challenging due to missing data, which can impact the representation of climatological trends.

Figure 2.5 further supports a qualitative analysis of the temporal and spatial distribution of events across stations. Rather than focusing on intensity differences between ERA5 and observational events, a more effective approach is to analyze event characteristics based on station locations, duration, and frequency. For instance, the heatwave event that occurred on June 1–6, 2006, appears intense and long-lasting in stations that are in the northern and northeastern parts of our study area (Fig. 2.5a,b). This pattern, regardless of the impact of missing data, suggests that additional factors, such as the Zagros Mountains, may contribute to extreme events in these regions. Interestingly, the long heatwave that occurred on August 1–13, 2021, not shown in stations (Fig. 2.5d, and other stations not

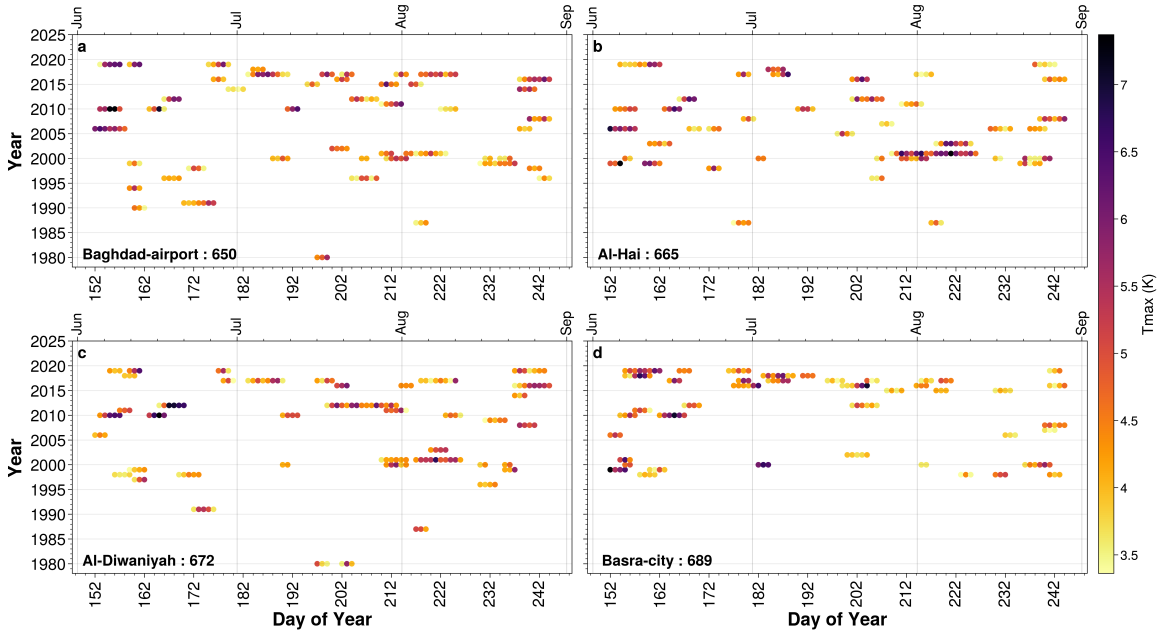

Figure 2.5: Occurrence of observational heatwave events for the months June through August within 1980 - 2020 of selected 4 stations, a) Baghdad-airport, b) Al-Hai, c) Al-Diwaniyah, and D) Basra city. The color shading indicates the Tmax anomalies (K), and the symbol size is constant.

shown) that are in the southern part of the study area while intensifying in the other stations (Fig. 2.5a,b,c).

Figure 2.6 shows a comparative analysis of reanalysis heatwave events using both observational and reanalysis (ERA5) data. Overall, the reanalysis data generally seem to be similar or slightly warmer temperature intensities compared to observations at most stations, particularly those located in central and southwestern Iraq, with the notable exception of station 670 (Al-Najaf), which is typically situated in the desert region. In contrast, for stations situated on the lee side of the Zagros Mountains, in elevated regions, or in the southern areas of Iraq, the observational data tend to show significantly higher temperatures than those recorded in ERA5, highlighting a potential underestimation by the reanalysis dataset in these areas.

This emphasizes the potential influence of local factors in modifying event characteristics. Ultimately, combining a spatial condition with the other criteria used in heatwave identification is crucial to mitigate local influences such as urban structures, cities, industrial Zones, and small-scale topographic features. In the following chapters, two case selections that examine the underlying physical processes will be based on both observational and ERA5-derived heatwave events, providing a structured framework for validating our analysis and hypotheses.

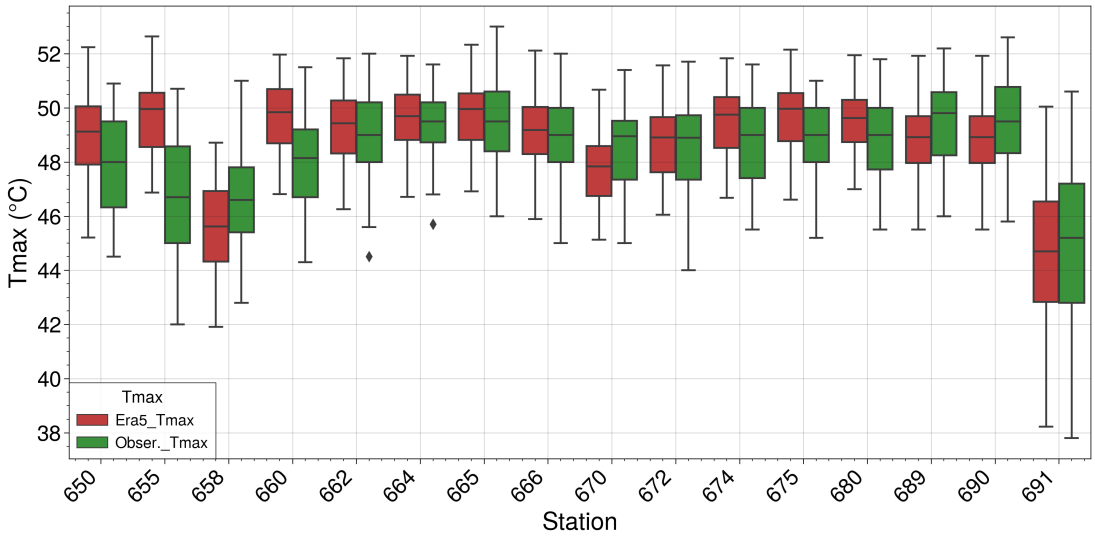

Figure 2.6: Comparison of heatwave events obtained from reanalysis data (ERA5, red boxes) with observational data (green boxes) for each station. For ERA5, the nearest grid point to each station was used. The boxplots include only the events that were matched between the two datasets.

Chapter 3

Dynamical aspects and mechanisms

This chapter investigates ERA5 reanalysis data to identify the main dynamical features associated with heatwaves. First, a single representative event is examined to illustrate the key physical drivers of heatwave evolution. Then, a composite-mean analysis is conducted using a wide range of variables at different pressure levels to further explore these drivers. This approach is also used to classify the events based on their dynamical characteristics. The findings provide further evidence of the influence of large-scale upper-level circulation patterns on local dynamics, which play a crucial role in the evolution of heatwave events.

3.1 Background

Temperature extremes are often driven by anomalous features of the mid-latitude large-scale circulation, suggesting that Rossby wave trains may contribute to the formation of heatwaves (Simpson et al., 2015; Rodwell and Hoskins, 1996; Hurrell, 1995, also see Chapter 1). On the regional scale, circulation over the Middle East interacts strongly with the complex topography. Tyrlis et al. (2013) highlighted the role of diabatic surface heating in elevated terrains, such as the Zagros Mountains, in modifying the low-level circulation. They also showed that topographic funneling in the Iraq–Gulf region contributes to the formation of the thermal low over the Gulf, due to the blocking influence of the mountain range extending from Turkey to Iran. Furthermore, they identified a potential influence of the South Asian Monsoon on Middle Eastern circulation, mediated by equatorially trapped Rossby waves generated by deep convective heating in the monsoon region that propagate westward (Rodwell and Hoskins, 1996). This mechanism creates subsidence and northerly flow (Etesian winds) over the eastern Mediterranean (Tyrlis et al., 2013). Similarly, Mofidi and Zarrin (2022) demonstrated that orographic effects strengthen the LLJ (Shamal winds) over Iraq (Fig. 1.2a,b).

The results of this section are published in AL-Shamarti, H., P. Rupp, and T. Birner. 2025. "Circulation Aspects Associated With Heatwave Events Over Iraq." International Journal of Climatology e70017. https://doi.org/10.1002/joc.70017.

Given the long-term exposure of the Middle East to extreme summer temperatures, heatwaves have attracted increasing scientific attention. However, most studies emphasize statistical descriptions of heatwave characteristics (see AL-Tamimi et al., 2020; Salman et al., 2017; Tanarhte et al., 2015; Nasrallah et al., 2004), with less focus on the underlying circulation mechanisms. In this chapter, we therefore examine both the large-scale and regional circulation patterns associated with heatwave evolution over Iraq.

3.2 Case Studies and Composite Evolution of Heatwave Events

3.2.1 Examining a single event

We start by examining a single heatwave event to illustrate some of the underlying physical drivers, which will be studied in more detail for all events in the following sections. The event selected, with its central day on June 22, 1998, was chosen based on its significant duration and intensity.

Figure 3.1a shows that the Tmax anomalies averaged over the target area steadily increased during the week preceding the event with a more rapid decline during the 3 days following the event. In particular, the maximum temperature in the reanalysis data over our target area reached 50.9°C on the central day, which is quite close to the values observed in station data. For example, the Basra Airport station, located approximately 88 km from this grid point, recorded 50.8°C *. Interestingly, the Tmax anomalies were already elevated by approximately +2 K as early as 10 days before the event, suggesting an anomalously warm June potentially linked to broader climate fluctuations such as the strong 1997/98 El Niño event that caused record global surface temperature (NOAA, 1998).

As discussed in the introduction (Section 3.1), the low-level jet (Shamal wind) plays an important role in temperature fluctuations in this region. Therefore, to examine the association between Tmax anomalies and Shamal wind anomalies, we consider a cross-section from 41°E/34°N to 48°E/30°N, which cuts through the heatwave-affected area and aligns with the Zagros Mountains. Along this cross-section, we analyze the evolution of anomalous wind speed as a function of height (Fig. 3.1b). We find a significant weakening of the Shamal wind in the days leading up to the heatwave event (Fig. 3.1b). This weakening reduced the typical cooling effect of the Shamal wind, allowing surface temperatures to rise.

Figure 3.1c shows low-level high-pressure anomalies over the Zagros mountains and Iran

*When comparing it with the nearest reanalysis grid point (about 53 km away), the maximum temperature was 50.6°C.

The results of this section are published in AL-Shamarti, H., P. Rupp, and T. Birner. 2025. "Circulation Aspects Associated With Heatwave Events Over Iraq." International Journal of Climatology e70017. https://doi.org/10.1002/joc.70017.

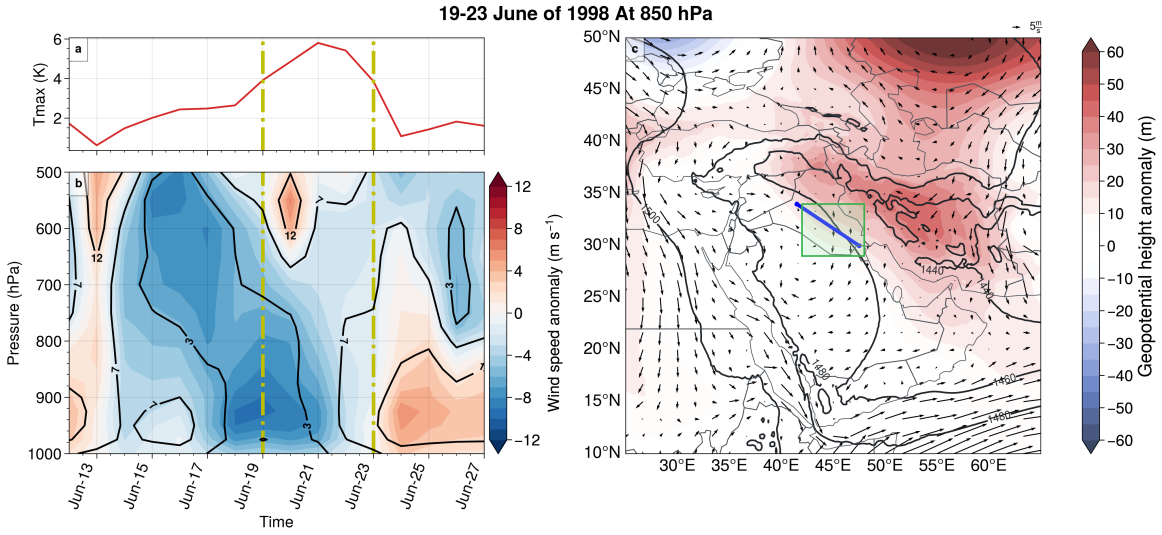

Figure 3.1: Different fields describing the heatwave case study with the central day on 22 June 1998. a) Evolution of Tmax anomalies (units: K) averaged over our target region. b) Cross-section of anomalous horizontal wind speed (full field as black contours) averaged along the line from 41°E/34°N to 48°E/30°N (blue line in Fig. 3.1c). c) Geopotential height anomalies averaged over 21-23 June 1998 with contour lines indicating its June climatology and horizontal total wind speed (arrows) at 850 hPa. Vertical dash-dotted lines in **a** and **b** indicate the period of the heatwave. The green box in **c** indicates the target area.

The results of this section are published in AL-Shamarti, H., P. Rupp, and T. Birner. 2025. "Circulation Aspects Associated With Heatwave Events Over Iraq." International Journal of Climatology e70017. https://doi.org/10.1002/joc.70017.

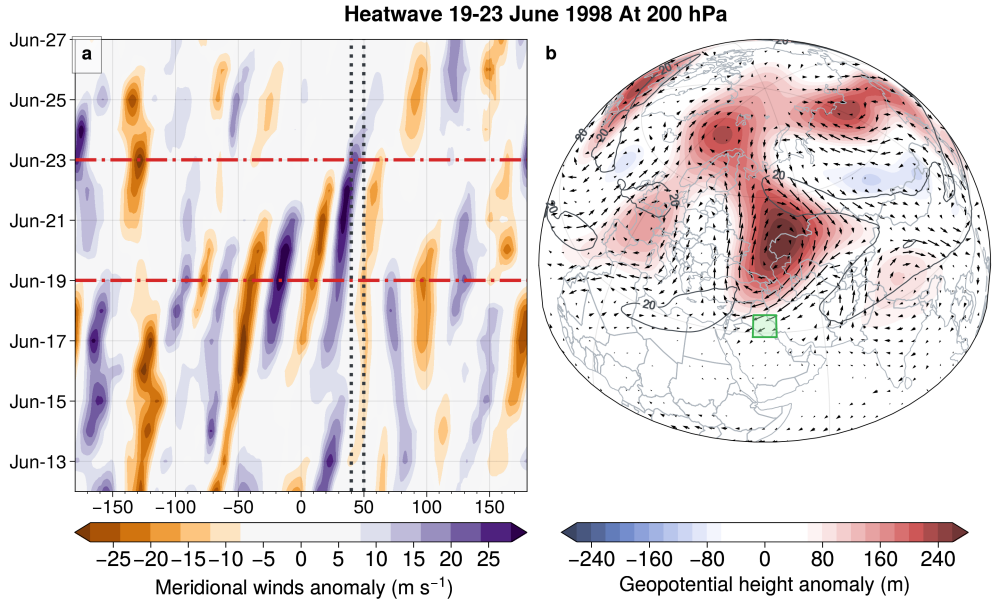

Figure 3.2: Upper-level (200 hPa) Rossby wave signatures during the heatwave case study with the central day on 22 June 1998. a) Hovmöller plot of meridional wind anomaly averaged over 37°-55°N. Horizontal dash-dotted lines indicate the period of the heatwave and vertical dotted lines indicate our target area. b) Geopotential height anomalies (shading), horizontal wind anomalies (arrows), and total zonal Wind (contours, units: m/sec) averaged over lag days -2 to +2 around the central day. The green box indicates our heatwave area.

that weaken the east-west pressure gradient in the region, consistent with reduced driving of the Shamal winds. Interestingly, this high-pressure anomaly appears to be linked to an even stronger high-pressure anomaly further north, which turns out to be the low-level signature of an upper-level anticyclonic anomaly (Fig. 3.2). This upper-level anomaly in turn appears to be embedded in a quasi-stationary Rossby wave train marked by alternating northerly and southerly flow anomalies across much of the subtropics and mid-latitudes, and which can be traced back almost 2 weeks prior to our heatwave event (Fig. 3.2a). Furthermore, the quasi-stationary pattern of this wave contributed to the intensification of its embedded anticyclonic anomalies, particularly to the north of Iraq (Fig. 3.2b).

As we will describe in Section 3.2.3, variations in the African-Asian jet influence the upper-level wave pattern, acting as a waveguide for the Rossby wave (see arrows and contours in Fig. 3.2b). Increased waviness of the jet is associated with slowed wave propagation, prolonging the exposure of the surface to anticyclonic conditions such as adiabatic warming by subsidence, increased solar irradiation, and reduced cloud cover. This setup creates favorable conditions for elevated surface temperatures, potentially leading to the occurrence of a heatwave.

The results of this section are published in AL-Shamarti, H., P. Rupp, and T. Birner. 2025. "Circulation Aspects Associated With Heatwave Events Over Iraq." International Journal of Climatology e70017. https://doi.org/10.1002/joc.70017.

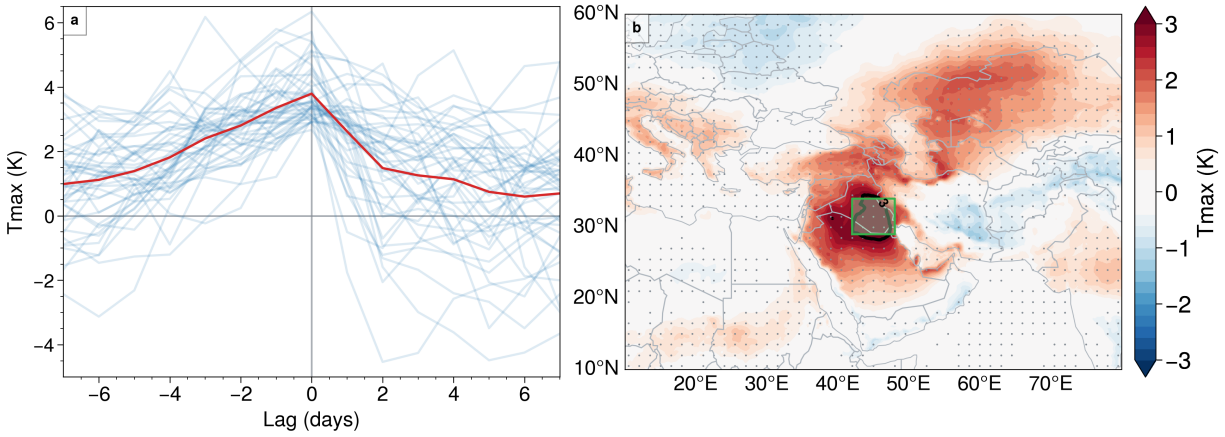

Figure 3.3: a) Composite-mean evolution of Tmax anomalies averaged over the heatwave area (red line). The thin blue lines show the individual evolutions for all 45 events. b) Composite-mean of Tmax anomalies averaged over lags -2 to +2 days. The black contour line indicates Tmax anomalies exceeding 3 K. The green box indicates our heatwave area. The dots indicate anomalies that are statistically significant with 95% confidence.

3.2.2 Composite mean evolution of heatwave events

The case study in the previous section suggests that reduced Shamal winds associated with upper-level anticyclonic anomalies toward the north are important for heatwave occurrence over our target area. In this subsection, we use composite-mean analyses to explore to what extent these circulation anomalies are important for our heatwave events in general. Figure 3.3a shows the composite-mean evolution of Tmax anomalies averaged over southern Iraq. It demonstrates that our heatwaves typically strengthen gradually over the week preceding the central day, with the peak Tmax anomaly reaching 3.7 K. However, this is followed by a more rapid decline in the days after the event, suggesting an asymmetry in the processes driving the growth and decay of the heatwaves.

During the evolution of the heatwaves, a wide area extending from the Arabian peninsula northward across Iraq toward southwestern Russia shows anomalously high Tmax values (Fig. 3.3b). As expected, the highest anomalies appear over the heatwave area around the central day.

The large extent of the temperature signature of our events suggests an involvement of large-scale dynamical processes. Figures 3.4a-c show the composite-mean upper level (200 hPa) geopotential height and wind anomalies over much of the Northern Hemisphere before, at, and after the central day averaged over all heatwave events. A pronounced anticyclonic high can be identified to the northeast of the target area, which tends to be strongest during the peak of the events. This anticyclone is associated with a sustained upper-level northeasterly flow toward Iraq. Furthermore, the upper-level high appears to be embedded

The results of this section are published in AL-Shamarti, H., P. Rupp, and T. Birner. 2025. "Circulation Aspects Associated With Heatwave Events Over Iraq." International Journal of Climatology e70017. https://doi.org/10.1002/joc.70017.

in a large-scale Rossby wave train that extends from the Atlantic toward the Bay of Bengal as well as even further eastward.

Figures 3.4d-f further highlight the Rossby wave train in terms of alternating southward and northward wind anomalies at 200 hPa that are most prominent at and just before the central day from central Europe beyond the Caspian Sea. The strongest Rossby wave amplitudes are found between the Atlantic and Asian jet cores (see black solid contours in Fig. 3.4d-f), which act as waveguides (Wirth et al., 2018). Strong southward flow anomalies are found directly to the northeast of our target area, consistent with the anomalous anticyclonic circulation in Fig. 3.4a-c. We again find that wave amplitudes disappear quite abruptly following the central day (Fig. 3.4f). An interesting characteristic of the wave train in Figures 3.4d and e is its very slow progression; the wave train appears to be quasi-stationary around Iraq during the onset and peak of the composite evolution. Southward wind anomalies are present with persistently strong amplitude for $\simeq$10 days around the heatwave area (40°- 50°E) (Figure A.1). Similarly, persistent and quasi-stationary northward wind anomalies are present further east (between 70°- 85°E). These quasi-stationary features abruptly disappear at positive lags ($\pm$2 days following the event).

One mechanism by which an anticyclonic high may produce surface warming is via adiabatic warming due to large-scale subsidence, further facilitated by the suppression of clouds and associated enhanced radiative heating. Anomalous large-scale sinking is indeed found during our heatwave events, strongest underneath the eastern flank of the upper-level anticyclone (Fig. 3.5) over Iran near the Zagros mountains. Further, anomalous large-scale ascent is found over the eastern Mediterranean, on the western flank of the upper-level anticyclonic high, embedded in the Rossby wave train. We further found anomalies in total cloud cover, potentially connected to the anomalies in vertical velocity (see Section 3.2.3 for further discussion of cloud cover and surface radiation anomalies).

Figures 3.4 and 3.5 showed that heatwaves over southern Iraq are, in the composite mean, associated with an upper-level anticyclonic high located to the northeast of Iraq. In the following, we investigate in more detail how the surface warming induced by this anticyclone extends to our heatwave area. Figure 3.6a shows strong low-level northeasterly flow anomalies that stretch from the area underneath the upper-level high across the Zagros mountains, reaching southern Iraq. These low-level flow anomalies indicate horizontal advection of warm air toward our target area, as well as warming due to down-slope flow on the leeward side of the Zagros Mountains (see Section 3.3).

The near-surface flow, on the other hand, shows distinctly different features. Predominantly, the surface flow anomalies (Fig. 3.6b) are characterized by south-easterly wind anomalies, which contrast with the prevailing north-westerly (Shamal) winds observed in this region during the early summer. This indicates suppression of cold-air advection from the north and therefore effectively enhances the warming.

The results of this section are published in AL-Shamarti, H., P. Rupp, and T. Birner. 2025. "Circulation Aspects Associated With Heatwave Events Over Iraq." International Journal of Climatology e70017. https://doi.org/10.1002/joc.70017.

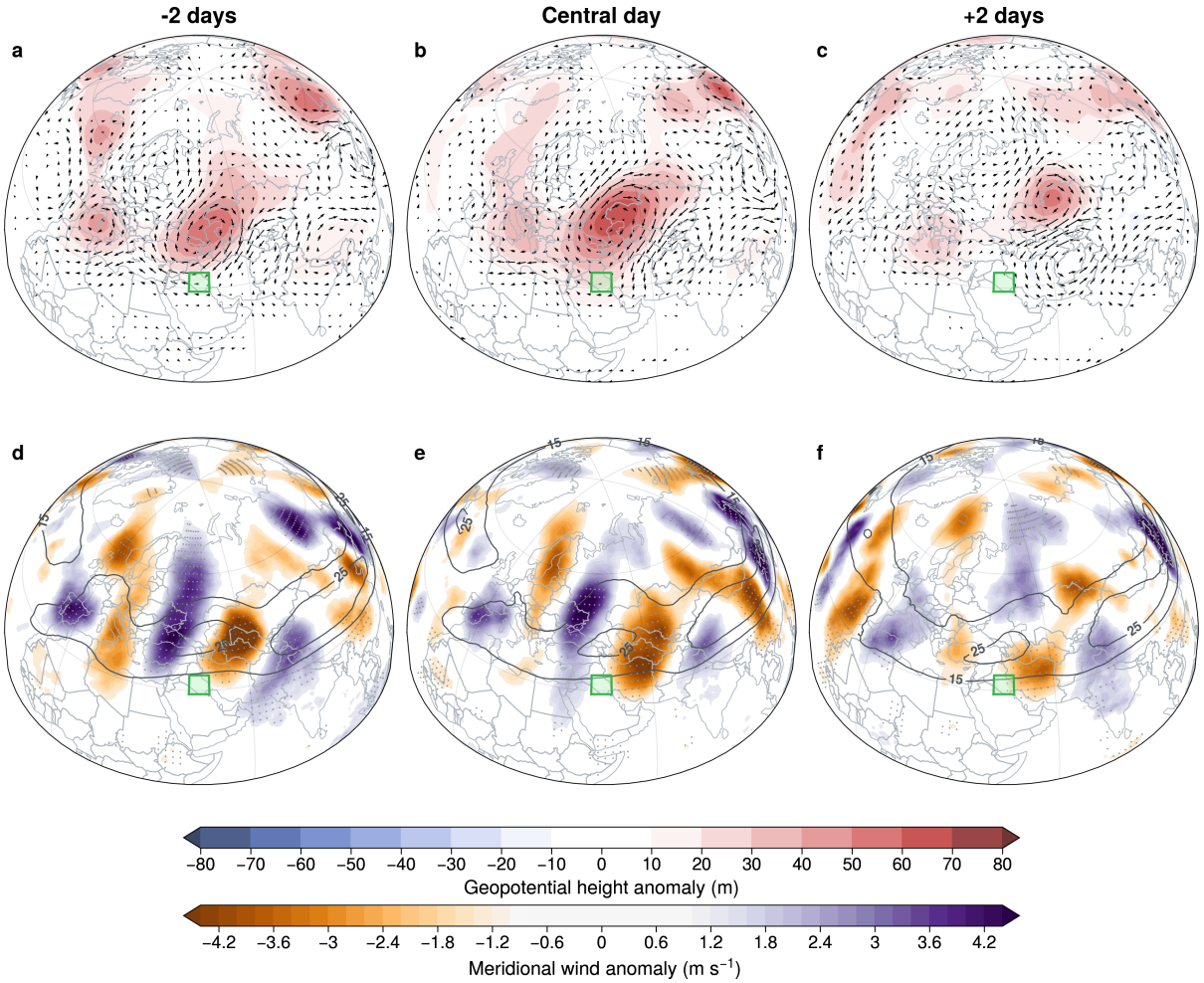

Figure 3.4: **a** to **c**: Composite-mean evolution over all events of geopotential height anomalies (shading) and horizontal wind anomalies (arrows). **d** to **f**: same for meridional Wind anomalies (shading) and total Zonal Wind (contours, units: m/sec). All fields are shown at 200 hPa and 2 days preceding the event (a,d), at the central day (b,e), and 2 days following the event (c,f). The green boxes mark the heatwave area. For **a** to **c**: only values that are statistically significant at the 95% confidence level are shown, for **d** to **f**: the dots indicate the statistical significance at the same level.

The results of this section are published in AL-Shamarti, H., P. Rupp, and T. Birner. 2025. "Circulation Aspects Associated With Heatwave Events Over Iraq." International Journal of Climatology e70017. https://doi.org/10.1002/joc.70017.

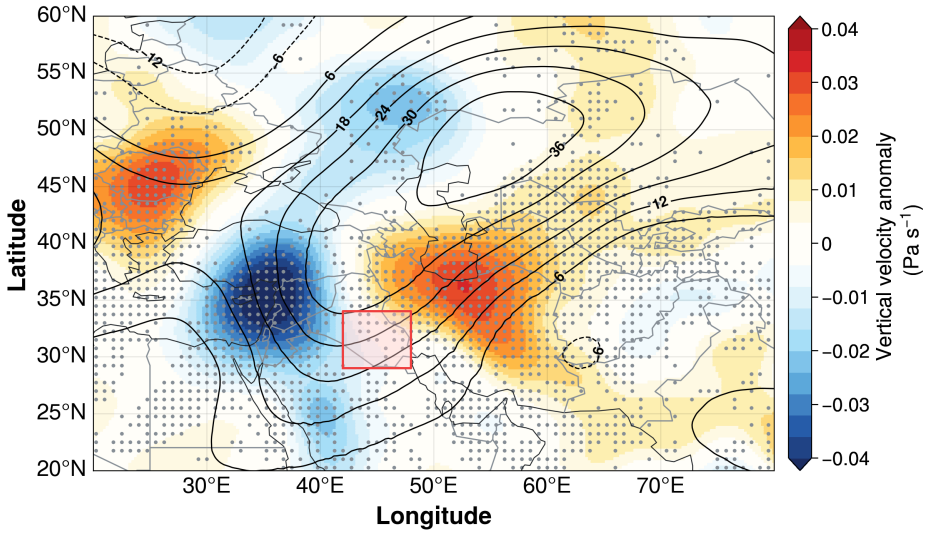

Figure 3.5: Composite-mean of vertical velocity anomalies (shading) and the geopotential height anomalies (contours, units: m) at 500 hPa averaged over lags -2 to +2 days. The red box marks the heatwave area. The dots indicate the values that are statistically significant at the 95% confidence level.

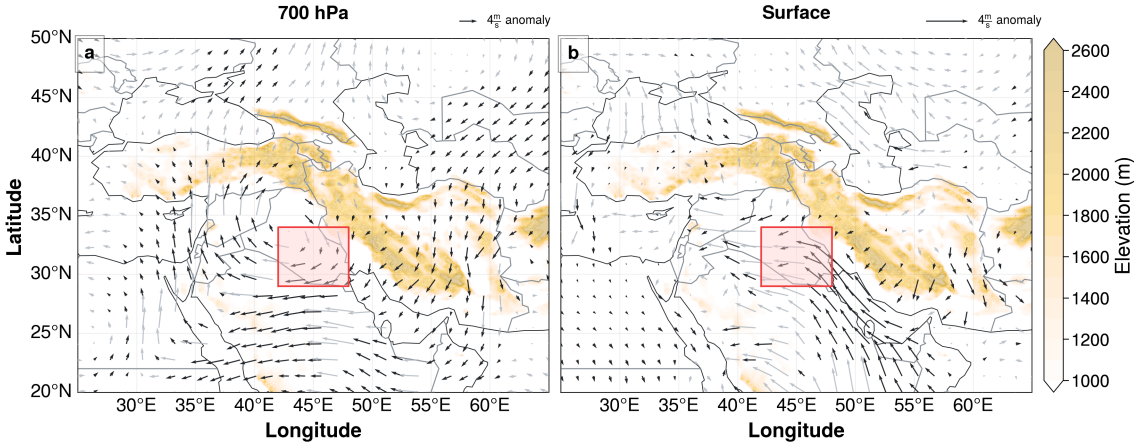

Figure 3.6: Composite-mean of horizontal wind anomalies vectors averaged over lags -2 to +2 days, (a) at 700 hPa level and (b) at surface level. Shading indicates the elevation of topography. The red box marks the heatwave area. The bold vector indicates the anomaly wind field, with black arrows exceeding the 95% confidence level.

The results of this section are published in AL-Shamarti, H., P. Rupp, and T. Birner. 2025. "Circulation Aspects Associated With Heatwave Events Over Iraq." International Journal of Climatology e70017. https://doi.org/10.1002/joc.70017.

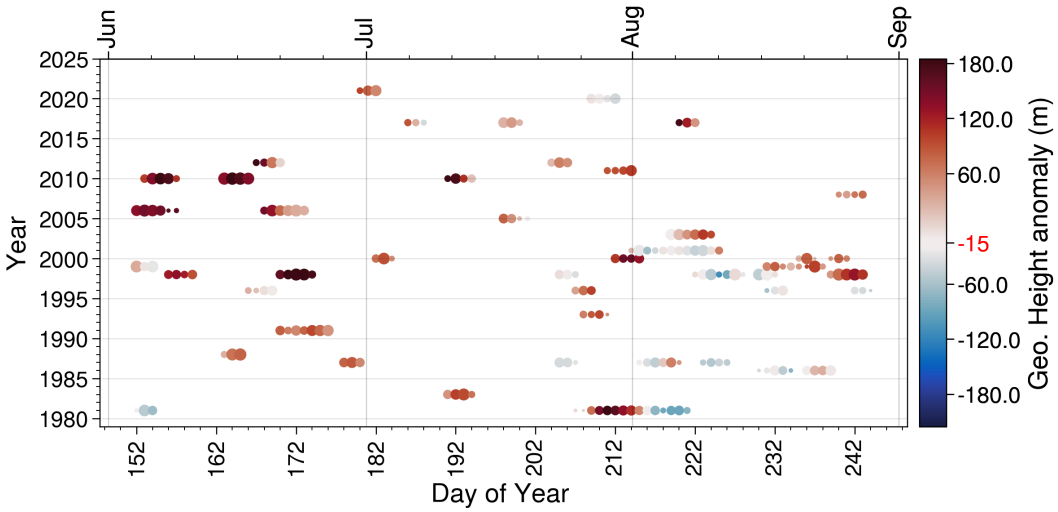

Figure 3.7: Similar to figure 2.2, but with color shading indicating the GHI. The GHI is defined as geopotential height anomaly at 200 hPa averaged over the region 40-60°E, 37-55.5°N (gray box in Fig. 3.9).

3.2.3 Physical drivers of heatwaves over Iraq

The presence of a Quasi-Stationary Anticyclonic High (QSAH) to the northeast of our target area seems crucial for our diagnosed heatwave events (e.g., Figure 3.4). However, given the statistical nature of the composite-mean analysis, one may ask the question: are all events associated with such an anticyclonic feature? And if not, what other physical and dynamical processes drive the identified heatwave events? To answer these questions, we classify events depending on whether they show an anticyclonic high (i.e., positive geopotential height anomaly) northeast of the heatwave area. Specifically, we create a classification index (thereafter Geopotential Height Anomalies Index (GHI)) based on the geopotential height anomaly averaged over the region that develops the QSAH in the composite mean (40-60°E, 37-55.5°N).

Figure 3.7 shows that while many events do exhibit strongly positive GHI, other events show either small positive GHI or even negative GHI (i.e., cyclonic anomalies). Closer inspection of the frequency distribution of GHI (Fig. 3.8) reveals that a threshold of GHI = 15 m effectively divides the heatwave events into two clusters, with 29 events exhibiting GHI $>$ 15 m (i.e., strong QSAH embedded in a Rossby wave, hereafter referred to as Rossby wave (RW) events) and 16 events exhibiting GHI $<$ 15 m (Non-RW events).

Figure 3.9 shows composite mean anomalies of Tmax and 200 hPa geopotential height separately for the RW and Non-RW clusters. The RW cluster (Fig. 3.9a) shows overall similar anomalies as the total composite shown in Fig. 3.3b in terms of spatial distribution and intensity. The Non-RW cluster (Fig. 3.9b), on the other hand, only shows regional warm

The results of this section are published in AL-Shamarti, H., P. Rupp, and T. Birner. 2025. "Circulation Aspects Associated With Heatwave Events Over Iraq." International Journal of Climatology e70017. https://doi.org/10.1002/joc.70017.

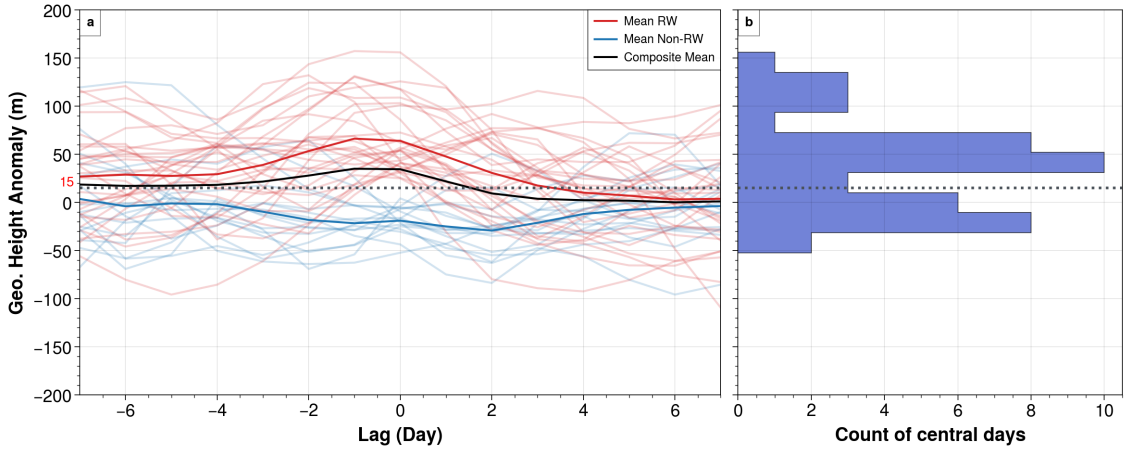

Figure 3.8: a) Composite-mean evolution of geopotential height anomalies averaged over the GHI area (black line). The thin red/blue lines show the individual evolutions for all 45 events. The bold red/blue lines show the mean of RW/Non-RW events. b) Number of the central day of events based on GHI.

anomalies over our target area, but cold anomalies to the northeast that are associated with upper-level low-pressure anomalies (somewhat by construction, since we demand GHI < 15 m for this cluster). These differences suggest that different mechanisms are acting for the RW versus the Non-RW clusters. To shed more light on these differences we next analyze the dynamical evolution of both clusters in more detail.

Figure (3.10) shows upper-level (200 hPa) meridional wind and geopotential height anomalies on the central day for the RW and Non-RW clusters. These anomalies indicate a clear RW pattern for the RW cluster (as expected), which appears even more pronounced as in the total composite (Fig. 3.4). A Fourier analysis based on the meridional wind anomaly averaged between 37.5-57.5°N reveals that the waves' dominant zonal wavenumber is between 6 and 7 (Fig. 3.11). In contrast, the Non-RW cluster does not show signs of Rossby waves surrounding the heatwave area, again suggesting that different mechanisms are at play for these heatwaves.

The dominance of different driving mechanisms is also evident from anomalies in thermodynamic variables. For example, the RW cluster shows a pronounced reduction in cloud cover over the QSAH region (Fig. 3.12a) that is consistent with anomalous sinking there (Fig. 3.13). This reduction in cloud cover is also associated with enhanced solar net radiation at the surface and total column water reduction (Fig. 3.14), which overall enhances the diabatic heating over this region.

The Non-RW cluster shows less coherent cloud cover anomalies (Fig. 3.12b), although a pronounced positive anomaly appears over northern Saudi Arabia, extending into western Iraq. We further find generally enhanced cloud cover surrounding the Arabian Peninsula,

The results of this section are published in AL-Shamarti, H., P. Rupp, and T. Birner. 2025. "Circulation Aspects Associated With Heatwave Events Over Iraq." International Journal of Climatology e70017. https://doi.org/10.1002/joc.70017.

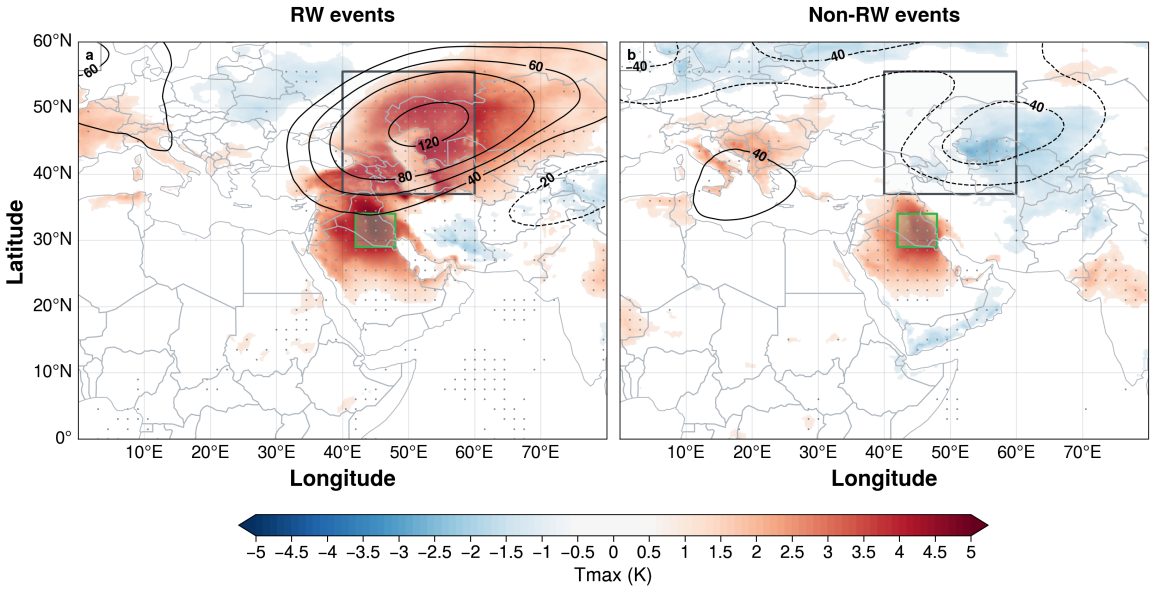

Figure 3.9: Composite-mean of Tmax anomalies (shading) and geopotential height anomalies (contours, units: m) at 200 hPa on the central day of (a) 29 RW events and (b) 16 Non-RW events. The green and gray boxes mark the heatwave area and the area used to define GHI, respectively. The dots indicate anomalies that are statistically significant with 95% confidence.

extending from the monsoon region (western India) to Ethiopia and Sudan, reaching the Red Sea. This configuration could be associated with the migration of the Inter-Tropical Convergence Zone (ITCZ) during the summertime (see section 3.3).

To study the impact of weakened low-level Shamal winds on the heatwave events (cf. Fig. 3.6, Section 3.2.2), we analyze the composite mean evolution of the anomalous wind speed (Fig. 3.15 produced like Fig. 3.1b). The climatological profile for this metric (Fig. 3.15a) shows a distinct (LLJ) that corresponds to the Shamal wind (north-westerly) near the surface up to about 800 hPa.

Figures 3.15b and c show the composite mean anomalies around RW and Non-RW anomalies. Both clusters exhibit a significant weakening of the LLJ by several m/s prior to the event, suggesting that the associated reduced cold air advection contributes to the development of the heatwaves. Notably, this wind speed reduction is strong enough so that near the central day of the events, the wind speed profile is more or less vertically uniform, i.e., without distinct LLJ. For the RW events, the wind speed reduction extends throughout the troposphere, whereas it is confined to lower levels for the Non-RW events. This suggests a connection between the upper-level large-scale circulation configuration (e.g., associated with the QSAH to the north-east of our target area, see Fig. 3.10a) and the reduction of the Shamal winds for the RW events. For the Non-RW events, on the other hand, the

The results of this section are published in AL-Shamarti, H., P. Rupp, and T. Birner. 2025. "Circulation Aspects Associated With Heatwave Events Over Iraq." International Journal of Climatology e70017. https://doi.org/10.1002/joc.70017.

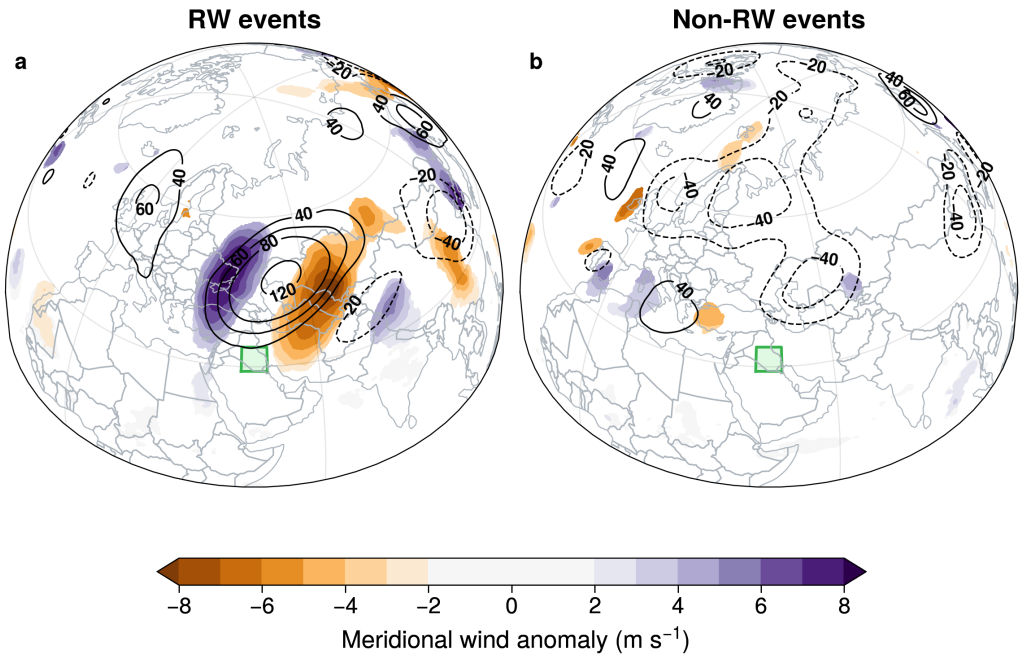

Figure 3.10: Composite-mean of meridional wind anomaly (shading) and geopotential height anomaly (contours, units: m) at 200 hPa on the central day of (a) 29 RW events and (b) 16 Non-RW events. The green box marks the heatwave area. Only values that are statistically significant at the 95% confidence level are shown.

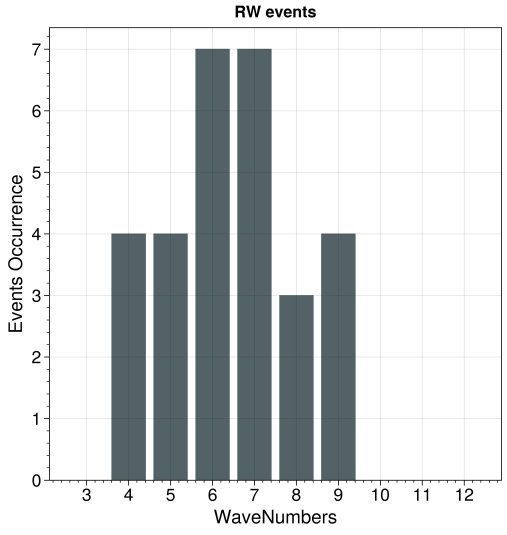

Figure 3.11: Dominant wavenumber during RW heatwave events at 200hPa. The dominant wavenumber was computed based on the Fourier coefficient in the meridional wind anomaly at 200 hPa, averaged over 37.5-57.5°N, with the highest power.

The results of this section are published in AL-Shamarti, H., P. Rupp, and T. Birner. 2025. "Circulation Aspects Associated With Heatwave Events Over Iraq." International Journal of Climatology e70017. https://doi.org/10.1002/joc.70017.

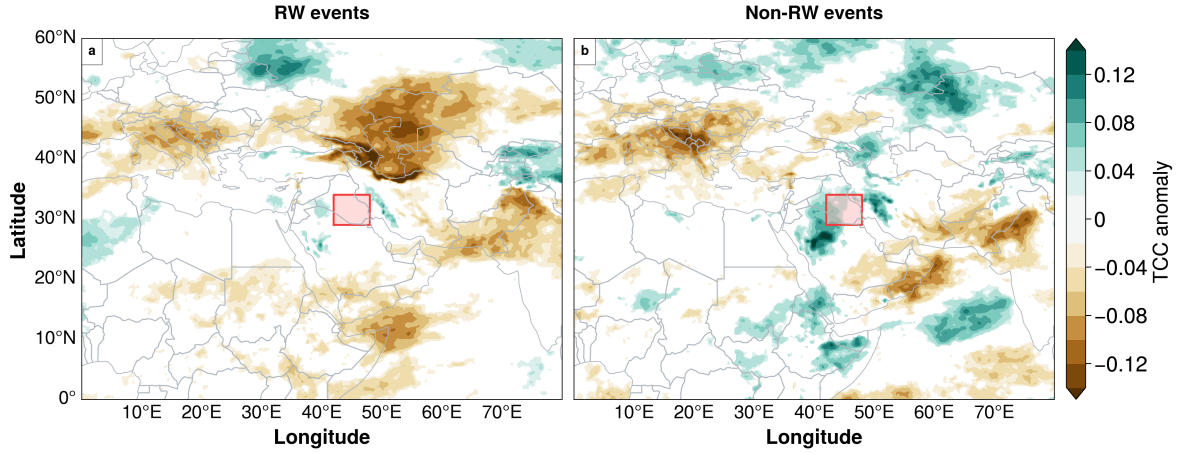

Figure 3.12: Composite-mean of Total Cloud Cover anomaly averaged over lags -4 to the central day of (a) 29 RW events and (b) 16 Non-RW events. The red box marks the heatwave area.

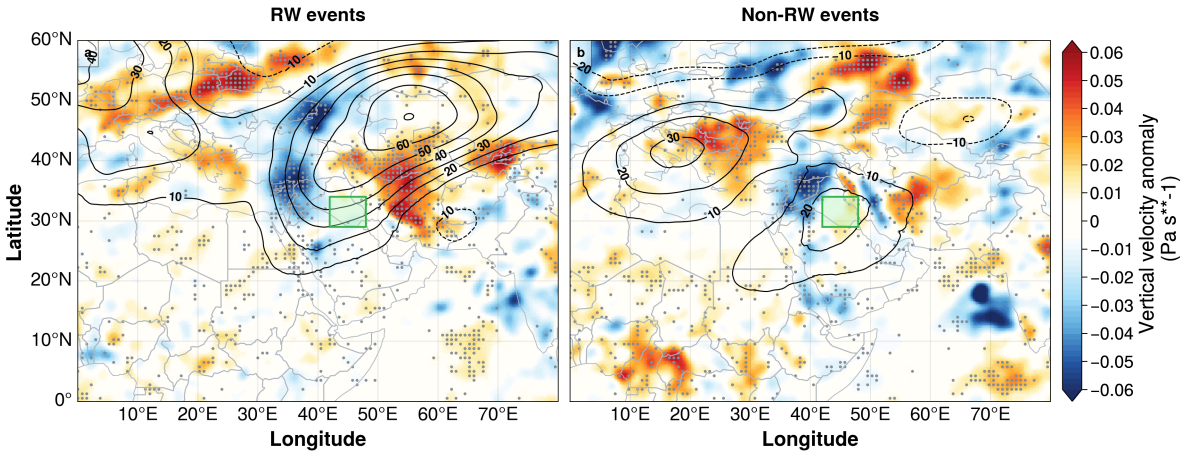

Figure 3.13: Composite-mean of vertical velocity anomalies (shading) and the geopotential height anomalies (contours, units: m) at 500 hPa averaged over central days, (a) RW events, and (b) Non-RW events. The red box marks the heatwave area. The dots indicate the values that are statistically significant at the 95% confidence level.

The results of this section are published in AL-Shamarti, H., P. Rupp, and T. Birner. 2025. "Circulation Aspects Associated With Heatwave Events Over Iraq." International Journal of Climatology e70017. https://doi.org/10.1002/joc.70017.

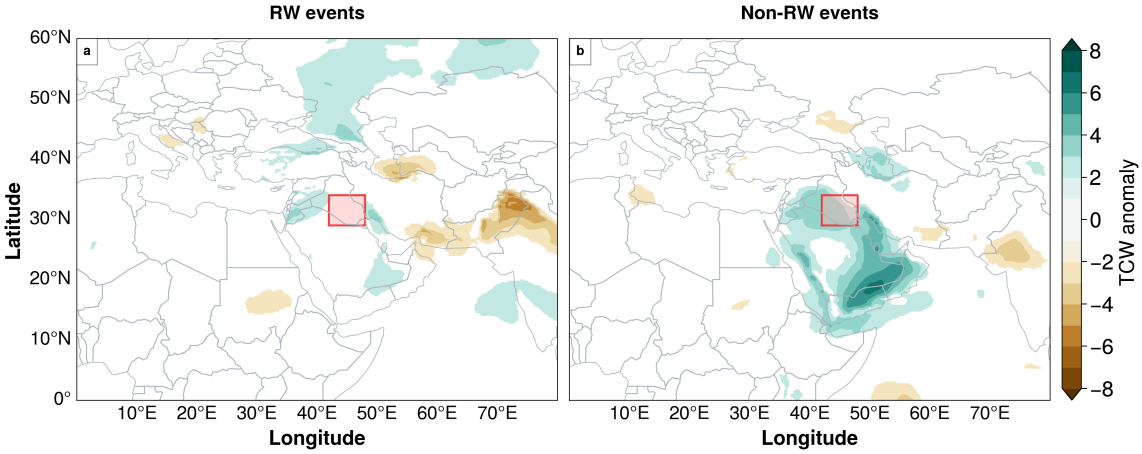

Figure 3.14: Composite-mean of Total Column Water anomaly averaged over lag days -4 to 0 of (a) 29 RW events and (b) 16 Non-RW events. The red box marks the heatwave area.

reduced LLJ seems to develop more regionally.

3.3 Discussion

Our analyses rely on ERA5, which captures well the large-scale circulation patterns driving these heatwave events. However, even with its 31 km horizontal resolution, ERA5 struggles to capture some of the complex interactions of mesoscale circulation features with the complex regional orography and land-sea contrasts (Belušić et al., 2018; Zhu and Atkinson, 2004). To mitigate some of these limitations, we employed a composite-mean approach focusing on regional averages, which helps to reduce some of the uncertainties by averaging over small-scale variations. Nevertheless, these limitations highlight the need for future research using higher-resolution datasets and regional climate models to better understand mesoscale dynamics, such as the Shamal wind.

Our results reveal that the majority of heatwave events (29 out of 45) over southern Iraq are associated with a large-scale anticyclonic system embedded in a quasi-stationary Rossby wave train (RW events). The remaining heatwaves (Non-RW events) do not show such an anticyclonic signature. However, we find a weakening of the Shamal winds during both heatwave clusters. For RW events, this Shamal wind weakening extends to upper levels, whereas it is more confined to near-surface levels for Non-RW events.

Regarding the weakening of the Shamal winds in both clusters, one may ask what synoptic-scale weather pattern can give rise to the Shamal wind in the first place?

The results of this section are published in AL-Shamarti, H., P. Rupp, and T. Birner. 2025. “Circulation Aspects Associated With Heatwave Events Over Iraq.” International Journal of Climatology e70017. https://doi.org/10.1002/joc.70017.

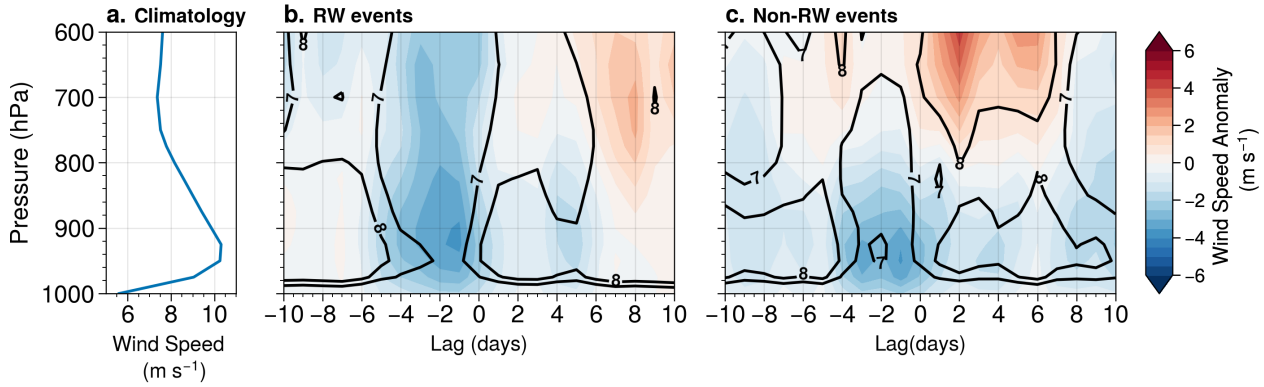

Figure 3.15: Cross-section of anomalous horizontal wind speed averaged along the line from 40°E/36°N to 48°E/30°N (see blue line in Fig. 3.1c). a) Climatology during June, July, and August (JJA), b and c) Composite-mean of the wind speed anomaly during RW and Non-RW events, respectively. Shading shows wind speed anomalies, and black contours show the total wind speed.

Figure 3.16 shows that days with strong Shamal wind † are associated with anomalous high-pressure over the eastern Mediterranean and anomalous low-pressure to the southeast of our heatwave area at 850 hPa. The corresponding friction-modified geostrophic flow strengthens the Shamal wind. This pressure pattern is associated with a reinforcement of the prevailing local thermal circulation, characterized by air rising over the low and sinking over the high (not shown). The complex orography of Iraq and its surrounding region further influences the Shamal wind. For example, the presence of the Zagros mountains in Eastern Iraq intensifies the Shamal wind through narrow channeling (Tyrlis et al., 2013). Based on the mechanism of the Shamal wind above, we can propose a potential mechanism that contributes to the occurrence of heatwaves, namely through the weakening of Shamal winds via interaction with quasi-stationary Rossby waves.

The manifestation of the Shamal wind depends on a significant pressure gradient. Therefore, to attenuate these winds, it is essential to weaken this pressure gradient. This pressure gradient can, for example, be influenced by the QSAH aloft, which was identified through composite analysis of the RW heatwave cluster. The QSAH system weakens the thermal low-pressure system located to the southeast of Iraq, reducing the pressure gradient and thereby attenuating the Shamal wind (cf. Fig. 3.1c).

Considering the intricate orographical structure, a pertinent question emerges: What other orographical influences may be important in driving the heatwaves? One relevant phenomenon that we identified is due to down-sloping winds (e.g., Figure 3.6). For the RW cluster, the combination between the eastern flank of the (QSAH) and the western flank

†Shamal wind defined as: Nighttime (9 pm-3 am local time; peak strength of the Shamal wind is at 3 am) horizontal wind speed along the line from 40°E/36°N to 48°E/30°N averaged over 1000-850 hPa.

The results of this section are published in AL-Shamarti, H., P. Rupp, and T. Birner. 2025. "Circulation Aspects Associated With Heatwave Events Over Iraq." International Journal of Climatology e70017. https://doi.org/10.1002/joc.70017.

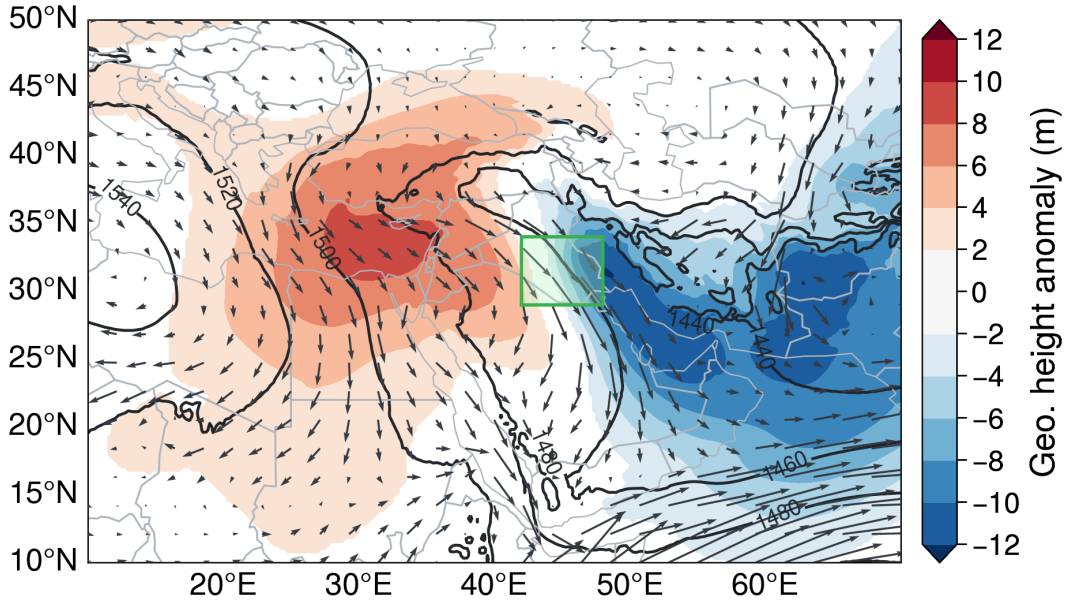

Figure 3.16: Composite-mean of geopotential height anomaly at 850 hPa (shading) over the days with nocturnal Shamal wind >10 m/s (see text for details) within the specified region encompassing the heatwave area (green box). Black contour lines indicate the geopotential height climatology (in m) for JJA. Arrows indicate the total horizontal wind field at 850 hPa. Only anomalies that are statistically significant at the 99% confidence level are shown.

The results of this section are published in AL-Shamarti, H., P. Rupp, and T. Birner. 2025. "Circulation Aspects Associated With Heatwave Events Over Iraq." International Journal of Climatology e70017. https://doi.org/10.1002/joc.70017.

of the Afghanistan-Tajikistan cyclone strengthens the northeasterly winds in the upper troposphere (over the Kyzylkum desert and Iran, including the Zagros mountains). This northeasterly flow, together with sinking over the Zagros mountains (Fig. 3.5), causes air masses to descend along their western and southern slopes into lower areas. The associated adiabatic warming may contribute to the formation of heatwaves. These down-slope winds seem to resemble Foehn winds.

A similar phenomenon refers to the so-called Sharqi winds ('Sharqi' is an Arabic term meaning easterly), which are easterly and southeasterly down-slope winds in the southern Zagros mountains (Ahvaz region, north of the Gulf). This configuration suggests the potential advection of warm-moist air into our target area by the Sharqi winds, which are enhanced by their convergence with the counterclockwise rotation of the thermal low-pressure system. The Sharqi winds likely have the potential to further modify the weakened Shamal winds. This requires that air masses possess sufficient kinetic energy to overcome the orographical structure. However, the diminishing thermal low weakens the acceleration of air masses, causing warm and humid air to become trapped in our heatwave region.

Both the weakening of the thermal low and the down-slope winds are likely indications of the influence of large-scale circulation patterns on heatwave events. Given the observation of Rossby waves in Figure 3.4, the question arises: What are the general circulation characteristics that give rise to these Rossby wave patterns?

The QSAH is embedded in a Rossby wave packet that initially propagates along the North Atlantic waveguide, changes of which are associated with the North Atlantic Oscillation (NAO). The NAO index strengthens this association by showing a prominent decline in the days leading up to the central day of heatwave events (Fig. 3.17). During NAO^- phases, the North Atlantic jet shifted southward, allowing the Rossby waves to propagate into the North African-Asian westerly jet. Effectively, the North African-Asian jet, despite being weak in the summertime, acts as a waveguide for the Rossby wave. Additionally, the weak jet favors the Rossby waves to become quasi-stationary.

Interestingly, despite the absence of Rossby waves during Non-RW events, a low-pressure system persists in the western part of our heatwave area. Whether the existence of this low-pressure system is robust is difficult to assess based on our limited number of events. Notably, a large number of Non-RW events occurred in late summer, coinciding with the typical poleward shift of the subtropical jet during that time. This shift makes it unlikely to observe a Rossby wave of mid-latitude origin over the Middle East, suggesting that either regional effects or perhaps circulation anomalies of tropical origin could play a role in these events.

For example, the poleward migration of the ITCZ during summer may contribute to the development of the low-pressure anomaly to the west of our heatwave area. This could then weaken the Shamal wind as a result of the corresponding reduction of the east-west

The results of this section are published in AL-Shamarti, H., P. Rupp, and T. Birner. 2025. "Circulation Aspects Associated With Heatwave Events Over Iraq." International Journal of Climatology e70017. https://doi.org/10.1002/joc.70017.

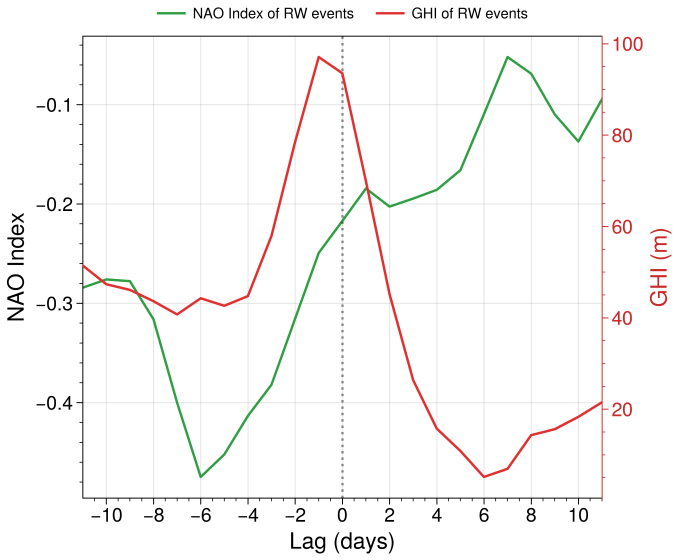

Figure 3.17: Composite-mean evolution of heatwave events of RW cluster. Shown are the North Atlantic Oscillation index NAO and GHI, GHI: geopotential height anomaly at 200 hPa averaged over the center anticyclone (40-60°E, 37-55.5°N) of the RW events.

pressure gradient across our heatwave area.

Furthermore, the Sudanese Low (SL) and Red Sea Trough (RST) are known to exhibit strong variations, both in intensity and location (El-Fandy, 1950; Krichak et al., 2012). These low-pressure systems may contribute to the low-pressure anomaly to the west of our target area during the Non-RW events.

Although the above points are speculative, they are somewhat supported by the observed cloud cover pattern anomalies (see Figure 3.12b). For example, the elevated cloud fraction in the western part of our target area supports our speculation. Furthermore, the evolution of geopotential height anomalies at 1000 hPa illustrates the intensification of the SL center (Fig. 3.18).

In conclusion, heatwaves in southern Iraq are typically associated with a weakening of the northerly-northwesterly winds (Shamal wind), which under climatological conditions induces a persistent cooling effect. Different mechanisms can weaken the Shamal wind: one possibility is circulation anomalies induced by anticyclones embedded in quasi-stationary synoptic Rossby waves that travel on the African-Asian jet. Another possibility is a change in the local pressure gradient driving the Shamal wind, for example, by an anomalous shift of the SL and/or RST (Fig. 3.19).

Despite the insights gained in this study, additional questions remain. For example, the Indian monsoon is known to influence regional circulation patterns over the Eastern Mediter-

The results of this section are published in AL-Shamarti, H., P. Rupp, and T. Birner. 2025. "Circulation Aspects Associated With Heatwave Events Over Iraq." International Journal of Climatology e70017. https://doi.org/10.1002/joc.70017.

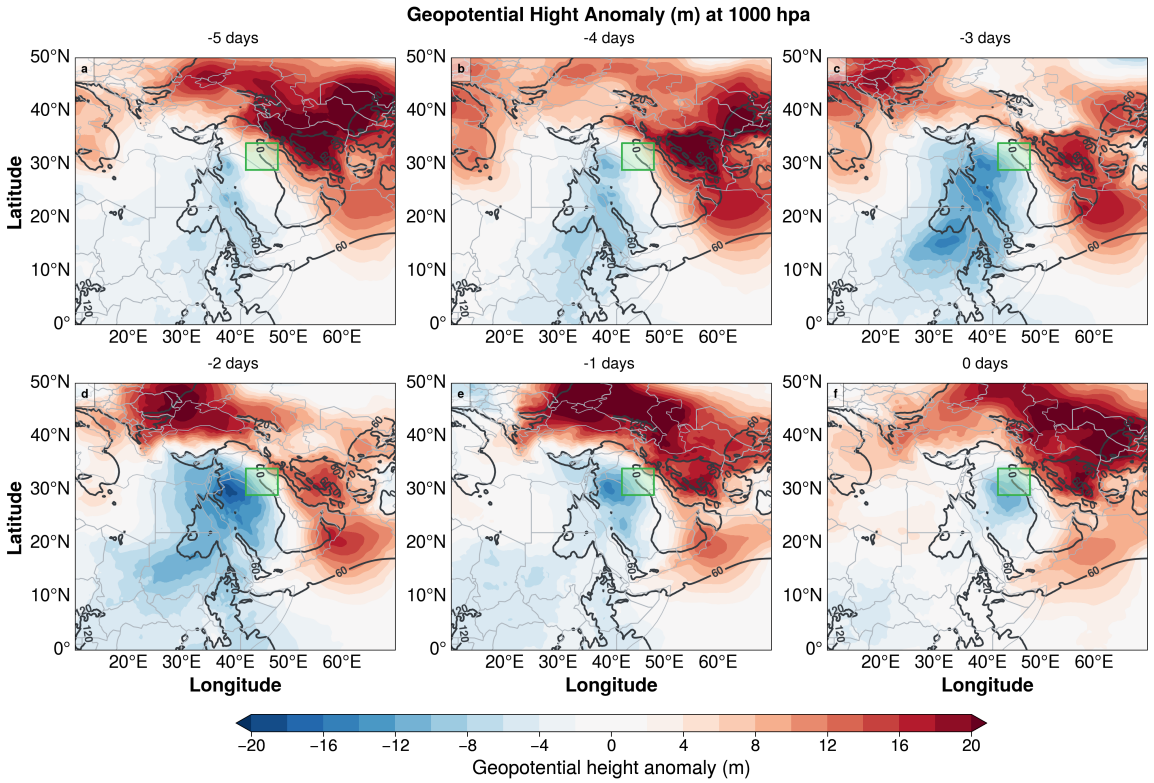

Figure 3.18: Composite-mean evolution of geopotential height anomalies (shading) with Climatology (contour, unit : (m) at 1000 hPa of Non-RW events. The green boxes mark the heatwave area.

ranean and the Middle East (Tyrlis et al., 2013), potentially modulating the Shamal wind. However, a preliminary analysis (not shown) did not reveal a robust link between monsoon activity and the strength of the Shamal wind during heatwave events. This lack of a clear connection may be due to limitations in data coverage or the specific timescales considered. Further investigations using more extensive datasets and targeted analyses are necessary to better understand the potential relationship between the Indian monsoon and Shamal wind variability.

In future research, improving understanding of the dynamical drivers of heatwaves could help enhance medium- to extended-range forecasts, which would aid in the development of adaptive strategies. These could include better early warning systems, urban planning adaptations, and regional disaster management plans to mitigate the impacts of heatwaves, particularly in vulnerable areas.

The results of this section are published in AL-Shamarti, H., P. Rupp, and T. Birner. 2025. “Circulation Aspects Associated With Heatwave Events Over Iraq.” International Journal of Climatology e70017. https://doi.org/10.1002/joc.70017.

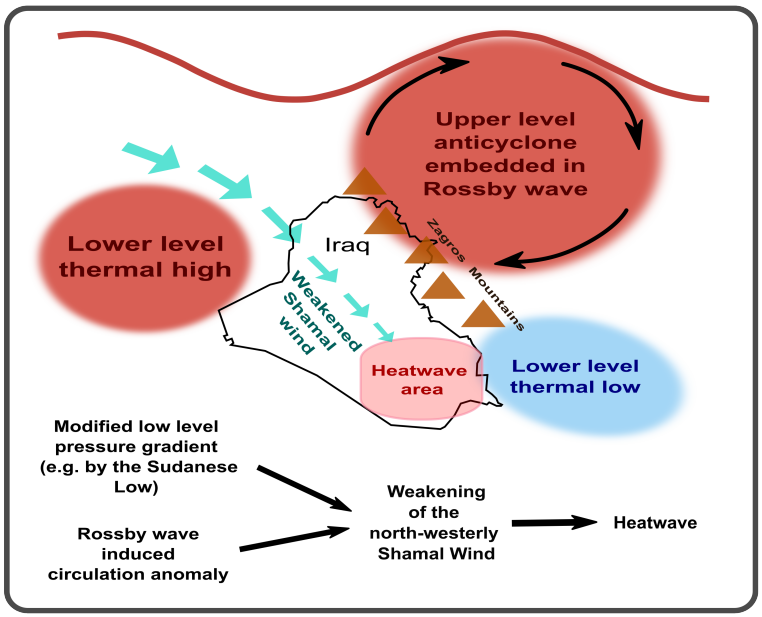

Figure 3.19: Schematic of two southern Iraqi heatwave mechanisms involving a weakening of the predominant near-surface Shamal wind. An upper-level quasi-stationary anticyclone, embedded in a Rossby wave, can modify the synoptic scale system via downward influence. Further, a change in the local lower-level pressure gradient can directly weaken the Shamal wind.

The results of this section are published in AL-Shamarti, H., P. Rupp, and T. Birner. 2025. "Circulation Aspects Associated With Heatwave Events Over Iraq." International Journal of Climatology e70017. https://doi.org/10.1002/joc.70017.

Chapter 4

Prediction of Heatwaves Using Subseasonal to Seasonal (S2S) Forecasting

We investigate sub-seasonal to seasonal (S2S) data to analyze heatwaves and assess their predictability on S2S timescales. The key advantage of this approach is that the S2S predictability time scale (with lead times of 2 to 6 weeks) is enhanced by remote phenomena and the interactions between the atmosphere and the Earth's surface. Another important advantage is that the availability of many ensemble members enhances our understanding of the physical drivers behind heatwave events. In this chapter, in addition to assessing the predictability performance of heatwave events, we examine a selected case study to compare the predicted physical drivers with those identified from reanalysis data.

4.1 Background on Numerical weather prediction (NWP)

Numerical weather prediction (NWP) employs atmospheric models based on fundamental physical laws—such as the conservation of mass, momentum, and energy—to forecast the weather. These models solve complex dynamical equations on a discrete spatial grid representing the Earth's atmosphere. First attempted by Lewis Fry Richardson in 1922, NWP was initially constrained by insufficient computational resources but laid the foundation for modern forecasting (Richardson, 1922). Today, NWP relies on precise initial conditions derived from comprehensive observational data, which are assimilated to create the best possible estimate of the current atmospheric state. The forecast then evolves step by step through numerical solutions of the governing equations (Coiffier, 2011).

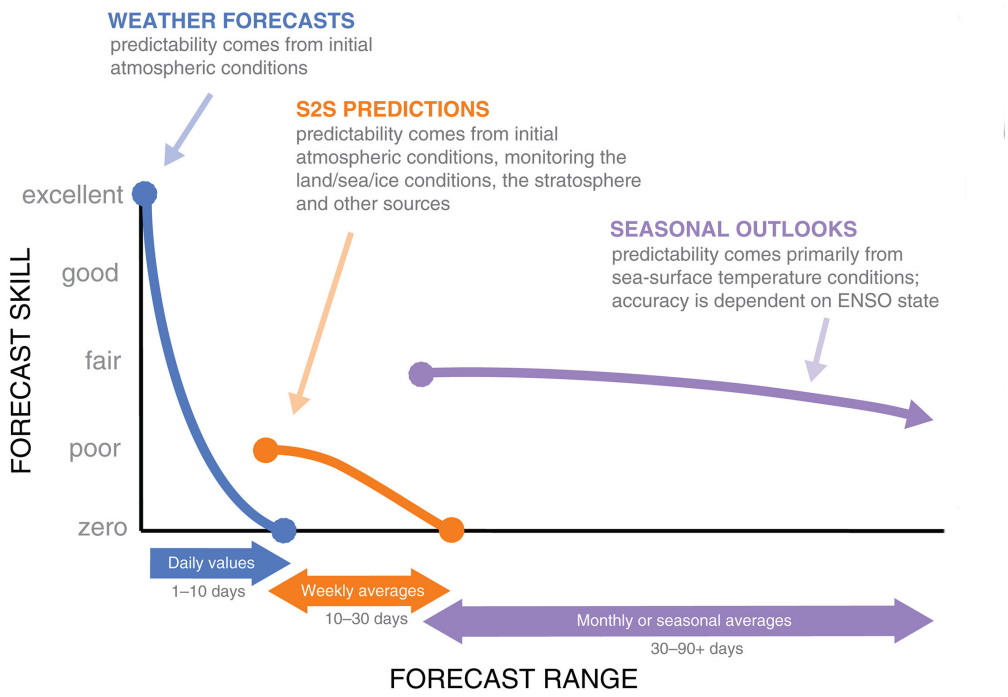

Figure 4.1: Qualitative assessment of forecast skill across different forecast ranges, from short-range weather predictions to long-range seasonal outlooks, highlighting key sources of predictability. The relative skill is evaluated based on varying forecast averaging periods (White et al., 2017).

Despite significant advancements, NWP remains constrained by uncertainties in initial conditions—often due to observational gaps or measurement errors—and by inherent model limitations, particularly in representing small-scale processes like cloud microphysics, turbulence, and radiative interactions (Wu and Xue, 2024). Sub-grid-scale processes, which cannot be explicitly resolved, are approximated through parameterization schemes that capture their effects on larger-scale atmospheric dynamics. NWP models calculate key atmospheric variables—pressure, temperature, wind, humidity, and precipitation—on a three-dimensional grid, where forecast accuracy generally improves with higher spatial resolution (Smith et al., 2021; Gultepe et al., 2019).

Although NWP has greatly benefited from increased computational power and model sophistication, its predictability remains inherently limited. In general, reliable forecasts extend up to about one week, with accuracy declining beyond 10 days due to the chaotic nature of the atmosphere. For longer timescales, such as seasonal forecasting, accuracy depends on slower-evolving aspects of the Earth system components—such as sea surface temperatures (SST), soil moisture, and sea ice, which provide a more stable basis for extended predictions.

4.2 Subseasonal to Seasonal (S2S) of ECMWF Forecast

The gap between short- to medium-range weather forecasts and seasonal forecasts has created a significant demand for predictions covering periods from two weeks to two months (Fig. 4.1). This need led to the establishment of the **Subseasonal to Seasonal (S2S)** forecasting initiative in 2013, developed by the World Weather Research Programme (WWRP) and the World Climate Research Programme (WCRP). A pioneering attempt at sub-seasonal forecasting demonstrated the ability to reproduce notable atmospheric events (blocking events) using one-month forecasts generated by a General Circulation Model (GCM) (Miyakoda and Sirutis, 1985). The S2S initiative aims to bridge the forecasting gap between weather and climate predictions by providing valuable outlooks for intermediate timescales (2–6 weeks). These forecasts support decision-making in sectors sensitive to weather variability—such as agriculture, water management, and disaster preparedness—by incorporating remote drivers that influence the likelihood of extreme temperature events (Lang et al., 2020; White et al., 2017).

Additionally, some S2S models provide high-resolution spatial grids, which are expected to enhance their ability to capture small-scale atmospheric processes. These advantages may be crucial for identifying local climate variations, including temperature anomalies, humidity levels, and wind directions. As a result, S2S forecasts are expected to improve the accuracy of heatwave predictions in specific regions. In this thesis, we use ensemble forecasts from the ECMWF model within the S2S database primarily as a data source. Our key motivation is to exploit the ensemble spread, which becomes meaningful beyond the 10-day forecast range and allows for a probabilistic assessment of heatwave predictability. The ECMWF model was selected for its high spatial resolution and large ensemble size relative to other S2S models. This selection also enables direct comparison and validation against results derived from ERA5 reanalysis data.

ECMWF forecasts types

S2S forecasts of ECMWF models provide two types of forecasts:

1. Real-time forecasts: Predictions for upcoming days, generated twice weekly (Mondays and Thursdays at 00Z) using 51 ensemble members (50 perturbed and 1 control).
2. Re-forecasts (hindcasts): Retrospective forecasts covering the past 20 years, initialized on the same calendar day as the real-time forecasts. These are run with 11 ensemble members (10 perturbed and 1 control) to support the calibration and verification of real-time predictions.

However, the data have been obtained from various Integrated Forecast System (IFS)

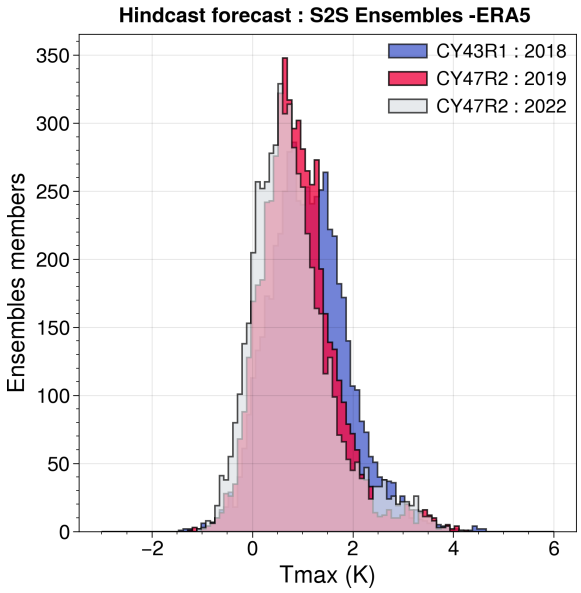

Figure 4.2: Distribution of the bias of hindcast Tmax anomalies (K) of S2S ensemble forecasts compared to ERA5 for different IFS cycles CY43R1 (2018, blue), CY47R2 (2019, red), and CY47R2 (2022, gray).

cycles. Since our heatwave events span from 1980 to 2022, we used in this thesis all available past IFS cycles to cover the full period of interest. This approach ensures that we include as much historical forecast data as possible, despite the differences between IFS versions over time. These IFS cycles are as follows:

- **IFS CY43R1**: Implemented on November 24, 2016, its reforecasts were built using initial conditions derived from ERA-Interim (T255L60), Soil Reanalysis (Tco639), and ORAS5 ocean initial conditions, with a horizontal resolution of 0.25 degrees.
- **IFS CY46R1**: Implemented on June 11, 2019, this cycle transitioned to ERA5 for atmospheric initial conditions while maintaining ORAS5 for ocean initial conditions and a 0.25-degree resolution.
- **IFS CY47R2**: Introduced on May 11, 2021, this cycle also utilized ERA5 and ORAS5 but featured an increased vertical resolution of 137 sigma levels, compared to the 91 levels used in the previous cycles.

The horizontal resolution of all forecasts is Tco639 (∼16 km) for the first 15 days and Tco319 (∼32 km) beyond that period, while the ocean model employs NEMO with a 0.25-degree resolution*. Figure 4.2 illustrates the Tmax anomalies bias (more details about Tmax in

*More details found in `https://confluence.ecmwf.int/display/S2S/ECMWF+model+description` .

Section 4.3) of each IFS cycle compared to ERA5. It shows that the IFS initialized with ERA-Interim has ensemble forecasts that are significantly warmer than ERA5 compared to other cycles, which also exhibit a warm bias.

For real-time forecasts, all cycles employed operational initial conditions derived from the ECMWF's Ensemble of Data Assimilation (EDA) and Ensemble Forecast Systems (EFS). The EDA system generates perturbed members to estimate a background error covariance matrix, enhancing the accuracy of the subsequent analysis cycle. These perturbed analyses also contribute to initializing the EFS (Isaksen et al., 2010). The high-resolution forecasts and re-forecasts demonstrate ECMWF's commitment to improving S2S predictability by utilizing advanced data assimilation techniques, consistent initialization frameworks, and detailed parametrization. This approach ensures robust operational forecasts and valuable datasets for research purposes.

4.3 Data Handling

The ECMWF S2S ensemble forecasts provide daily-averaged temperatures; however, our heatwave definition is built on daily maximum temperatures derived from hourly reanalysis data, which is inconsistent with these forecast data types. To address this discrepancy, we used the other type of S2S data provided by ECMWF, known as instantaneous and accumulated data. Specifically, we calculated daily Tmax from the maximum 2-meter temperature over the last 6 hours (***mx2t6***). This calculation was applied to all instantaneous data.

As we mentioned in 4.2, we use different IFS cycles to maximize historical forecast data coverage, thereby increasing the number of ensemble members for each event by combining real-time forecasts with their corresponding hindcasts. This advantage increases the size of the ensemble for each heatwave event, improving the robustness of the analysis. As a result, any event occurring within the real-time forecast period could include up to 51 ensemble members, with an additional 11 or more members depending on the hindcast initialization days (e.g., Monday and Thursday). This approach enhances the accuracy of estimating the fraction of members capturing heatwave events. Moreover, it ensures broader coverage across forecast lead times, mitigating data gaps associated with specific initialization days.

4.3.1 Deseasonalization of S2S Forecast Data

The performance of deseasonalizing S2S forecast data is built on the existence of 20 years of hindcast data from the S2S ECMWF model system. This extensive range of forecast data

is highly effective for computing the climatology of the forecast data. The deseasonalization process was performed as follows (Spaeth and Birner, 2022):

1. **Compute Ensemble Means**: Calculate the mean for each ensemble of each hindcast year as a function of the lead time.
2. **Compute climatological Means**: Calculate the annual mean of the ensemble forecasts over the 20 hindcast years as a function of the lead time.
3. **Create Window of climatological Means**: Establish a window of annual mean hindcasts within $\pm 14d$ days relative to the date d that the forecast starts in. Given that ECMWF forecasts are available twice a week (Monday and Thursday), this results in 9 initializations over the window selection.
4. **Match Valid Times**: Average the hindcasts from step 3 such that the forecast valid times align (e.g., average forecasts for 10 June, 11 June, etc., rather than matching forecast lead times such as lead times of +4, +5 days, etc.).
5. **Apply Running Mean Filter**: Apply a 7-day running mean filter to the resulting time series.
6. **Trim Time Series**: Due to the window of running mean is ±14-day, the resulting time series starts earlier than date d and covers a period longer than the forecast of interest. Trim the time series at the beginning and end to match the forecast period of interest, thus providing the climatology.
7. **Anomaly calculation**: subtract the climatology from the Total field.

4.4 Predictability of ERA5-based Events

The S2S ensemble forecast dataset used in this study includes real-time forecasts spanning 2018–2022, combined with their associated hindcasts covering the preceding 20 years. Consequently, the earliest hindcast year is 1998. Based on this period, the analysis includes 22 events from the RW cluster and 6 events from the Non-RW cluster. To assess the model's skill for each event, we defined **Truth** of the anomaly of Tmax and geopotential heights forecasts based on the real-time forecasts initialized on (or close to within 2 days) the central day of each event. In other words, the **Truth** is derived from the S2S model itself. This approach mitigates the biases between the S2S model and ERA5 reanalysis data. For instance, Figure 4.3 compares just a single IFS cycle obtaining its initialization from ERA5 with the ERA5 dataset averaged over summer months individually. It illustrates that the S2S model is warmer over mountainous regions compared to ERA5, highlighting the importance of considering the complex topographical structures when assessing model

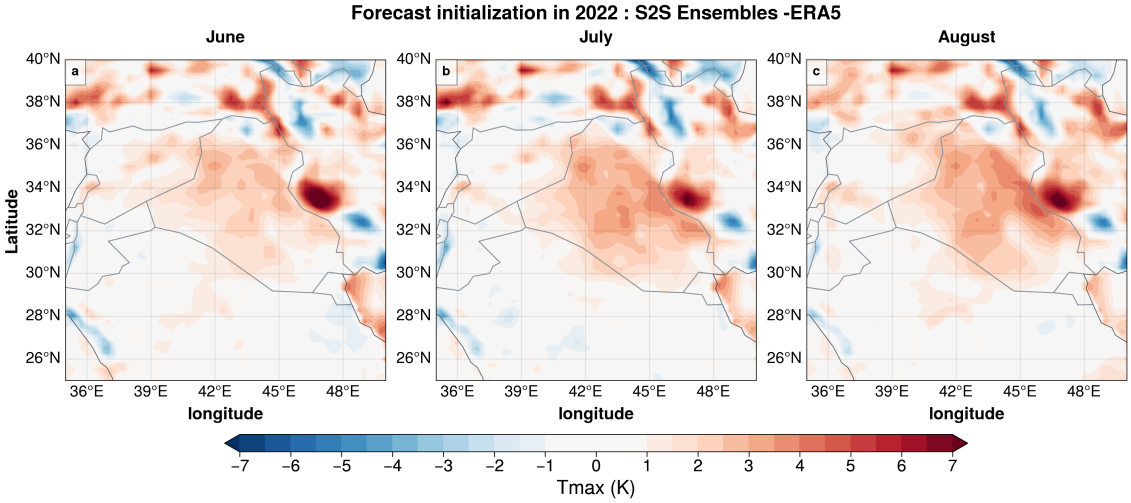

Figure 4.3: Spatial difference of Tmax anomalies at the first day of the lead time of the ensemble mean of real-time forecasts, and ERA5 on the same day. The results are averaged monthly for 2022: (a) June, (b) July, and (c) August.

performance. Indeed, we use the S2S model itself to define the **Truth**, since the system is built on the EDA/EFS framework, which is specifically designed to reduce bias and minimize initialization errors (see 4.2). The **Truth** computed of Tmax anomalies averaged over our target area and the geopotential height anomaly index (i.e., GHI index, see Chapter 3). Our analyses focus on the following skill metrics, which are discussed in the following subsections:

Root Mean Square Error metric

The Root Mean Squared Error (RMSE) is a widely used metric to assess the forecast skill of a model. In this study, we computed the RMSE for each event relative to its **Truth**. The RMSE provides a quantitative measure of the discrepancy between the predicted values and the actual reference values. To evaluate the forecast skill of the ensemble model, we followed the procedure as below:

1. **Step 1**: For each event e and each ensemble member i, the error is calculated as:

$$\text{Error}_{i,e} = T_{i,e} - T_{\mathbf{Truth},e} \tag{4.1}$$

where:

- $T_{i,e}$ is the forecasted Tmax anomaly from the i-th ensemble member for event e.

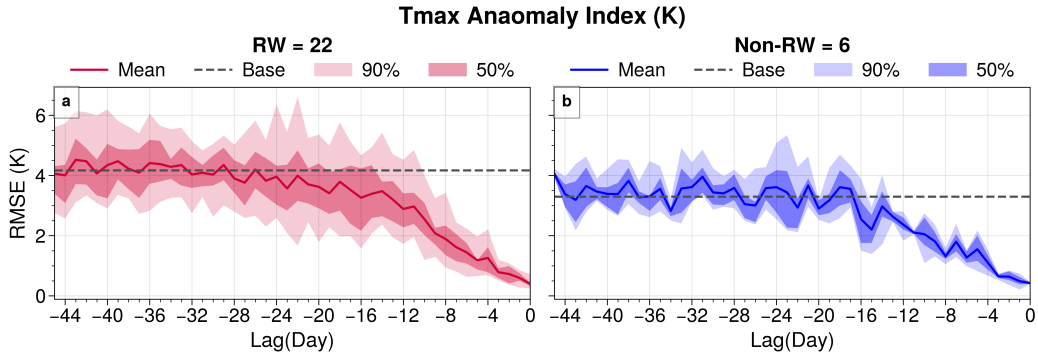

Figure 4.4: RMSE of Tmax anomalies. The solid line represents the averaged RMSE over all available events of each cluster. Shading colors indicate the ensemble member distribution events of RMSE. The dashed gray line indicates the baseline RMSE. a) represent the Rossby wave events (RW), b) Non-Rossby wave events (Non-RW).

- $T_{\mathbf{Truth},e}$ is the actual reference value **Truth** of the event that obtained from S2S model.

2. **Step 2**: The $RMSE_e$ for a single event e is calculated as:

$$\mathrm{RMSE}_e = \sqrt{\frac{1}{N_m}\sum_{i=1}^{N_m}(\mathrm{Error}_{i,e})^2} \tag{4.2}$$

where:

- N_m is the total number of ensemble members.

3. **Step 3**: The mean RMSE across all N_e events is calculated as:

$$\mathrm{RMSE} = \sum_{e=1}^{N_e}\mathrm{RMSE}_e \tag{4.3}$$

where:

- N_e is the total number of heatwave events considered.

This methodology ensures that the accuracy of the forecast is comprehensively evaluated in multiple events and members of the ensemble. Figure 4.4 shows the RMSE of Tmax anomalies of both heatwave events clusters. The baseline RMSE, dashed lines in Figures 4.4 and 4.5, is defined as the mean RMSE calculated over the extended lag times from -46 to -25, serving as a reference of model performance. Hence, we consider the model to perform well when the RMSE remains significantly lower than this baseline (for Tmax

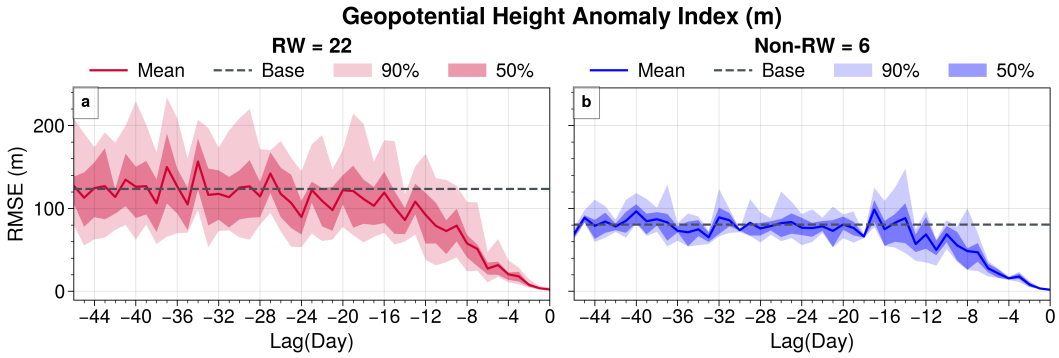

Figure 4.5: Similar of figure 4.4 however of geopotential height index.

anomalies less than ≃4K of RW and ≃3K of Non-RW). Based on this criterion, the RMSE of Tmax anomalies shows a steady decline in two weeks before the event for both heatwave clusters, suggesting that the model performs well within this short-range predictability window. In RW events, the RMSE begins to deviate significantly from the baseline at lag-28, which is the longer range in forecast than for Non-RW events, where the deviation occurs around lag-16. Beyond these reference points (i.e., before lag-28 for RW and lag-16 for Non-RW), RMSE fluctuates around the baseline, suggesting a drop in forecast skill with increasing longer-range forecasts. The relatively extended predictability window for RW events is likely due to the intrinsic predictability of large-scale Rossby wave dynamics in the S2S model (Fig. 4.4a), which evolve more slowly than the smaller-scale processes that dominate Non-RW events. In contrast, Non-RW events show less variability in the ensemble members' distribution of RMSE across lag times (see shading in Fig. 4.4b). This stable pattern is likely associated with limited predictability rather than high confidence. The small sample size of Non-RW events reduces statistical confidence in assessing variability and may limit the model's ability to capture and respond to the physical drivers of these events, contributing to challenges in predictability.

Interestingly, the RMSE values for both clusters at lag 0 remain higher than zero. This may be partly due to the initial definition of the **Truth**, which in some events did not occur exactly on the initialization day but rather around lead time day 2. This temporal mismatch can artificially inflate the RMSE at lag 0.

Similarly, the S2S model shows increased uncertainty (i.e., close to baseline) in the GHI index for longer-range predictions (Fig. 4.5). The RMSE for RW events tends to be more variable than that for Tmax anomalies; however, beyond lag-28, it fluctuates near the baseline, closely matching the RMSE observed for Tmax anomalies (cf. Fig. 4.5a and 4.4a). This similarity is associated with the large-scale atmospheric dynamics governing these heatwave events, which strengthens the consistency in predictability across both temperature and circulation-related indices. In contrast, the RMSE for Non-RW events shows certainty just in the first week of prediction, which is consistent with the previous

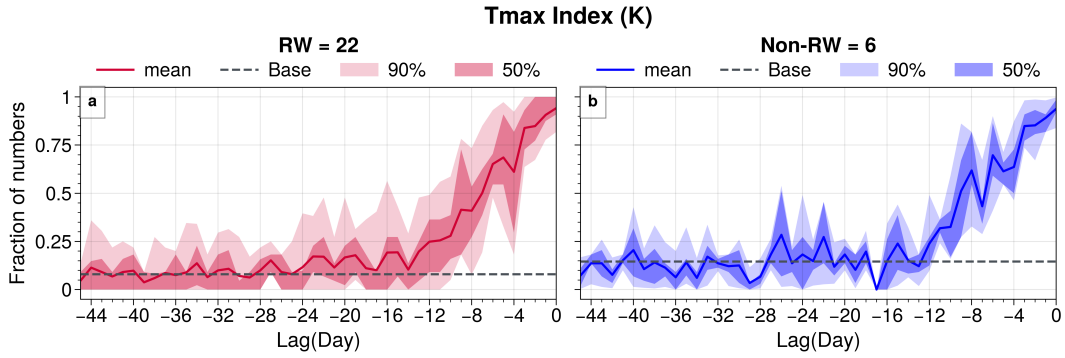

Figure 4.6: Fraction of ensemble members. Solid lines refer to the mean of the fraction of the members that capture the events of all the events, dark shadings and light shadings refer to the 50% and 90% of the members that capture the events, respectively. a) represent RW events, b) Non-RW events.

results that these events are driven by different physical processes that are less influenced by large-scale circulation dynamics (Fig. 4.5b).

Fractional Truth-Based Threshold Metric

The other skill metric is Fractional Truth-Based Threshold. The Fraction of **Truth** was employed as the skill metric, where 80% of the **Truth** for each event was set as a threshold to evaluate the forecast skill. This approach shows results in agreement with those obtained from RMSE. For example, the model performs well in short-range forecasts (i.e., 2 weeks in advance) for both clusters of Tmax anomalies (Fig. 4.6). During the first week, most ensemble members successfully captured the heatwave events. However, in longer-range forecasts—particularly after lag day -14 for RW events—the model's predictions of Tmax anomalies begin to approach the baseline, reaching it around lag day -28, where predictability becomes indistinguishable from the baseline. This behavior is consistent with the RMSE pattern (cf. Fig. 4.6a and 4.4a).

However, the models' predictions of Non-RW tend to close and fluctuate around the baseline at lag-12. Once again, the forecast appears uncertain for Non-RW events, as indicated by the increasing variability of the metric even in short-range forecasts. This supports our earlier argument that the smaller sample size reduces statistical confidence (Fig. 4.6b).

Figure 4.7 shows both clusters' fractional **Truth** metric for the GHI index. As expected, the metric confirms that the S2S model successfully predicts events driven by large-scale circulation (RW events) (Fig. 4.7a). In contrast, the model struggles to predict the index when large-scale circulation does not play a significant role. Furthermore, the forecast appears uncertain for Non-RW events, with predictions generally fluctuating around the

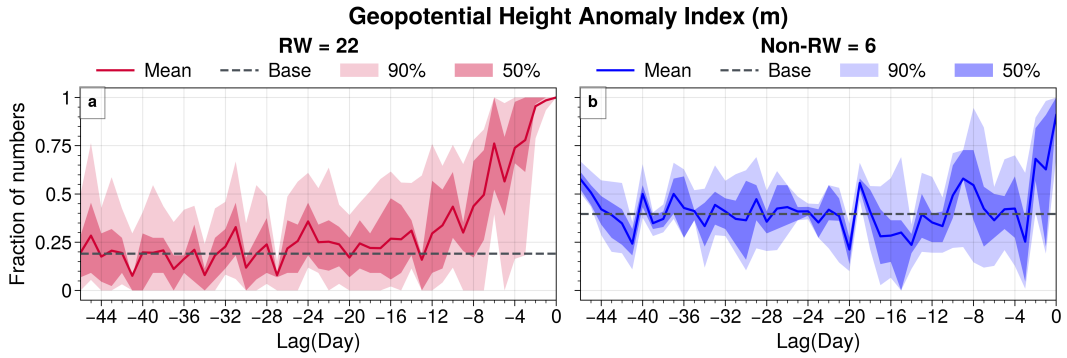

Figure 4.7: Similar of figure 4.6 however of geopotential height index.

baseline across all lag times (Fig. 4.7b). Based on these two metrics, we categorized the ensemble forecast members into those that successfully captured the events and those that did not. We then examined these classifications using the forecast numbers that were obtained from the fractional truth approach to reveal the physical mechanisms driving the ensemble forecasts.

Figure 4.8 illustrates the composite-mean of the upper-level circulation at 200 hPa for the forecast numbers that capture the events of both clusters. In RW events, the S2S model accurately predicts quasi-stationary upper-level anticyclonic anomalies to the north of our target area (4.8a and b). These anticyclonic anomalies (contour lines) are embedded in the Rossby wave train in the Northern Hemisphere during the first week of forecasts (Fig. 4.8a). This configuration is consistent with the physical drivers of these events that we analyzed in Chapter 3. In the second week, although the model seems to predict less accurately, the anticyclonic high anomalies and the Rossby wave are still pronounced (Fig. 4.8b). This emphasizes our results from the skill modules of the S2S model using RMSE and Fractional Truth.

On the other hand, the S2S model shows a potential dipole of geopotential height anomalies over the Mediterranean and Europe for Non-RW events during the first week of forecast (Fig. 4.8c). This pattern suggests that another physical driver of these events may be associated with these anomalies. The high geopotential anomalies over the Mediterranean remain unclear in terms of their connection to the likely wave structure (cf. shading and contours in Fig. 4.8c). Indeed, this wave structure (shading) may reflect uncertainty arising from the limited number of available samples, which reduces the reliability of the signal. In contrast to RW events, the S2S model shows poor predictive performance for heatwaves that are not linked to large-scale circulation anomalies (Non-RW), particularly in the second week. While RW events retain some predictability due to persistent large-scale atmospheric patterns, the model struggles to capture key upper-level features for Non-RW events after the first week. For example, the expected dipole pattern in geopotential height disappears, and the high-pressure anomalies over the Mediterranean weaken significantly

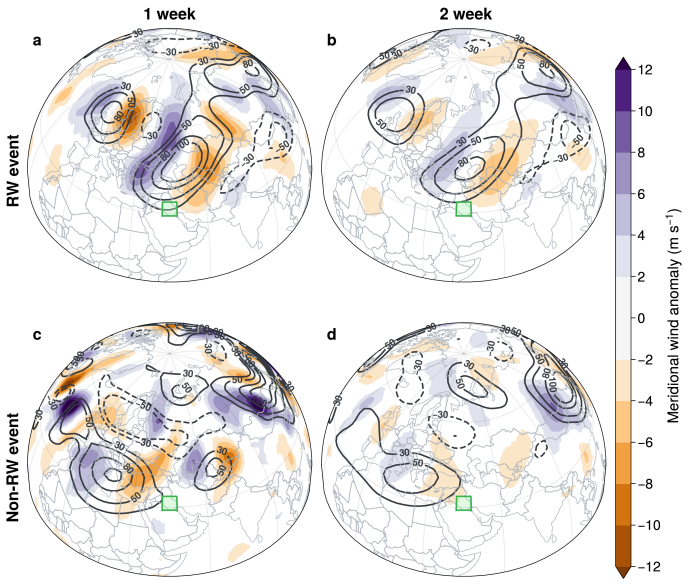

Figure 4.8: Composite-mean evolution of meridional Wind anomalies (shading) and geopotential height anomalies (contours) at 200 hPa of only members that capture the events. **a** and **b**: RW events, **c** and **d**: Non-RW events. **a** and **c**: first lagging week of the events, **b** and **d**: second lagging week of events. The green and red boxes mark the heatwave area.

(Fig. 4.8d). Additionally, meridional wind anomalies, which were evident in the first week, became negligible in the second week, suggesting a rapid loss of forecast skill for these types of events.

4.4.1 Discussion

The S2S model demonstrates strong predictive skill for Tmax anomalies (and then heatwave events) in both event clusters during short-range forecasts, as evaluated using RMSE and fractional **Truth** skill metrics. However, the model loses skills in longer-range forecasts. Despite the limited statistical sample size of Non-RW events, these metrics indicate reliable forecasts within the first two weeks, similar to RW events, which are driven by large-scale circulation. This suggests that while the model effectively captures large-scale dynamics, it may also have some skills to predict smaller-scale physical processes that contribute to heatwave evolution.

This estimation is further supported by the GHI index skill assessment, which indicates that the S2S model remains reliable only within the first four lag days for Non-RW events—an expected outcome, since these events are driven by mechanisms other than Rossby waves. In contrast, the model shows extended skill in forecasting Rossby wave–driven heatwaves

(RW events) up to two weeks in advance. Moreover, the forecast members that successfully captured these events continue to show anticyclonic anomalies embedded within the Rossby wave even in the second week, consistent with our findings in Chapter 3.

4.5 Case Study of a Heatwave Event and its subseasonal predictability

A heatwave event centered on 2 June 2006, from the ERA5-based composite results, was selected to examine the specific atmospheric dynamics associated with this event, verify that the composite patterns are reflected in individual cases, and provide a basis for evaluating the performance of forecasts against observed behavior. This event was particularly appropriate for S2S analysis due to its significant duration and intensity, as well as the availability of abundant ensemble forecast data for its period, thereby enhancing the evaluation of heatwave predictability. Furthermore, it was observed in most of the observational datasets (i.e., events obtained from station data as Section 2.3), which further supports its selection. Another advantage is the presence of a subsequent heatwave event 11 days after the selected case, which allows for a comparative analysis of anomaly patterns in certain variables, such as Shamal wind, using ERA5 data.

4.5.1 Observed Evolution based on ERA5

To maintain the contextualization that we followed in Chapter 3, we will use the same analysis approach in terms of the sequence of the selected variables to analyze our selected event that was obtained from ERA5-based composite results. Starting with Figure 4.9, it shows Tmax anomalies averaged over the 4 days preceding the event's onset and during the event itself. The anomalies began extending across western Turkey and the northern Arabian Peninsula before the event (Fig. 4.9a). However, the anomalies intensified over Iraq, expanding further northward during the event (Fig. 4.9b). This pattern may explain why the event was not extended in the far south of our target area based on observational data. In Figure 4.9b, the Tmax anomalies exhibit a pronounced north–south contrast $\approx$3-7K relative to the climatology ($\simeq$319K, see the contour line in Fig. 4.9b), highlighting the significant influence of mesoscale processes and the complexity of the topography. The anomalies extend across a broad region toward the north, with particularly high anomalies over the mountains of Turkey $\approx$7-8K, compared to its climatology $\simeq$300K. Nevertheless, the heatwave event tends to be more pronounced in Iraq.

Furthermore, cold anomalies are observed over the Iranian Plateau during the event, suggesting a dipole-like pattern in contrast to the strong warming over Iraq. This contrast may be related to the influence of the Indian summer monsoon upper-level anticyclone

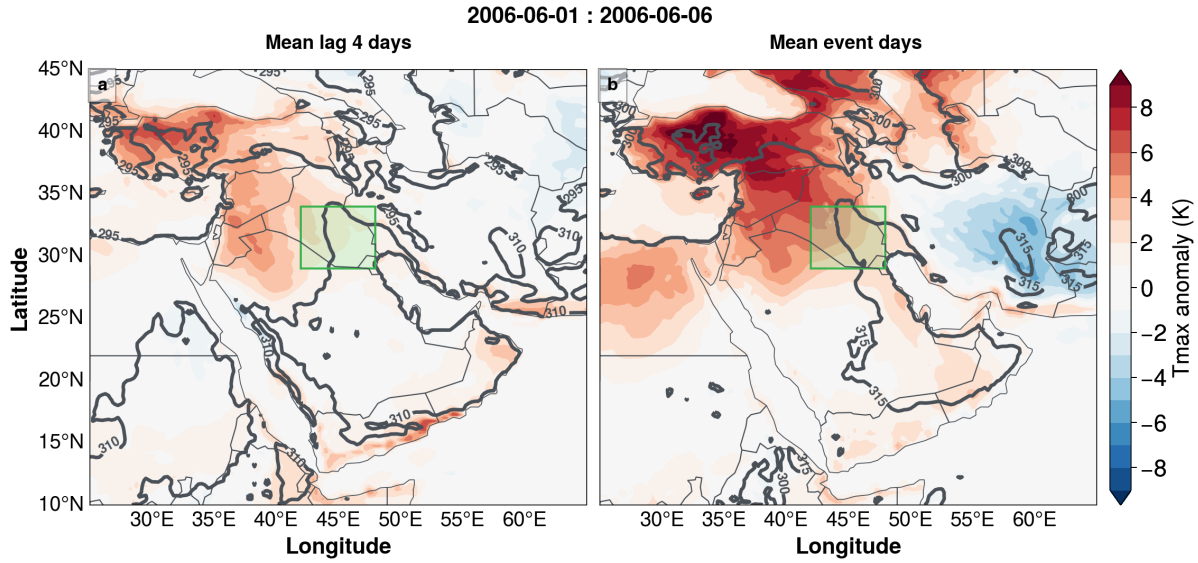

Figure 4.9: Evolution of Tmax anomalies (shading) with climatology(contour, units : K). a) Averaged over 4 days preceding the onset of the event with May climatology(contour). b) Averaged over the event itself with June climatology(contour). The green box marks the heatwave area.

or other regional processes such as topographic and land–atmosphere interactions. This observation raises important questions about the mechanisms driving the heatwave and its connection to upper-level circulation patterns.

To explore the mechanisms, similar to our analysis in Chapter 3, we investigate the geopotential height anomalies to examine the upper-level large-scale atmospheric dynamics associated with this heatwave event.

Figure 4.10 illustrates the evolution of upper-level geopotential height anomalies and meridional wind anomalies at 200hPa. Preceding the event, the upper-level anomalies appear to be displaced far north, around 60°N, which is associated with the North Atlantic jet (Fig. 4.10c). As expected, the meridional wind anomalies exhibit a Rossby wave train propagated approximately at 60°N before the heatwave event guiding initially by the North Atlantic jet which traps the wave at higher latitudes (Fig. 4.10c). During the event, this wave shifts southward, becoming confined between 30°N and 60°N before its exiting near the monsoon region (cf. Fig. 4.10c and d). This propagation pattern is attributed to the African-Asian jet, which extends over broad regions and acts as a crucial waveguide for the Rossby wave during the event (Fig. 4.10c). In contrast, the upper-level anticyclone associated with the summer monsoon seems to strengthen before the event, potentially influencing deep convection in the lower troposphere near our target area (Fig. 4.10a). During the event, upper-level anomalies intensify and expand over a broad region, shifting toward lower latitudes (Fig. 4.10b). Notably, the anticyclonic anomalies extend over

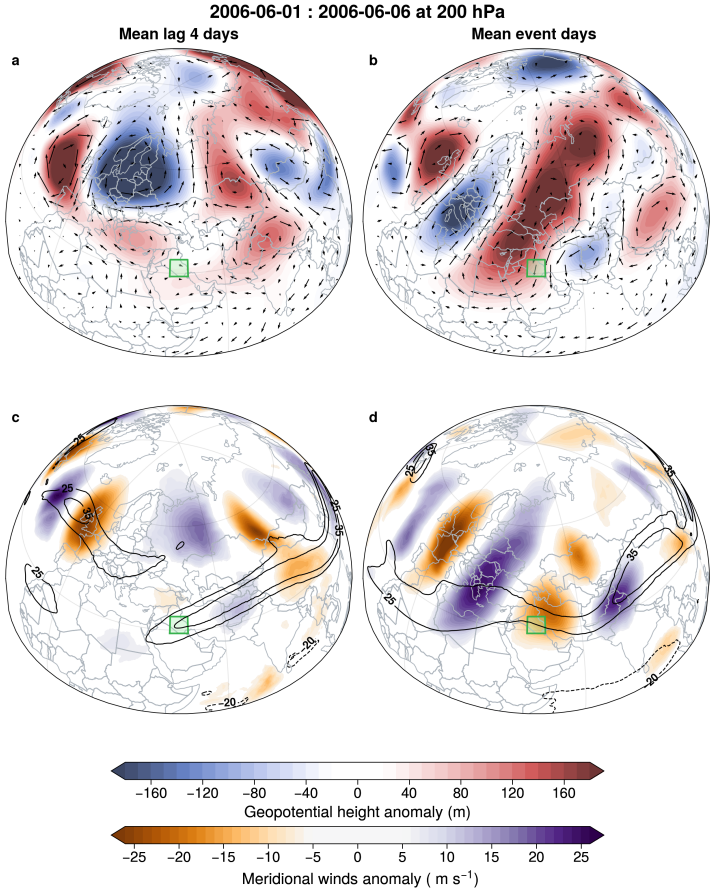

Figure 4.10: **a** and **b**: Evolution of geopotential height anomalies (shading) and horizontal wind anomalies (arrows). **c** and **d**: Evolution of meridional Wind anomalies (shading) and total Zonal Wind (contours, units: m/sec). All fields are shown at 200 hPa. Averaged over 4 days preceding the onset of the event (a,c) and averaged over the event itself (d,c). The green box marks the heatwave area.

the Arabian Peninsula, reaching our target area. This configuration reveals a wave-like structure that extends from mid-latitudes to lower latitudes, with the pressure anomalies embedded within this structure (Fig. 4.10b). This structure suggests long-wavelength wave dynamics in shaping the atmospheric conditions during the event.

The influence of Rossby wave evolution extends beyond the upper troposphere, affecting both the mid- and lower troposphere. Figure 4.11 illustrates pressure system anomalies in the mid- and lower-troposphere that coincide with the Rossby wave evolution observed at upper levels. These pressure systems, embedded within the Rossby wave, appear to extend into the lower troposphere without a noticeable vertical tilt, suggesting the presence of a barotropic wave. Figure 4.11a reveals the presence of a pressure gradient between the positive geopotential height anomalies at 500 hPa over the eastern Mediterranean with the

low-level thermal low extending over the Gulf, which is declared at 850 hPa (Fig. 4.11 a). This pressure gradient, which was more pronounced before the event, mostly formed due to the influence of the high terrain of the eastern Mediterranean and the thermal low at lower levels.

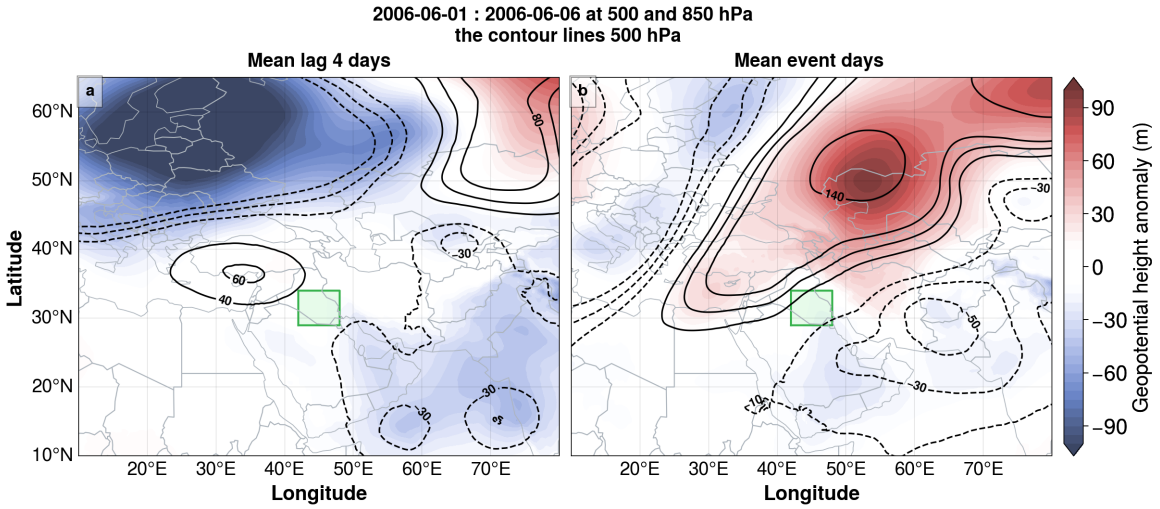

Figure 4.11: Evolution of geopotential height anomalies at 500 hPa (contours) and at 850 hPa (shading). a) Averaged over 4 days preceding the onset of the event. b) Averaged over the event itself. The green box marks the heatwave area.

During the event, the high geopotential height anomalies are synchronized with those at the upper level (Fig. 4.11b). As a result, the Eastern Mediterranean is influenced by these anomalies, which likely contribute to changes in the local pressure system on a synoptic scale. Despite the strengthening of local positive anomalies over the eastern Mediterranean as a result of the spanning of the upper-level anticyclonic system to a lower level during the event, which would typically enhance the pressure gradient, the thermal low weakens during the event (Fig. 4.11b). This weakening of the thermal low is also associated with the attenuation of the Shamal winds, as discussed in Chapter 3. In addition, anticyclonic anomalies in the mid- to lower troposphere over Iraq boosted the subsidence and then the adiabatic warming process (contour lines in Fig. 4.11b).

The thermodynamic anomaly variables provide further evidence of the thermal low modification in synchronization with upper-level anomalies. Before the event, the cloudiness intensifies over the southern Arabian Peninsula, likely linked to deep convection that is associated with Indian summer monsoon anomalies (Fig. 4.12a). Therefore, the low-level thermal low over southern Iraq strengthens preceding the event. However, this pattern disappears during the event, with a notable absence of cloudiness over the Arabian Peninsula (Fig. 4.12b). Meanwhile, cloud cover intensifies over northern and northeastern India, likely associated with the southward shift of the Rossby wave to lower latitudes.

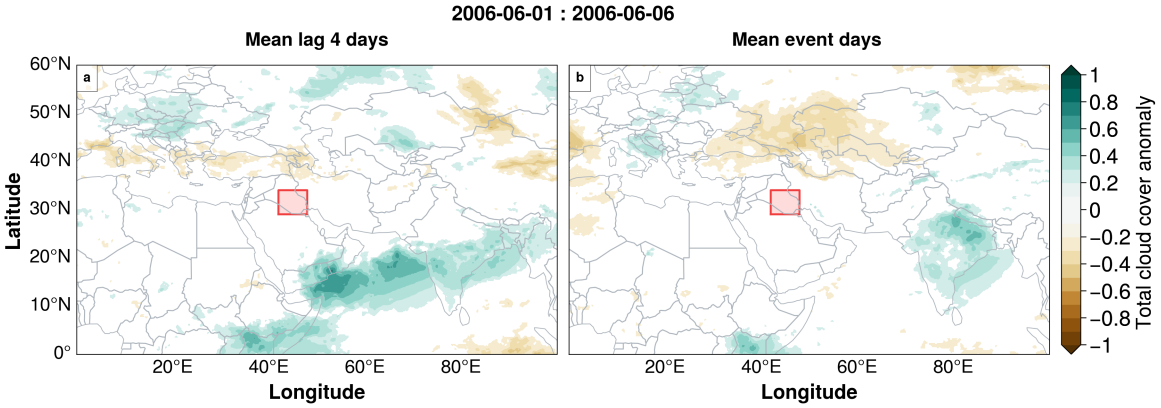

Figure 4.12: Evolution of total cloud cover anomalies. a) Averaged over 4 days preceding the onset of the event. b) Averaged over the event itself. The red box marks the heatwave area.

As discussed in Chapter 3, the attenuation of the prevailing Shamal winds, which are associated with friction-modified geostrophic flow emerging from the pressure gradient between dominant pressure systems, plays a key role in amplifying heatwave conditions. Figure 4.13b illustrates that the Shamal winds attenuate during the event, which coincides with the increase in Tmax (Fig. 4.13a). The Tmax anomalies, averaged over the target area, gradually rise in the week preceding the event and decline over the five days following the central day, returning to climatological levels. This attenuation extends to the mid troposphere levels corresponding with our results in Chapter 3. However, during the second event (June 17–23), weak positive anomalies ($\simeq$1 m/s) in the Shamal winds appear particularly in the lower troposphere (900–1000 hPa), at the onset of the event. This suggests that the Shamal wind had a small cooling effect, despite the positive anomalies. Nevertheless, the attenuation of the Shamal wind is still observed on the central day and at lag +1.

Interestingly, vertical advection ($-\omega\frac{\partial\theta}{\partial p}$) increases before both events (Fig. 4.13c), with warming by adiabatic compression of sinking air at approximately 4 K/day. This process coincides with the strengthening of the Shamal wind two days before the first event, and a similar pattern, though with stronger advection rates, is observed for the second event. This suggests that warmer air, likely from the mid to upper troposphere, is transported downward into the lower troposphere.

However, the Shamal wind analysis already accounts for aspects of horizontal advection $-(u\frac{\partial T}{\partial x}+v\frac{\partial T}{\partial y})$; examining vertical advection alone provides an incomplete picture of heatwave dynamics. Therefore, we further analyzed horizontal advection explicitly by investigating temperature advection terms at the 850 hPa level, where low-level processes are more pronounced.

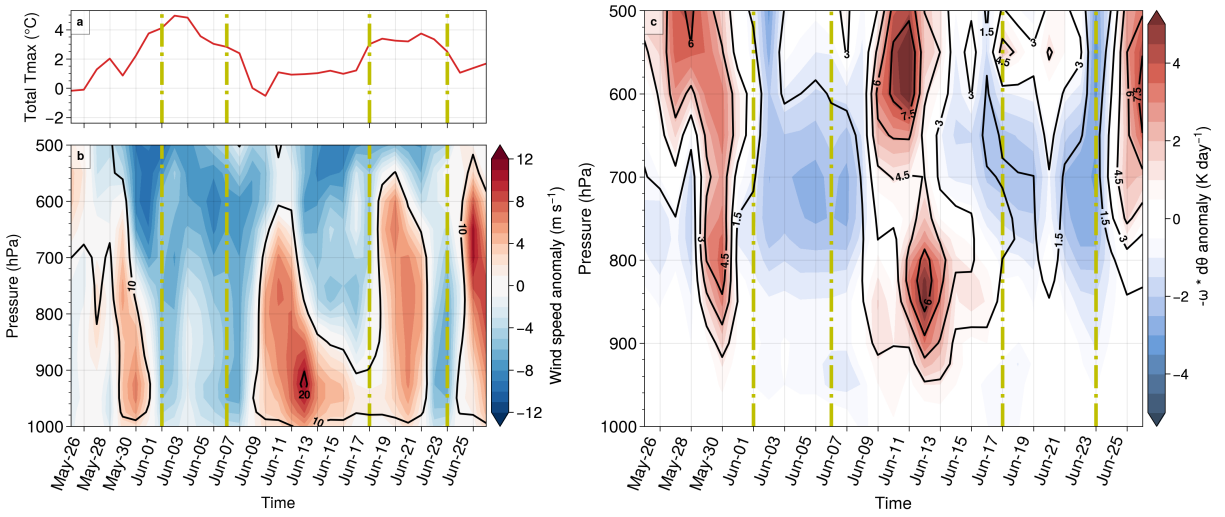

Figure 4.13: Different fields describing the heatwave case study with the central day on 02 June 2006. a) Evolution of Tmax anomalies (units: K) averaged over our target region. b) Cross-section of anomalous horizontal wind speed (full field as black contours) averaged along the blue line in (Fig. 4.14) that we defined in chapter 3. c) Similar to (b), however, of Vertical advection anomalies. vertical dash-dotted lines indicate the period of the heatwave.

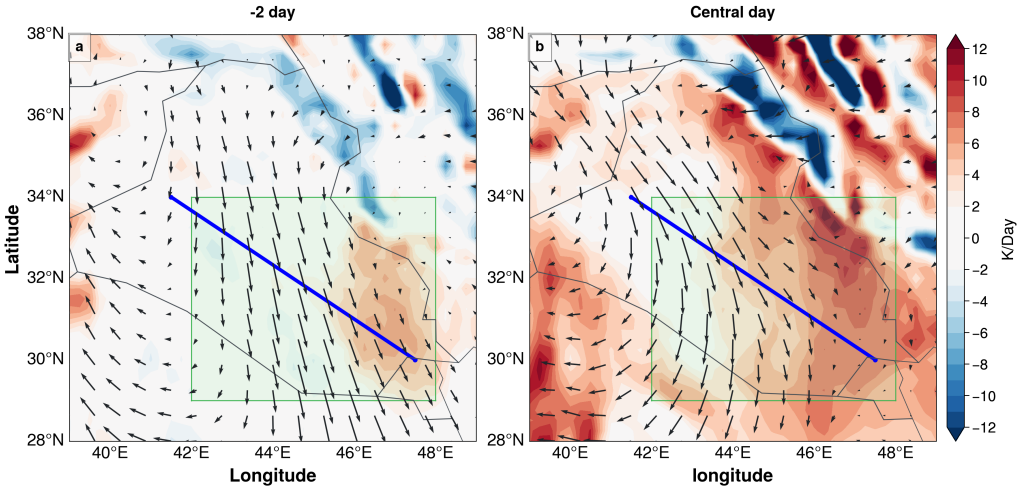

Figure 4.14: Horizontal temperature advection anomalies (shading) and total horizontal wind field (arrows) at 850 hPa. a) two days before the event, b) on the central day of the event. Blue line from 41°E/34°N to 48°E/30°N indicates the Shamal winds definition (see chapter 3) The green box indicates our target area.

Figure 4.14 shows the anomalies of this advection along with the total horizontal wind field direction. The positive advection anomalies appear weaker over southern Iraq at day -2 before the event in comparison with the central day of the event, coinciding with a

strengthened Shamal wind on the same day (Fig. 4.14a). However, the advection intensifies as it aligns with the Zagros Mountains, expanding toward our target area on the central day of the event (Fig. 4.14b). This is associated with a likely deviation in wind direction over southern Iraq, particularly in our target area, due to the blocking effect of the mountains. Furthermore, the arrows show the potential presence of a gentle downsloping wind on the leeward side of the Zagros Mountains, even ERA5 has limitations (horizontal resolution $\simeq$30 km) of the mesoscale features, such as gap winds. We will discuss these results more in the next discussion.

4.5.2 Discussion

This event (June 2, 2006) is classified as an RW event, with large-scale Rossby waves acting as the primary physical driver. Observational data captured this event in most stations located on the leeward side of the Zagros Mountains and in the northern part of our target area. To further analyze the mechanisms behind this event, we examined the ERA5 reanalysis data.

Studying this single event provides valuable insight into questions raised by the composite-mean analysis of the RW cluster. This case study supports our earlier findings that synoptic-scale modifications significantly contribute to heatwave evolution. Specifically, Rossby wave activity plays a crucial role in altering lower-level atmospheric conditions. Furthermore, the potential interaction between the upper-level anticyclonic Indian summer monsoon and large-scale circulation patterns further impacts regional dynamics.

Modification in Local Dynamical Enhancing Heatwave Conditions

Consistent with the composite analysis of RW events, the attenuation of the Shamal wind appears to be a key factor in heatwave intensification. In the days leading up to the event, vertical advection strengthens down to 900 hPa, indicating that warmer air from the mid-to-upper troposphere is being transported downward. This process is temporarily coupled with a strengthening of the Shamal wind a few days before the heatwave. Although the Shamal wind transports relatively cooler air from higher latitudes and thus exerts a surface cooling influence, its associated turbulence enhances vertical mixing within the boundary layer. This boundary-layer mixing suppresses the surface warming that would otherwise result from vertical advection (cf. Fig. 3.1b,c). When the Shamal wind weakens, however, vertical advection becomes more effective, contributing to the development of a warm layer over our target area—a pattern observed in both events.

During the heatwave, the Shamal wind tends to weaken due to a reduction in the pressure gradient. Given the complex topography of our target area, the residual gentle flow,

resulting from the north-to-south sliding air mass over Iraq, is likely deflected by the blocking effect of the Zagros Mountains. Consequently, this flow becomes less intense than the down-slope winds on the leeward side of the Zagros Mountains. As a result, horizontal advection appears to extend from the leeward side of the Zagros Mountains to our target area, which has lower terrain compared to the surrounding region. This reduction in cold-air advection over the target area limits effective ventilation, allowing warm air to become trapped in the lower terrain. As a result, heat accumulates near the surface, amplifying the intensity of the heatwaves. Even though this pattern is considered mesoscale and occurs on a short timescale, its evolution is driven by the development of the upper-level general circulation and Rossby wave propagation.

Rossby wave and the waveguide acting

Generally, the vertical advection, which appears to intensify coinciding with the strengthening Shamal winds (Fig. 4.13c), is associated with subsidence from a dominant high-pressure system in the mid-troposphere over the Zagros Mountains. This subsiding further enhances the local anticyclonic circulation over the northern Arabian Peninsula and the eastern Mediterranean (Zaitchik et al., 2007). While the low-level thermal low extends across southern Iraq to the Gulf, strengthened by irradiation and deep convection of the upper-level anticyclonic circulation of the Indian monsoon. These pressure systems, which reinforce the strength of the Shamal wind, are influenced by Rossby wave propagation.

In the preceding days (26-30 May) of the event, the North Atlantic jet acted as a waveguide for the Rossby wave propagation, facilitating its propagation across the mid-latitudes. However, during the event, it shifts to the south, increasing the likelihood of approaching or merging with the African-Asian jet, which often spans across a wide region in summertime. This interaction enhances the propagation of the Rossby wave toward lower latitudes, particularly over the Middle East and North Africa MENA region. As a diagnostic of the waveguide, figure 4.15 shows the meridional gradient of PV at 350K relative to latitude. It suggests that the jets tend to converge or merge over the northern Mediterranean and southern Europe one day before the event.

In this wave pattern, the anticyclonic system embedded within the Rossby wave intensifies and expands across a broader range of latitudes. This upper-level anticyclonic anomaly enhances subsidence over elevated terrains, deepening and extending into the lower troposphere.

However, an additional factor influencing the weakening of this thermal low is its association with the upper-level anticyclonic system of the Indian Summer Monsoon. Meanwhile, as Rossby waves propagate toward lower latitudes, their phase structure facilitates the development of a cyclonic system over the Iranian Plateau (Fig. 4.10b). This cyclonic system probably weakens the monsoon westerly flow, reduces moisture transport, and lim-

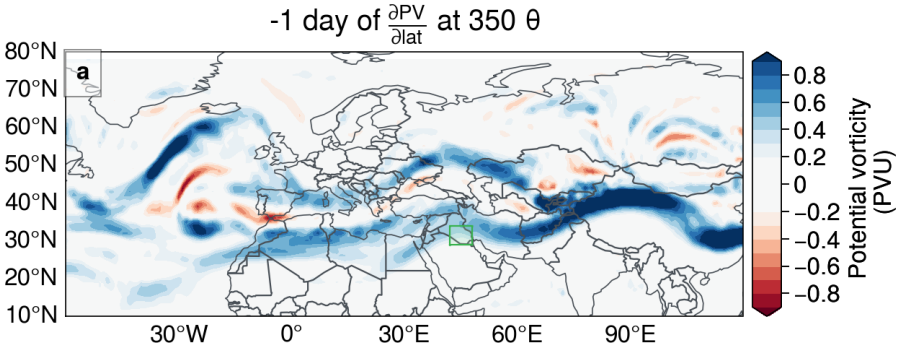

Figure 4.15: Meridional gradient potential vorticity relative to latitude of one day before the event (1 PVU: K kg^{-1} m^2 s^{-1}). The green box indicates our target area.

its surface irradiation, ultimately leading to a weakening of the low-level thermal low over the Gulf. This configuration is consistent with the observed reduction or eastward shift in total cloud cover, indicating suppressed or displaced convective activity (Fig. 4.12b). This weakening serves to attenuate the Shamal winds, which in turn modify the surface temperatures.

4.5.3 Predictability of the selected Heatwave Event

To evaluate the forecast performance, we use the 2006 hindcast year, which corresponds to the 2022 real-time forecasts, to define the **Truth** for each variable in our analysis. This dataset was prioritized because it allows initialization on the exact central day of the heatwave, an advantage not available with the 2021 dataset, despite both being based on the same IFS model. This selection ensures a more precise representation of the accuracy of the forecast (for further details, see 4.2).

Figure 4.9 illustrates the S2S Tmax anomalies over two weeks. The S2S forecast model shows strong skill in capturing extreme Tmax anomalies over the target region and its surroundings during the first week. At lag -3, 91% of ensemble members successfully predicted the event, decreasing slightly to 82% at lag -6. However, predictability deteriorates during the second week, with the forecast success rate dropping to 23% at lag -9 and 18% at lag -13 (Fig. 4.16a–d).

Despite this decline, the forecasts still capture the general anomaly pattern in the second week, though with an eastward shift, particularly toward the Zagros Mountains, suggesting a shift in heatwave-driving mechanisms in this region (Fig. 4.9a and b). In contrast, the ensemble forecasts at lags -6 and -3 exhibit patterns closely similar to the ERA5 reanalysis (cf. Fig. 4.9b).

For ensemble members who fail to capture the event, the second week features cooler anomalies than observed. Furthermore, during the first week, the anomalies intensify in the center of Iraq with a notable tendency toward cooler conditions at lag -6 (Fig. 4.16e-h).

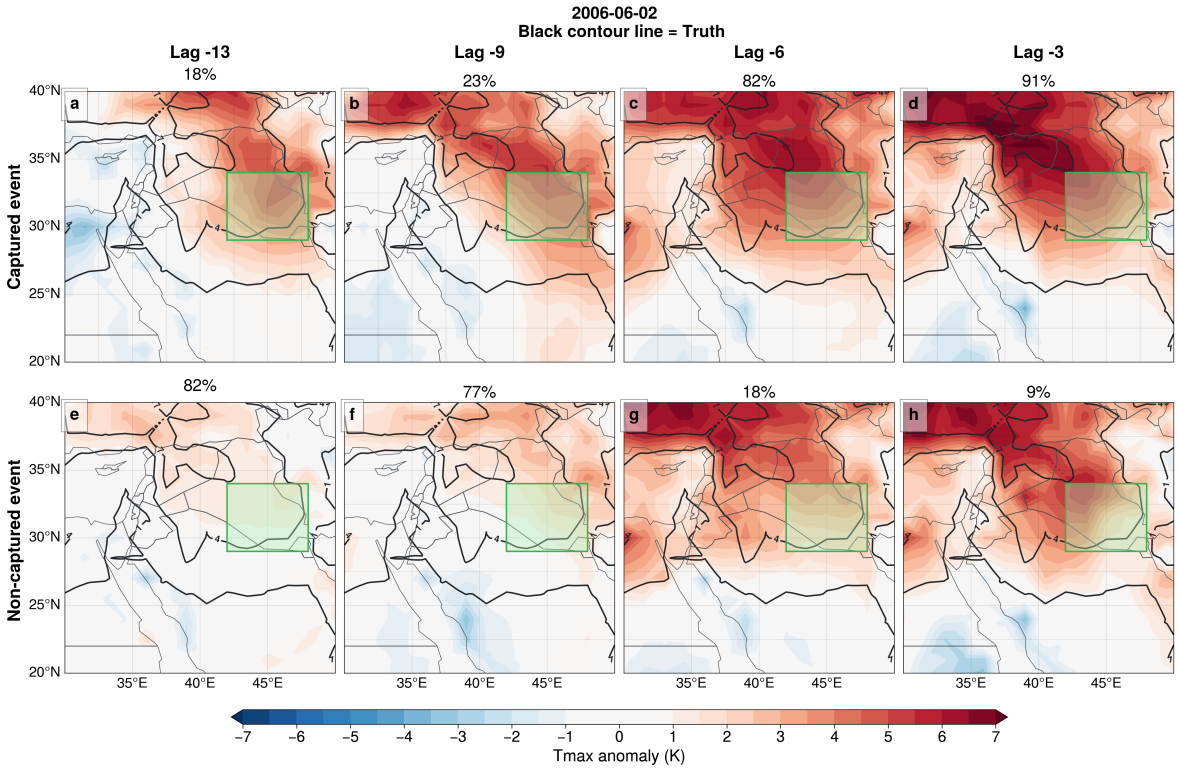

Figure 4.16: Tmax anomaly (K) of S2S data for June 2, 2006, **a-d** indicate ensemble members that captured event, **e-h** indicate ensemble members that do not capture the heatwave event at different lead times (lags -13, -9, -6, -3). The black contour lines represent the observed indicate **Truth** of the anomalies. The green box indicates our target area. Percentages above each panel indicate the proportion of ensemble members predicting the event.

To understand the dynamical factors influencing forecasts, we examine upper-level circulation patterns using geopotential height anomalies at 200 hPa (Fig. 4.17). The captured and non-captured ensembles exhibit distinct configurations, with notable asymmetries emerging during the second week (Fig. 4.17a, b, e and f). During this period, the ensemble forecasts show weaker anomalies, indicating a decline in forecasts. However, the captured ensembles maintain a more coherent large-scale structure, with a slight northward displacement of the pressure systems relative to the **Truth** (cf. Fig. 4.17a and b).

In contrast, during the first week, all ensemble members—whether they captured the event or not—exhibit a high degree of similarity with the ERA5 reanalysis. The upper-level geopotential height anomalies align with the Rossby wave pattern, indicating that the

forecasts effectively capture large-scale circulation at shorter forecast (cf. Fig. 4.17c,d, and g,h).

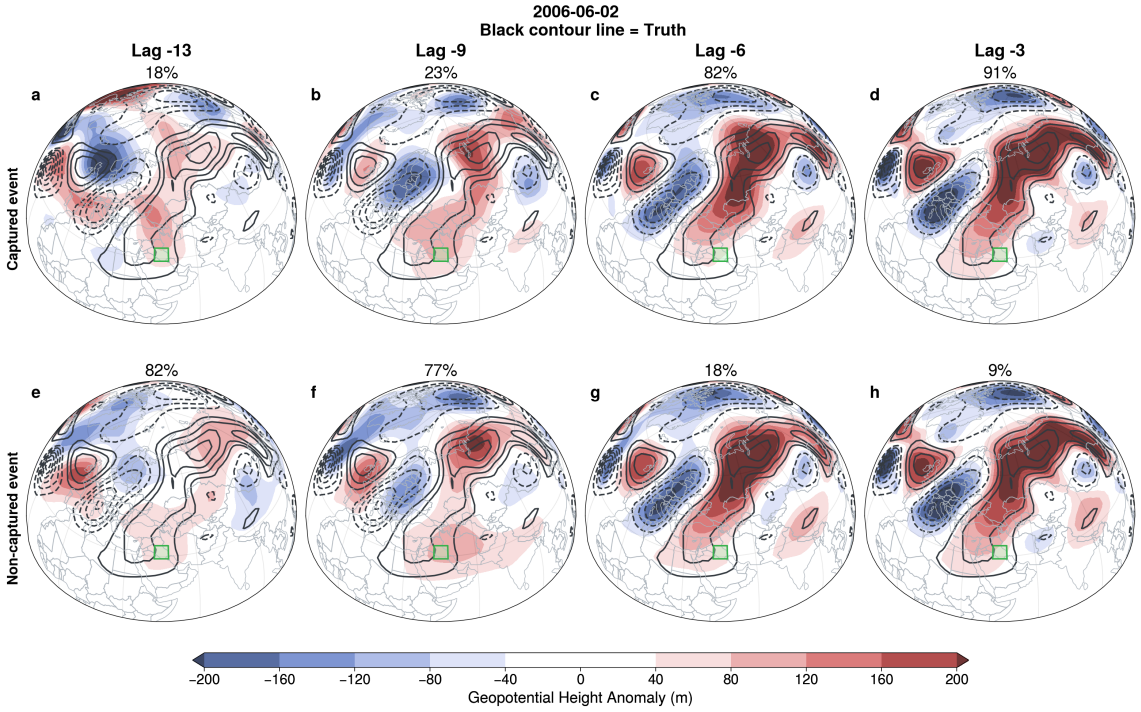

Figure 4.17: Similar to 4.16 however of geopatantial height anomalies (m).

Figure 4.18 shows S2S meridional wind anomalies at 200 hPa. The anomaly configurations closely correspond with the geopotential height patterns (Fig. 4.17), reinforcing the relationship between upper-level wave activity and heatwave evolution in ensemble members' forecasts.

During the first week, both captured and non-captured ensembles exhibit a well-defined Rossby wave structure, particularly at lags -6 and -3 (Fig. 4.18c, d, g and h). This consistency underscores the model's strong predictive skill at shorter forecasts, where the wave structure remains coherent and closely aligned with the **Truth**. The symmetry in the meridional wind anomalies further supports the notion that ensemble forecasts effectively resolve upper-level wave dynamics, which play a crucial role in capturing extreme heat events.

However, as the forecast extends longer, the forecast deteriorates. By lag -9, the ensembles exhibit a northward displacement of anomalies, accompanied by a weakening over the mid-latitudes (Fig. 4.18b). This shift likely reflects a gradual loss of coherence in the wave structure, reducing forecast accuracy.

In the far-extended range (lag -13), the anomalies become diffuse and significantly weaker

compared to the **Truth** (cf. Fig. 4.18a and e). The diminished wave signal suggests that beyond two weeks, the model struggles to maintain large-scale circulation features, reflecting the intrinsic predictability limit of the troposphere and leading to increased forecast uncertainty. This highlights a fundamental limitation in extended-range forecasting, where the Rossby wave diminishes as the lead time increases.

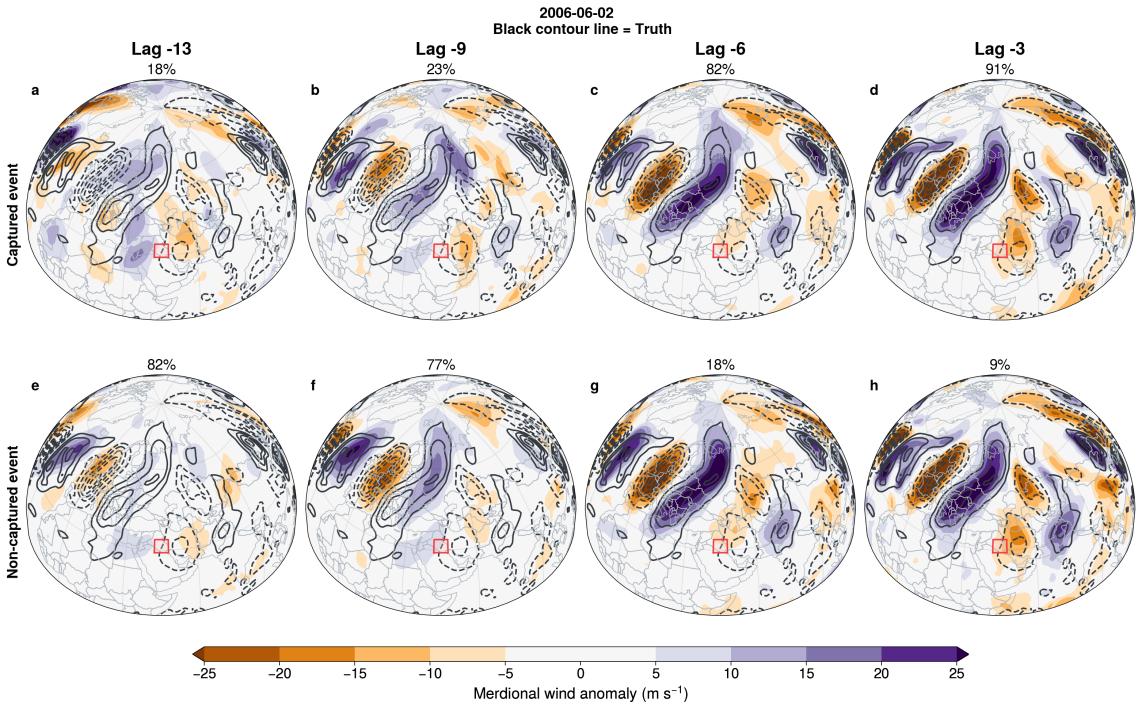

Figure 4.18: Similar to 4.16 however of merdional wind speed anomalies (m/sec).

In the lower atmosphere, the S2S model demonstrates skill in capturing the reduction of the low-level thermal low, which is associated with Shamal wind attenuation (Fig. 4.19). During the lag period from -9 to -3 days, the forecast ensemble that captured the event successfully represents the weakening of the thermal low in alignment with the **Truth**. However, at lag -13, positive anomalies shift toward our target area, suggesting an alternative heatwave mechanism that does not involve a reduction in the thermal low.

In contrast, the ensemble members failed to capture the event, still showed a similar pattern at lag -3, resembling those that successfully forecast the heatwave (Fig. 4.19). While the model does indicate a weakening of the thermal low at lag -6, it also suggests an anomalous northward extension of the lower-level monsoon flow over India. This tends to be consistent with an expansion of upper-level subtropical positive geopotential height anomalies (cf. Fig. 4.17g). This consistency becomes more pronounced at lag -7, as the upper-level subtropical high extends over the Arabian Peninsula. This extension could be associated with an overestimation of deep convection and an exaggerated intensification of the thermal low (cf. Figures 4.17f and 4.19f).

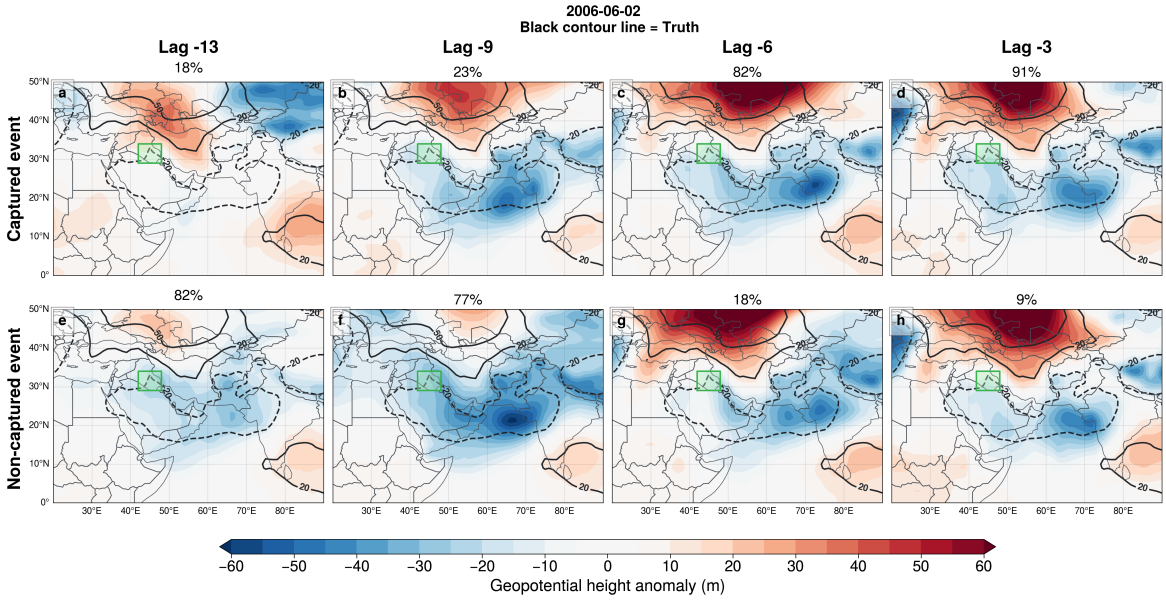

Figure 4.19: Similar to 4.16, however, of geopotential height anomalies at 850 hPa (m).

Unfortunately, we did not present the Shamal wind index as a function of pressure levels (as ERA5 reanalysis data) due to the high computational demands of data processing. However, in Figure 4.20, we approximate this diagnostic by calculating mean wind speed anomalies over the lower troposphere (850,925, and 1000 hPa).

Despite this limitation, the model demonstrates skills only at lag -3 of both captured and non-captured ensembles. However, in longer forecasts (lag -13 and -9), the ensembles that captured the events show a southward shift of wind anomalies over the Gulf, likely due to increasing model uncertainty. For non-captured ensemble forecasts, the model shows strengthening of the Shamal wind at lag -6 (Fig. 4.20g).

4.5.4 Discussion

The spatial distribution of the ensemble members that successfully capture the event reveals that the S2S model demonstrates the skills to closely resemble the reanalysis data in 2 weeks in advance of the forecast. However, the model tends to amplify the Tmax anomalies on the leeward side of the Zagros Mountains, particularly during the second week of the forecast. This bias likely arises from increasing model uncertainty at longer forecasts, primarily due to the intrinsic limit of atmospheric predictability, with additional contributions from limitations in representing mesoscale processes. This limitation appears lag –6 and longer forecasts across all ensembles, where the model misrepresents Shamal wind attenuation (Fig. 4.20). This suggests that while the model represents mesoscale processes well at shorter forecasts, its skill drops at longer forecasts, performing less effectively than

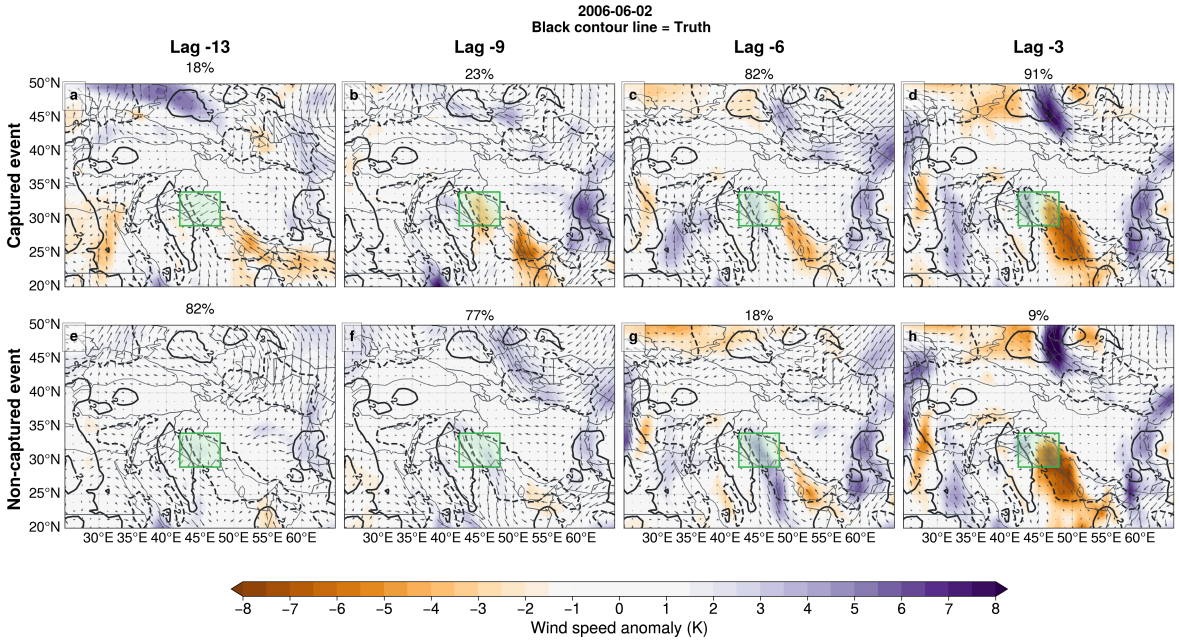

Figure 4.20: Horizontal Wind speed anomalies averaged over 850–1000 hPa levels (Shading). The arrow indicates Horizontal wind direction anomaly. **a-d** indicate ensemble members that captured event, **e-h** indicate ensemble members that non-captured heatwave events at different lead times (lags -13, -9, -6, -3). The black contour lines represent the observed indicate **Truth** of the anomalies. The green box indicates our target area. Percentages above each panel indicate the proportion of ensemble members predicting the event.

for larger-scale features such as Rossby waves. Indeed, the model likely tends to overemphasize the influence of the Indian Summer Monsoon at lower levels as a response to the uncertainty of the position of the wave and subtropical height. This uncertainty might prompt the model to be exaggerated, particularly in deep convection, moisture transport, and cloudiness (i.e., cooling SST). This leads to an intensified thermal low over the Gulf (as seen at lag -9 in the Non-captured ensemble events in Figure 4.19f), affecting the pressure gradient and increasing uncertainty in the evolution of the Shamal wind.

Furthermore, increasing uncertainty in large-scale circulation is a common limitation in extended-range forecasting. This uncertainty emerges as a key source of model error, allowing other physical drivers to modify surface temperature and influence heatwave development. For instance, the strengthening of geopotential height anomalies over high terrain enhances adiabatic warming, reinforcing anticyclonic conditions that, in turn, maximize surface temperature. Overall, while the S2S model exhibits performance skill in capturing Rossby wave dynamics in the first week, its skills in the second week are probably affected by systematic shifts in key features. These biases highlight the challenges in distinguishing true physical signals from model-induced uncertainties in extended-range forecasts.

Chapter 5

UNSEEN Heatwave Events: Discovering Hidden Mechanisms of Heatwaves via Unseen S2S Events Utilizing Ensemble Abundance

A significant limitation in analyzing ERA5-based heatwave events is the statistical constraints associated with rare events. First, the heatwave definition used in Chapter 3 resulted in one dominant cluster characterized by a distinct physical mechanism (i.e., Rossby Wave events), while the remaining events formed a more ambiguous cluster in terms of their physical mechanisms. Second, the hindcast S2S forecast data do not cover the period that was selected for ERA5-based heatwave identification; for example, only six events from the Non-Rossby Wave (Non-RW) cluster were identified in this dataset. This presents a challenge in understanding the underlying mechanisms and implications for the predictability of such events.

Overcoming these limitations often requires expanding the events through simulations, typically conducted using idealized climate models. However, we adopt an alternative approach in this thesis by utilizing the **UNprecedented Simulated Extremes using ENsembles (UNSEEN)** method. The UNSEEN approach utilizes forecast ensemble members to compute more reliable statistics for heatwave events. It relies on the ensemble forecasts' characterizations that provide a large number of physical atmospheric scenarios under similar boundary conditions, which do not exist in the reanalysis data (i.e., ERA5-Based events). Ultimately, it increases the effective sample size, allowing more robust estimation of the frequency, intensity, and variability of heatwave events driven by different physical mechanisms. This method, demonstrated by Thompson et al. (2017), has proven effective in earlier research by using large ensembles of high-resolution initialized climate

simulations to model extreme events such as severe floods triggered by rare, intense rainfall. In the context of this study, the UNSEEN method provides a valuable tool for improving the understanding and predictability of heatwave events, offering insights that traditional reanalysis and datasets cannot provide.

5.0.1 Trend sensitivity

In Chapter (4), we removed the seasonal cycle from the date. However, these datasets likely still exhibit significant climatic variability due to the existence of underlying trends. Although this variability may seem less important given that we have event data, it is crucial for the construction of heatwave identification, as it greatly influences the count of identified events. To examine the influence of trends on the data and how they affect the threshold selection (i.e., the 90% percentile), we compared different preprocessing approaches. Specifically, we tested the effects of removing the linear trend alone, deseasonalizing alone, and applying both methods in different orders (i.e., trend removal followed by deseasonalization, and vice versa). This approach allows us to evaluate how each method—or their combination—impacts the resulting distribution and the robustness of the threshold. Ultimately, it helps identify the most appropriate strategy for handling the data prior to detecting extreme events. The detrending process (removing linear trend) employed the hindcast data from previous years, which was performed for each lead time on a day-of-the-year basis. For instance, if the lead time corresponds to June 1 of the reference time initialized in 2022, the trend is calculated using all June 1 data from the preceding 20 years of hindcast.

Figure 5.1 shows the comparison of the 90% percentile of each data processing approach across all hindcast years. The thresholds reveal a trend in the data, particularly in the deseasonalization-only case, which shows a pronounced warm tendency. This tendency likely increases the number of detected events in hindcast years close to the real-time period. In contrast, the other preprocessing approaches appear broadly consistent across the years, regardless of the order in which the detrending and deseasonalization are applied. Based on these results, we proceed with the dataset from which only the linear trend was removed.

5.1 UNSEEN Heatwave identification

Similar to our methodology for identifying heatwaves in reanalysis data, adjustments were necessary to accommodate the structure of the S2S forecast data and to minimize the influence of trend and seasonality. The steps are as follows:

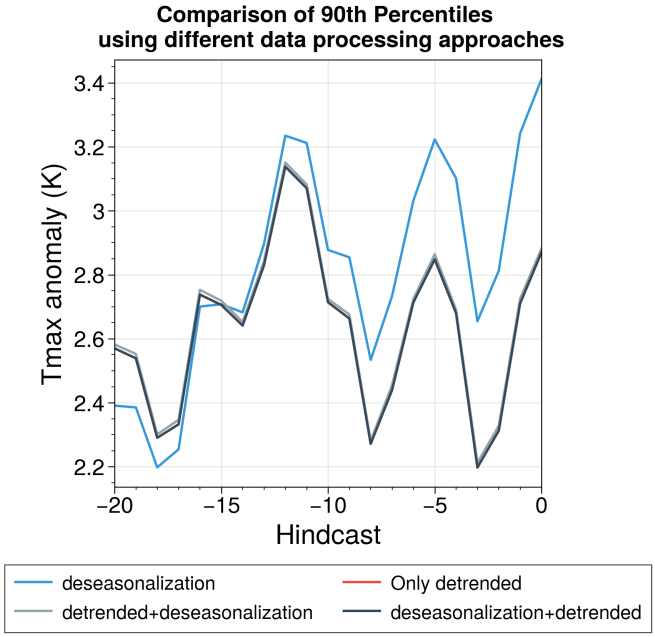

Figure 5.1: Comparison of the 90th percentile of Tmax across hindcast years under various preprocessing approaches: (1) linear trend removal only, (2) deseasonalization only, and (3) both methods applied in different sequences.

1. **Data Selection:** We selected the initialization of the S2S forecast data for the years 2021 and 2022 with 20 years of hindcast. Using data from these years ensures consistency, as the forecasts were generated using the same model cycle, reducing potential biases introduced by variations across different model configurations.

2. **Spatial Averaging:** A spatial mean was calculated for our target area (box), and heatwave identification was based on this averaged value. This approach differs from the methodology outlined in the Chapter (2), where we used individual grid points. This different approach (i.e., spatial means) was necessary to manage the computational expense and complexity associated with loading large datasets. However, this technique may introduce a degree of uncertainty, particularly in regions characterized by strong spatial variability due to topographic complexity, such as in Iraq (e.g., the Zagros Mountains). With these local conditions, spatial means can smooth out extreme values, potentially under-representing localized heatwave intensities or losing the characterization of the timing and duration of events.

3. **Lead Time Selection:** To minimize the effects of initialization memory and ensure that detected events are as independent as possible, heatwave events were identified within the 14–46 day lead time window. This selection is based on the assumption that, at this window, atmospheric variability in ensemble forecasts reflects the model's internal dynamics and physics rather than the influence of initial conditions.

4. **Threshold identification:** Consistent with Section(2.2), we selected the 90% percentile as the threshold to define the UNSEEN events. However, as shown in Figure(5.1), the percentile values fluctuate across the real-time and hindcast years. To account for these variations, a year-specific threshold was applied. This method enhances the consistency and reliability of UNSEEN events selection across different years.

5. **Event Definition:** Consistent with the earlier methodology, heatwave events were identified as periods where the maximum temperature anomaly (Tmax) exceeded a specific threshold for at least three consecutive days.

Figure 5.2 illustrates the temporal distribution of the UNSEEN events across both real-time and hindcast years. Except for an isolated spike in hindcast year -11 at lead time 14, and in the real-time data at lead time 19, the UNSEEN events appear to be well distributed across all years and lead times. This consistent spread suggests the absence of a residual trend effect, which supports the robustness of using the 90th percentile threshold computed separately for each hindcast year.

Interestingly, no events are identified at lead time 38 across all years. More broadly, there is a decreasing trend in the number of detected events at longer lead times. This suggests that the model tends to predict cooler conditions relative to the event threshold as lead time increases, which may reflect a systematic bias or forecast drift, and highlights the reduced skill of the model at extended lead times.

5.2 UNSEEN events-overall evolution

The evolution of Tmax anomalies over 17 days (from lag -6 to +10 days) reveals an anomaly of $\approx$4 K on the central day (Fig.5.3a, red line). Anomalies increase leading up to the central day, corresponding with a growing number of ensemble members and reduced spread. After the central day, the anomalies gradually decline, consistent with a reduction in the number of ensemble members and an increase in their spread (see blue line and violin plots for positive lag days in Fig.5.3a, blue line). This prolonged evolution of anomalies may be linked to upper-level general circulation features such as atmospheric blocking or Rossby wave trains. Additionally, the S2S module itself could be a potential source of the sustained positive anomaly. In other words, the ensemble forecasts may retain signals from slowly evolving sources of predictability, such as the Madden–Julian Oscillation (MJO), El Niño–Southern Oscillation (ENSO)-related SST anomalies, or land surface conditions. These memory-driven components are known to influence atmospheric variability on sub-seasonal timescales and can contribute to coherent warm anomalies well over long periods. Since the detrending relies on only 20 years of hindcast data, it may not completely remove the influence of such persistent signals.

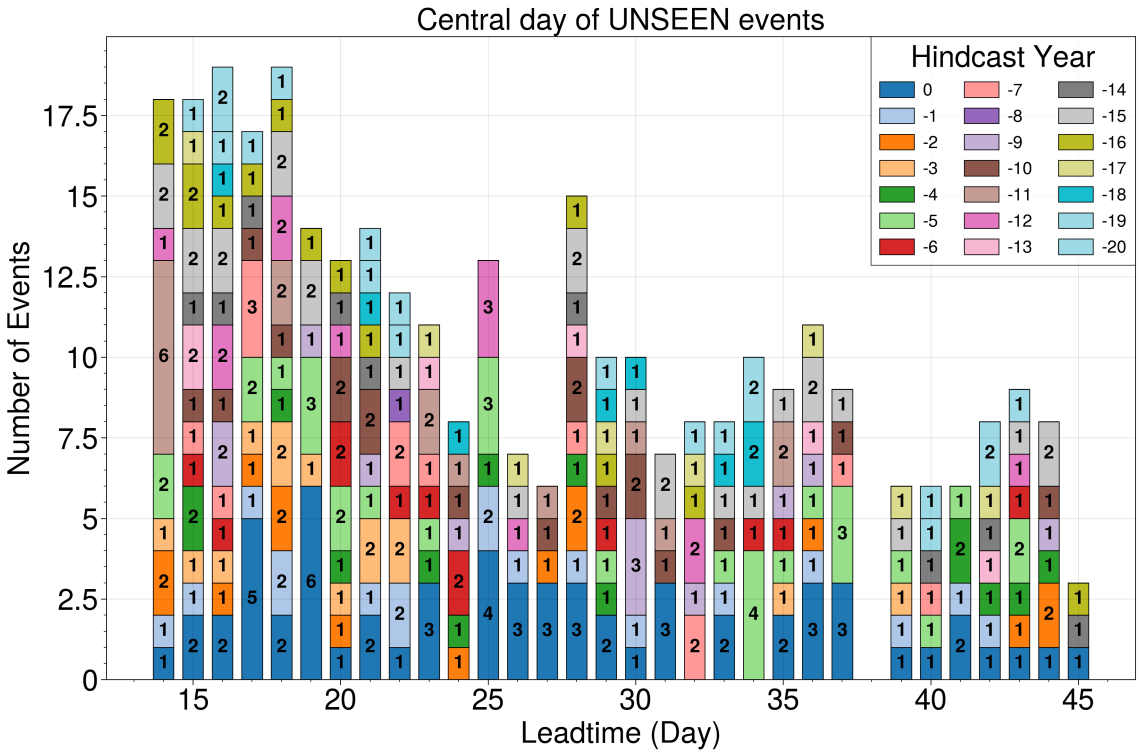

Figure 5.2: Frequency of UNSEEN events over both real-time and hindcast over all lead-time. The threshold was 90% percentile of each year's forecast.

Figure (5.3b) shows the anomalies intensifying over Iraq compared to the surrounding regions. The anomalies appear to be constrained by the Zagros Mountains, acting as a boundary to the east, and thus tend to extend westward. Further, the box plot (Fig. 5.3c) shows that the late-season events are characterized by lower severity (i.e., August) compared to those in the early season (June). Indeed, the evolution of Tmax anomalies coincides with that of the upper-level circulation, and we will attempt to describe their synchronization.

Figure 5.4 shows the composite mean of upper-level geopotential height anomalies (200 hPa) for the UNSEEN events. At lag -5 (Fig. 5.4a), a pronounced anticyclonic anomaly emerges over the target region, extending northward and stretching into central Eurasia with a slight eastward tilt. This anomaly appears embedded within a Rossby wave train, evident from the alternating positive and negative anomalies across Eurasia. The associated subtropical jet is intensified over the Indian monsoon region, suggesting a possible interaction between the Rossby wave train and the upper-level monsoon circulation. Arrow vectors highlight the large-scale anticyclonic flow, which may partly reflect the northwestern flank of the monsoon anticyclone (Fig. 5.4a). This intersection coincides with the pronounced easterly flow (total field) over the southern Arabian Peninsula, suggesting a potential tropical–extratropical coupling likely linked to enhanced monsoon convection. In

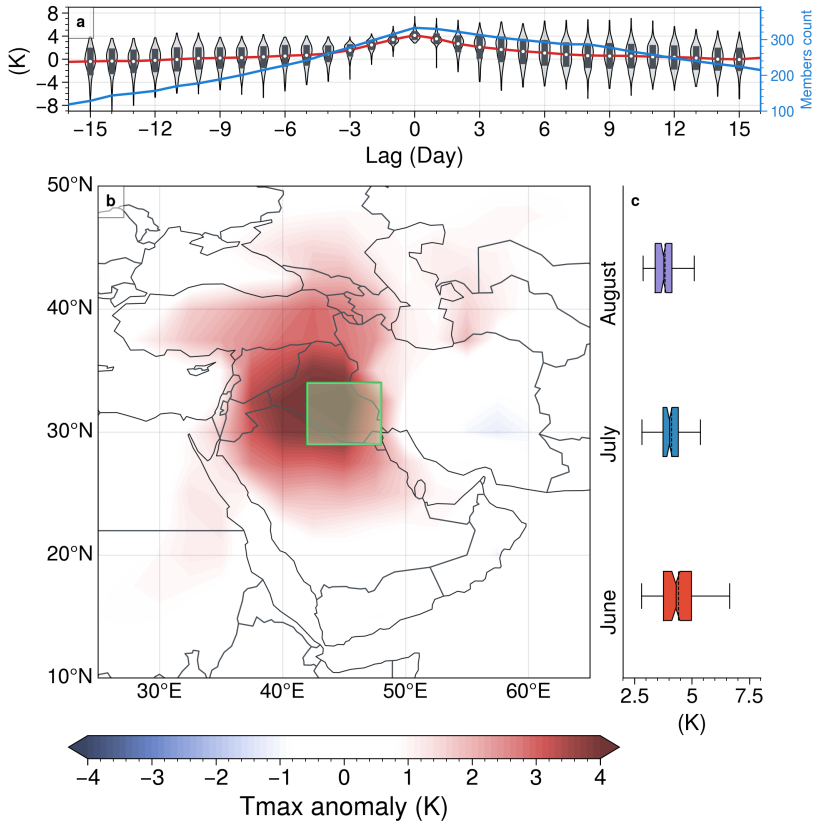

Figure 5.3: (a) Composite-mean evolution of Tmax anomalies averaged over the heatwave area. The blue line indicates the number of ensemble members that are identified by UNSEEN approach, with the corresponding distribution shown by the violin plot. (b) Composite-mean of Tmax anomalies of lag 0. (c) The box plots represent the distribution of Tmax anomalies (K) averaged over our heatwave area for each summer month (June, July, and August) individually. The green box indicates our heatwave area.

lag 0, this easterly flow becomes more pronounced, while the anticyclonic anomaly intensifies to the north and becomes confined between 30–55°N, extending slightly westward into the eastern Mediterranean. Simultaneously, a dipole pattern emerges, with cyclonic anomalies over central Europe and an intensified ridge over northern Iraq, indicating a possible Rossby wave breaking event (Fig. 5.4b). This dipole structure is commonly associated with a reshaped upper-level jet, which can facilitate the westward extension or long-lasting anticyclonic anomalies. This upper-level jet also extends toward East Asia, contributing to favorable conditions for cyclonic development over far eastern Asia (Fig. 5.4b). Moreover, the anticyclonic anomalies remain stationary over the 10-day period, consistent with the persistence of positive Tmax anomalies for more than two weeks (5.3a). This persistence likely reflects the retained memory of key sources of predictability within the S2S model. These sources could modulate the evolution of planetary-scale Rossby wave trains and promote persistent anticyclonic ridging patterns over the Middle East. Figure

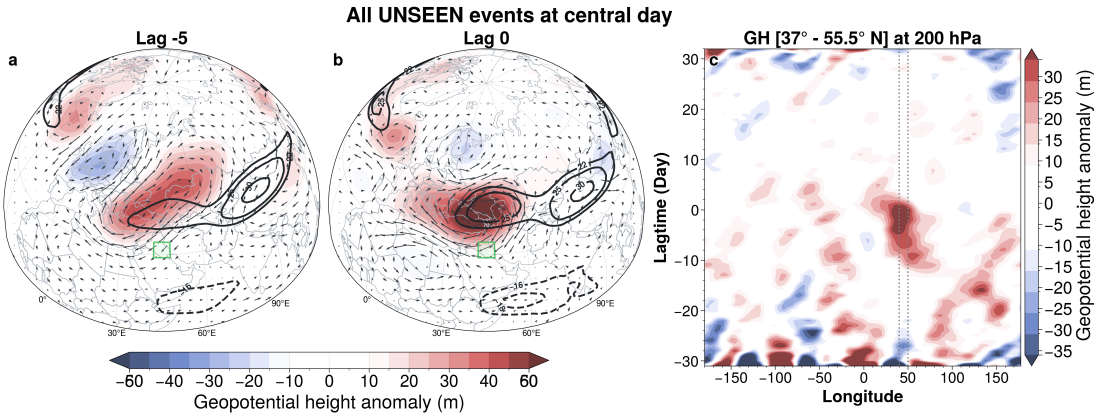

Figure 5.4: Composite-mean evolution of geopotential height anomalies (shading), horizontal wind anomalies (arrows), and total Zonal Wind (contours, units: m/sec) at 200 hPa. **a** and **b** lags -5 and 0 of UNSEEN events, respectively. **c** Hovmöller plot geopotential height anomalies averaged over latitude 37°-55.5°N. The area between the dotted lines in (c) indicates Iraq, and the green box marks the heatwave area.

5.4c shows a stationary pattern of anticyclonic anomalies that persists for more than two weeks, with a tendency to strengthen as the central day approaches.

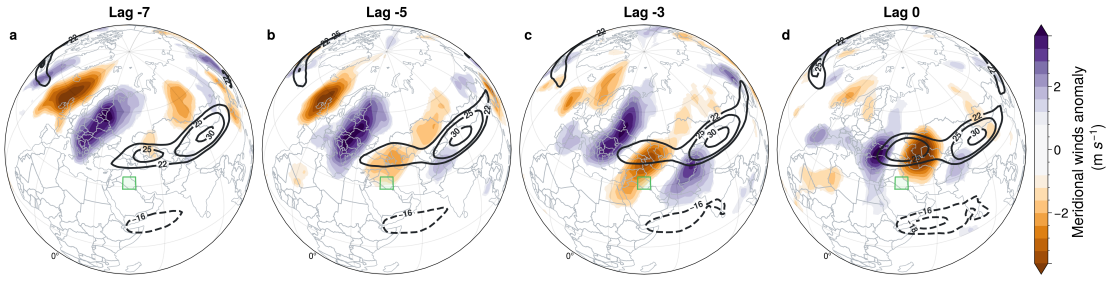

Figure 5.5: Composite-mean evolution of meridional Wind anomalies (shading) and total Zonal Wind (contours, units: m/sec) at 200 hPa. The green box marks the heatwave area.

These upper-level pressure anomalies are embedded within a Rossby wave train propagating through mid-latitudes, characterized by fluctuating meridional wind structures spanning (35-65°N) during lags -7 to -5 (Fig. 5.5a and b). From lag -3 to lag 0, the wave pattern shifts equatorward, guided by the subtropical jet (Fig. 5.5c and d). At lag 0, meridional wind anomalies intensify over Iraq, suggesting the Iraq–Arabian Peninsula region becomes the target of a downstream ridge embedded within the Rossby wave packet (Fig. 5.5d). Additionally, the wave pattern becomes more latitudinally confined between 25–40°N, consistent with anticyclonic Rossby wave breaking during the core of the heatwave events.

Figure 5.6 illustrates the evolution of geopotential height anomalies at two levels, with shading representing the lower troposphere (700 hPa) and contours showing the upper

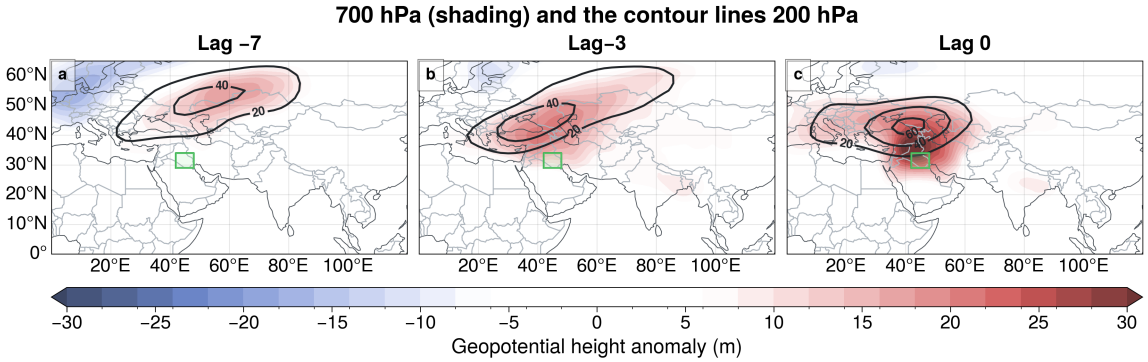

Figure 5.6: Composite-mean evolution of geopotential height anomalies at 700 hPa (shading) and at 200 hPa (contours). The green box marks the heatwave area.

troposphere (200 hPa). At lag –7, a broad upper-level ridge (contours) extends eastward across the Mediterranean into Eurasia, while weaker lower-level anomalies appear further north toward higher latitudes (Fig. 5.6a). At lag –3, the anomalies structure develops to be more coherent, with the 700 hPa anticyclone intensifying over Iraq while the 200 hPa ridge shifts poleward, creating a vertically tilted configuration (Fig. 5.6b). This vertical tilt—where the upper-level ridge is displaced northward relative to the lower-level anticyclone—reflects an enhanced baroclinic structure and suggests dynamical coupling between the two levels. At lag 0, the lower-level anticyclone becomes more confined over Iraq, while the 200 hPa anomaly intensifies further north, exhibiting the tilted meridional structure (Fig. 5.6c).

This vertical tilt is consistent with Rossby wave evolution and provides favorable conditions for heatwave amplification. The upper-level ridge promotes subsidence and suppresses vertical mixing, while the lower-level anticyclone reinforces near-surface warming under persistent high pressure. Moreover, the interaction of this structure with the Zagros Mountains likely enhances mesoscale processes, including localized subsidence on the leeward side, reduced cloud formation, and stable boundary-layer development—all of which contribute to the intensification of heatwaves over Iraq.

5.3 UNSEEN Events Classification

5.3.1 Thermal Low and Shamal Wind Relationships with Tmax

As in previous results, this configuration leads to a modification of the dominant pressure system patterns over the region during the summer season. Specifically, the low-level thermal low, which is typically linked with the Shamal wind mechanism, was modified in

response to the evolution of Rossby waves at upper levels. To investigate this further, we create a Thermal Low Index (TLI) to examine its correlation with Tmax anomalies. It was derived by averaging geopotential height anomalies at 850 hPa over a selected area extending 27°–32°N and 48°–54°E, an area notably influenced by geopotential height anomalies over Iran (Fig. 5.7). This area selection was based on earlier findings related to the Shamal wind mechanism (Fig. 3.16). Then, the result was standardized before computing the correlation.

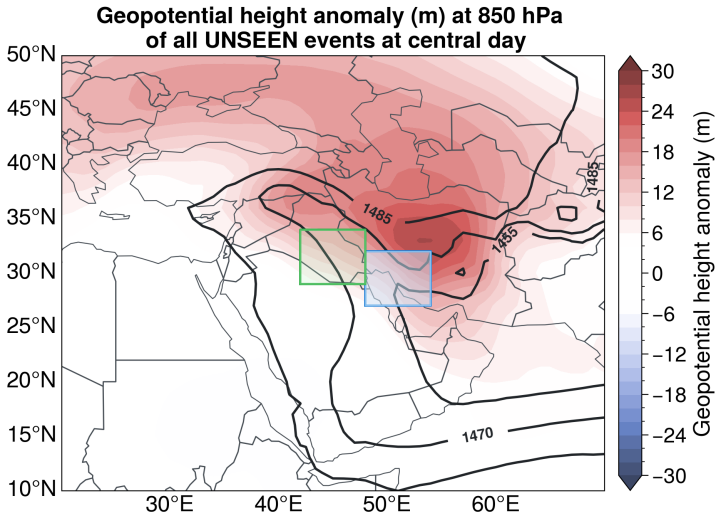

Figure 5.7: Geopotential height anomalies (color shading) at 850 hPa in the central day of the UNSEEN with the climatology (contour lines). The green box marked the heatwave area. Blue box indicates the TLI wich calculated as the averaged along the line over 27°-32° and 48°-54°E.

Figure (5.8) presents 2D histograms of the TLI and Shamal Wind Index (SWI) against Tmax anomalies, using ensemble forecast data from both real-time and hindcast summer periods. The shading color of both plots indicates the frequency (or density) of ensemble forecast members. In figure (5.8a), the ensemble forecasts are high density around zero anomalies (shading) with a slight tilt to the east, reflecting a moderate positive correlation (r=0.4) between Tmax anomalies and the TLI (Fig. 5.8a). This correlation indicates that higher Tmax anomalies are associated with the reduction of the low-level thermal low (i.e., positive TLI values). Similarly, in figure (5.8b), the shading slightly tilts to the west, indicating a negative correlation (r=-0.3) between Tmax anomalies and the SWI. This suggests that attenuated Shamal winds are linked to higher Tmax anomalies. Although these correlations are relatively weak, they are consistent with the physical understanding that suppressed thermal lows and weaker Shamal winds can both favor surface warming. We therefore use these indices as diagnostic tools for classifying UNSEEN events, while recognizing that the thermal and dynamical drivers of heatwaves are likely to be multi-factorial and not captured by single metrics alone.

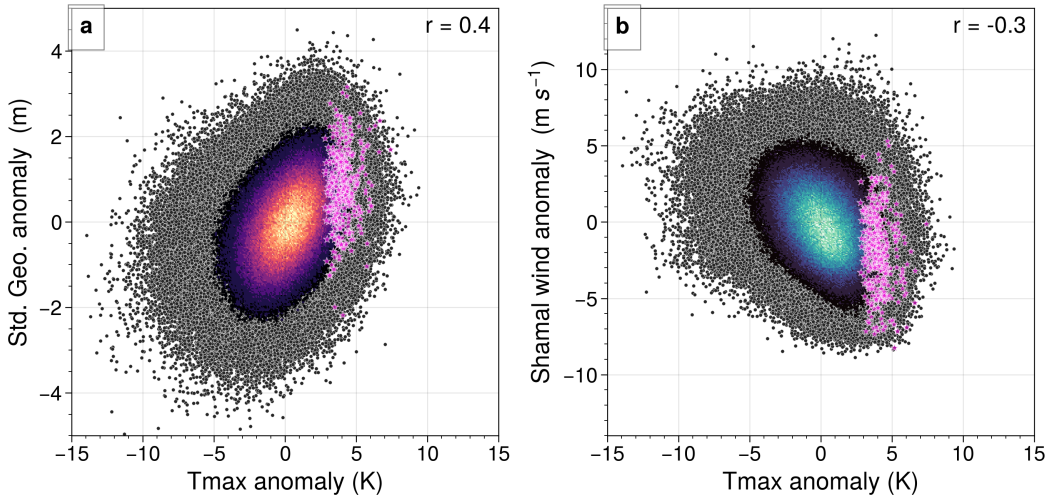

Figure 5.8: 2D histograms showing: (a) the low-level thermal low index, averaged along the line over 27°-32° and 48°-54°E, and (b) Shamal winds. In both plots, the x-axis represents Tmax anomalies from all ensemble forecast members across real-time and hindcast forecasts of 14-46 lead time. The color shading in both panels represents the density of the ensemble members. Black dots indicate individual members. Pink stars indicate the UNSEEN events.

5.3.2 Clusters Identification

In Chapter 3, our classification approach aimed to distinguish between events with and without Rossby wave activity. For this purpose, we used the strength of the upper-level anticyclonic pressure system as a metric, based on the assumption that the anticyclones are embedded in Rossby waves. However, this method did not reveal distinct groups—due to the limited number of events—with clearly different Rossby wave patterns. In addition, the events classified as non–RW did not exhibit a clear underlying mechanism. In the UNSEEN approach, this limitation is amplified, as composites reveal a systematically longer-lasting upper-level anticyclone compared to ERA5-based events, likely due to the selected forecast window (14–46 lead time). The main goals of using the UNSEEN approach are to investigate the ensemble size to explore the suggested Rossby wave patterns associated with heatwaves, in addition to identifying the key physical drivers of non–Rossby wave events. Thus, using only the anticyclone as a classification criterion is not meaningful, since we already know that the events fall into two groups—one associated with Rossby waves and the other not. Ultimately, this approach produces a repetition of the results presented in Chapter 3. To address this, we employed an alternative strategy based on mechanisms more directly linked to regional heatwave dynamics. Based on Figure(5.8), we classified these events considering the reduction of the local thermal low and attenuation of Shamal winds. To exclude moderate events, we removed events associated with TLI and SWI values near zero. This filtering ensures that only extreme events with a strong physical

signal are retained for analysis. Ultimately, the remaining events are categorized into three distinct clusters, defined as follows:

1. Events characterized by positive TLI and negative in SWI. These events (155 events) correspond to the patterns discussed in Chapter 3, where the thermal low is reduced and the Shamal wind is attenuated.

2. Events with positive SWI values (44 events) are, by definition, not associated with a weakening of the Shamal winds. In these cases, the Shamal wind remains stronger than climatology. As chapter (3), the strengthening of the Shamal wind can result from the intensification of either the thermal low or the high-pressure system over the northern Arabian Peninsula, or from the simultaneous strengthening of both. Ultimately, both positive and negative TLI values are present within this group.

3. Events with both negative TLI and SWI values (32 events) suggest a distinct physical driver of heatwaves associated with active ISM conditions. During strong monsoon phases, enhanced southwesterly flow from the Indian Ocean modifies the regional pressure patterns, weakening the typical north–south pressure gradient that drives the Shamal winds. Simultaneously, increased moisture and cloud cover reduce surface heating, weakening the thermal low. Together, these effects disrupt the usual Shamal wind mechanism, illustrating how tropical circulation interacts with regional dynamics.

Next, we analyzed these three clusters to investigate the associated dynamics and to identify the physical drivers behind the UNSEEN events.

5.3.3 Summary and Physical Interpretation of Clustered UNSEEN Events

Clusters Consistent with Rossby Wave Dynamics

We find that two of the three groups of UNSEEN events are associated with distinct Rossby wave activity, which we will demonstrate in the following: one group is characterized by Rossby Wave Propagation (RWP) and the other by Rossby Wave Breaking (RWB). These different Rossby wave activities potentially modify the lower-tropospheric dynamics associated with the Shamal winds, resulting in distinct heatwave-driving mechanisms.

In the RWP events, the wave train structure supports baroclinic development, which may enhance upward motion over Iraq. The analysis shows that attenuation of the Shamal winds begins around lag -4, nearly coinciding with an increase in Tmax anomalies (Fig. 5.9a).

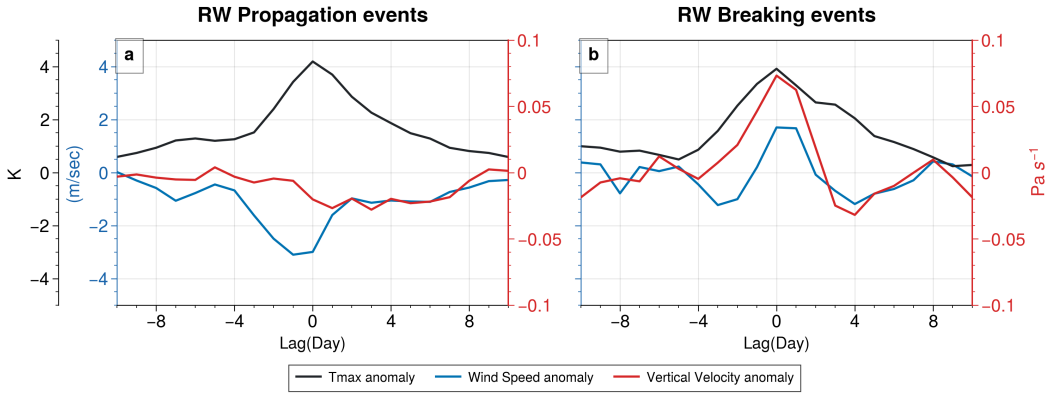

Figure 5.9: Tmax anomalies (black, unit: K), Shamal wind anomalies (blue, unit: m/sec) and vertical velocity anomalies (red, unit: Pa/sec) averaged over 41-45°E and 29-38°N. As ECMWF, the vertical velocity parameter indicates upward motion with negative values and downward motion with positive values. (a) RWP events and (b) RWB events.

This evolution suggests a feedback loop in which the weakening of the Shamal wind reduces horizontal advection, allowing warm air to rise more easily. The resulting ascent promotes further warming and drying of the lower troposphere, reinforcing heatwave conditions. At mid- and lower-tropospheric levels (Fig. 5.10 top row), anticyclonic anomalies over Central Asia extend southward but remain weak over Iraq. Near the surface (1000 hPa), high-pressure anomalies are shifted eastward, creating a baroclinic structure that persists through lag -3. By lag 0, a broad high-pressure system extends from the Iranian Plateau to the Arabian Sea, suppressing vertical motion over the thermal low region and weakening the pressure gradient that typically drives the Shamal winds.

In contrast, RWB events are dominated by subsidence and surface warming. Persistent anticyclonic anomalies at both 700 hPa and 1000 hPa coincide with downward motion over eastern and northern Iraq (Fig. 5.9b and Fig. 5.10, bottom row). These features strengthen around lag -3, enhancing surface heat via adiabatic warming.

Unlike the attenuation of the Shamal wind seen in RWP events (Fig.5.9a), which is attributed to the weakening of the thermal low in response to strengthened lower-level pressure height anomalies over southern Iraq and the Gulf (see contour lines in Fig.5.10c), RWB events feature intensified Shamal winds, driven by a stronger pressure gradient between a surface high over northern Arabia and the low-level thermal low to the south. This strengthening is linked to low-level high-pressure anomalies that remain confined over Iran and do not substantially affect the thermal low over southern Iraq and the Gulf, particularly in the region where the thermal low is defined (see contour lines in Fig. 5.10g).

The evolution of upper-level circulation further distinguishes these two types. In RWP events (Fig. 5.11), a Rossby wave train initiates in mid-latitudes (30–60°N) at lag -7, with quasi-stationary anticyclonic anomalies over Central Asia and Europe. These anomalies

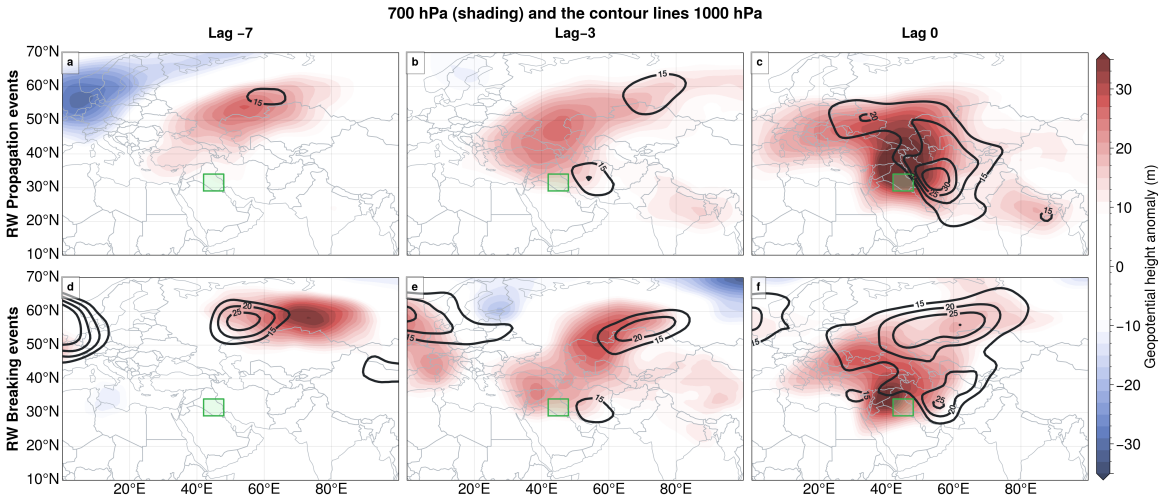

Figure 5.10: Composite-mean evolution of geopotential height anomalies at 700 hPa (shading) and at 1000 hPa (contours). **a** to **c**: Evolution of geopotential height anomalies of RWP events. **d** to **f**: The evolution of RWB events. The green box marks the heatwave area.

are embedded in the subtropical jet, which weakens and gradually shifts equatorward. By lag 0, the wave becomes more zonal, while the ISM outflow intensifies at upper levels, possibly expanding westward over the Arabian Sea.

RWB events (Fig. 5.12) show a contrasting pattern. A blocking anticyclone over the North Atlantic at lag -7 redirects wave activity equatorward into 30–50°N, guiding wave breaking over Iraq by lag 0. This shift in the wave pattern promotes downstream propagation over the eastern Mediterranean and northern Iraq, resulting in the development of upper-level anticyclonic anomalies that persist through lag 0. The downstream wave breaking coincides with enhanced ISM upper outflow from southern India and the Arabian Sea, supporting upper-level divergence and favoring subsidence to the west (as Fig. 5.9b). This reinforces the low-level anticyclone and supports sustained heatwave conditions.

Interestingly, RWP cluster shows a weakening of the thermal low and Shamal wind attenuation patterns consistent with our ERA5-based composite and case studies (Chapters 3 and 4). In contrast, RWB) cluster features strong Shamal winds and enhanced subsidence. This duality illustrates how different configurations of Rossby wave dynamics—propagation versus breaking—can yield contrasting yet equally impactful heatwave scenarios.

Indian Summer Monsoon ISM Cluster

The third cluster identified in our analysis suggests an additional physical driver of heatwave events linked to ISM activity. Figure 5.13 presents the geopotential height anomalies

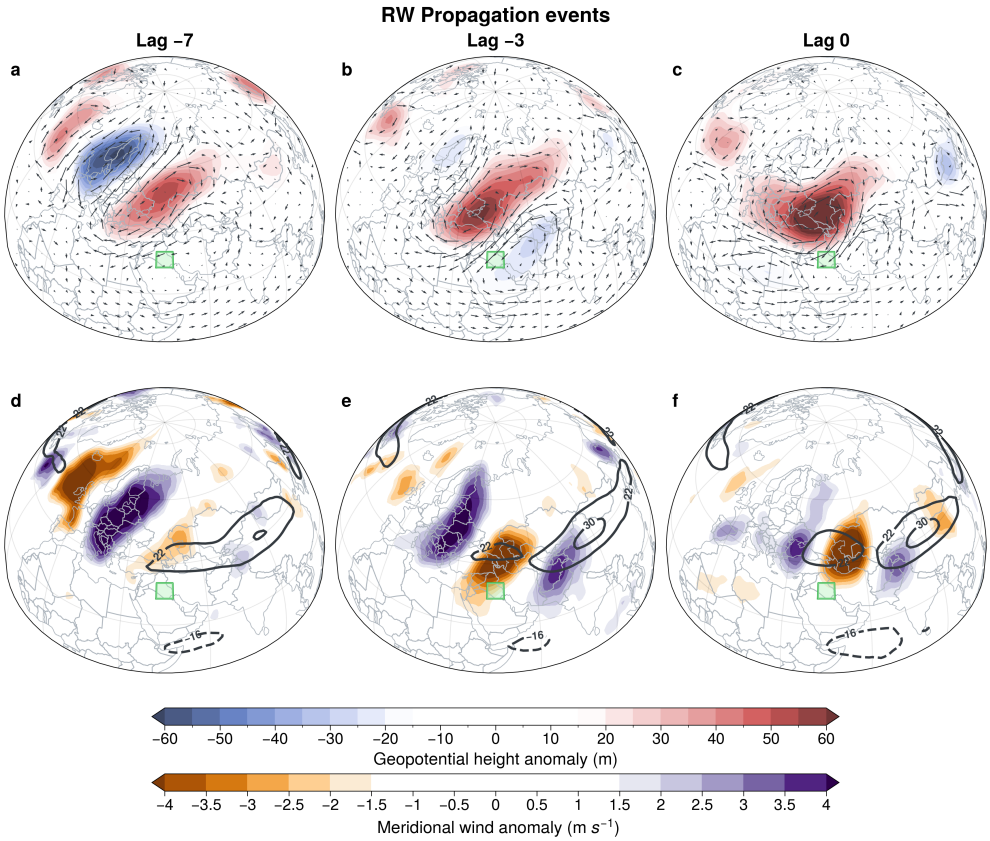

Figure 5.11: Different fields associated with RWP events. **a** to **c**: Evolution of geopotential height anomalies (shading) and horizontal wind anomalies (arrows). **d** to **f**: Evolution of meridional Wind anomalies (shading) and total Zonal Wind (contours, units: m/sec). All fields are shown at 200 hPa. Averaged over lag -7 preceding the event (a,d), averaged over lag -3 preceding the event (b,e), and averaged over lag 0 preceding the event (c,f). The green box marks the heatwave area.

at 200, 700, and 1000 hPa for this cluster. At the upper level, an anticyclone dominates over the Mediterranean region, forming a dipole pattern with significant cyclonic anomalies over the North Atlantic. This anticyclonic pattern is accompanied by anomalies of the upper jet, which stretches to the north of our target area. Notably, the core of this jet intensifies over northern Iraq, particularly across Turkey, extending near the Tibetan Plateau. Simultaneously, the easterly flow associated with the upper Indian Monsoon circulation intensifies across southern India and extends westward toward the Arabian Peninsula (Fig. 5.13a). This configuration aligns with weak negative geopotential height anomalies in the lower troposphere in the southern Arabian peninsula (Fig. 5.13b). These anomalies tend to be more pronounced near the surface, spanning the Arabian Peninsula and extending into the eastern Mediterranean (Fig. 5.13c). Negative geopotential height anomalies at 850 hPa extend across a broad latitudinal band (0–20°N) from southern India to the Arabian

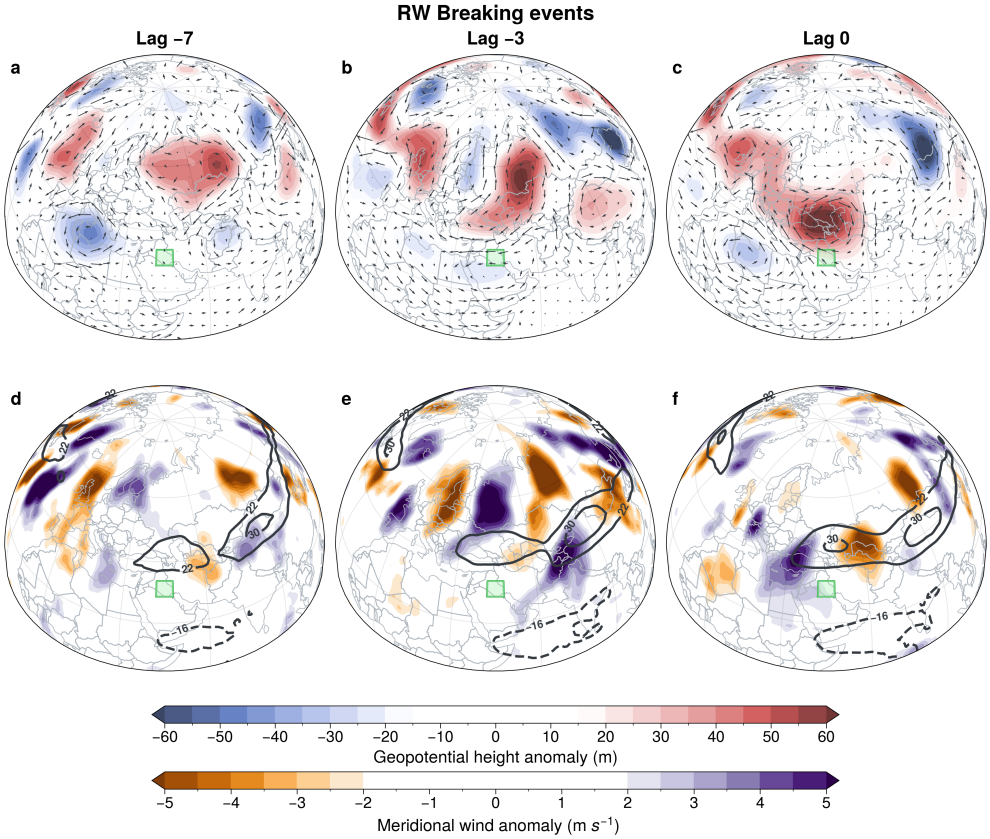

Figure 5.12: Smiler to (Fig. 5.11), however of RWB events.

Peninsula. Figure 5.14 highlights the lower-level anomalies (dashed contour lines) together with total cloud cover anomalies. For the RWP and RWB clusters, the results do not reveal a clear association between the low-level thermal low and the evolution of convection; instead, they show an absence of cloud cover anomalies linked to the upper-level anticyclonic system (Fig. 5.14a–c and 5.14d–f). In contrast, the ISM cluster shows that the thermal low associated with monsoon activity extends into the eastern Mediterranean, potentially enhancing deep convective activity in the region (Fig. 5.14g–i).

This deep convection is consistent with anomalies in the Total Cloud Cover (TCC) as illustrated in Figure (5.14g-i). At lag days -2 and -1, TCC anomalies intensify and coincide with negative geopotential height anomalies at 850 hPa. (Fig. 5.14g,h). This pattern persists at lag 0, though the anomalies become stronger and shift slightly northward, becoming more pronounced over India and the Arabian Peninsula (Fig. 5.14i). Furthermore, the dashed contour lines—representing negative geopotential height anomalies consistent with those seen at 700 and 1000 hPa—confirm that a broad region (5.13b), particularly Southwest Asia (north Arabian peninsula), is experiencing active ISM conditions. These conditions, in turn, exert an influence on the Shamal wind mechanism.

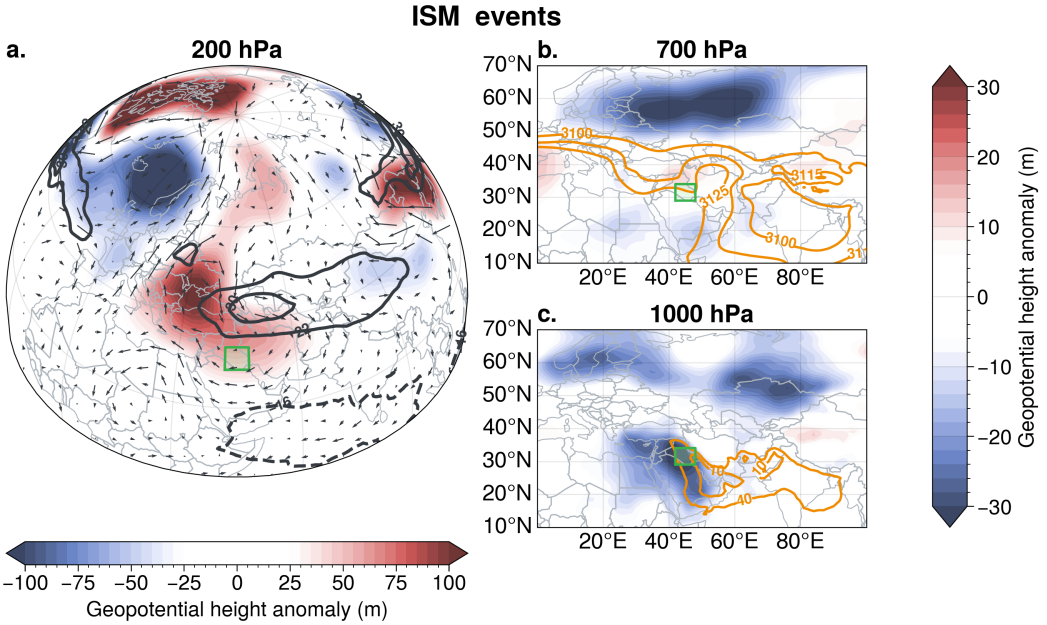

Figure 5.13: Geopotential height anomalies at lag 0 of Indian Monsoon-driven events at different pressure levels. (a) These anomalies at 200 hPa (shading) with total zonal wind (contours; units: m/s) at the same level, and (b) at 700 hPa (shading), with contour lines indicating also geopotential height anomalies, however, at 1000 hPa.

5.4 Discussion

The UNSEEN events approach reveals additional mechanisms driving heatwaves and provides deeper insights into Rossby wave–related dynamics, addressing several unresolved questions from the ERA5-based analysis. Although the S2S data may exhibit increased chaos beyond lag day 14—the window in which our heatwave identification is focused—this is not a limitation for the UNSEEN approach. On the contrary, this characteristic is essential, as the data still offers a coherent and physically plausible framework for understanding the underlying processes. This remains valid despite model uncertainties, particularly in processes like cloud formation, as the results show no significant discrepancies with established physical principles. This consistency enables the identification of a large number of heatwave events, which are not accessible through ERA5-based event analyses.

Even after removing the seasonal cycle, residual trends persist in the S2S data. Eliminating these typically requires a longer time series, which is unavailable for this dataset. However, the approach used in this chapter (removing the trend based on the day of year) helps mitigate the influence of low-frequency climate variability, such as ENSO, which could otherwise mask the subseasonal drivers of heatwaves and affect the interpretation of long-range forecasts.

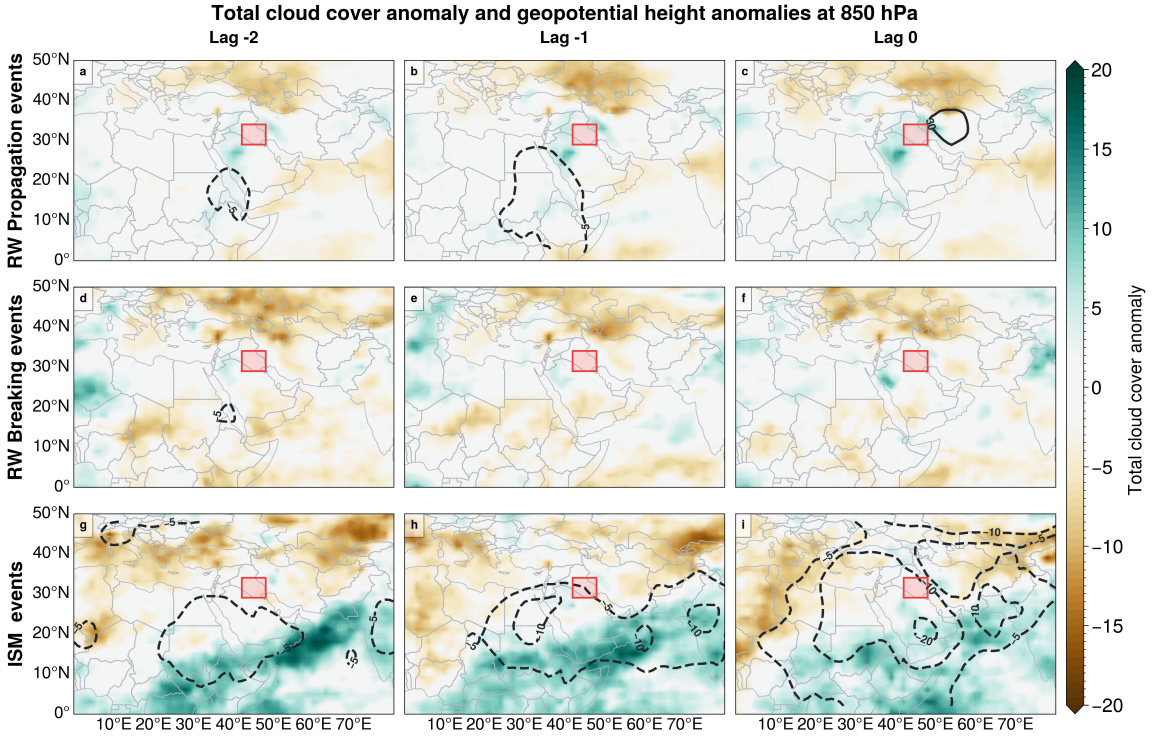

Figure 5.14: Evolution of total cloud cover anomalies (shading) and geopotential height anomalies (contour lines, negative values are dashed lines). **a** to **c** indicate the evolution of RWP events,**d** to **f**: of RWB events and **g** to **i**: of ISM events. The red box marks the heatwave area.

Composite-mean analyses of the UNSEEN events show that these anomalies are closely associated with upper-level circulation. The analysis confirms a robust synchronization between upper-level circulation anomalies and changes in local pressure patterns in the lower troposphere, both of which contribute to heatwave generation, as shown in Chapters 3 and 4. Upper-level anticyclonic anomalies consistently appear across different datasets (ERA5 and S2S) and are strongly linked with heatwave events. Their persistence likely enhances heatwave conditions.

A critical driver of these heatwaves is the low-level thermal low, a component of the Shamal wind system. Consequently, the attenuation of the Shamal wind is a key factor influencing heatwave evolution, although its strengthening can also contribute. Based on Shamal wind characteristics, most heatwave events are found to be associated with Rossby wave activity, particularly through wave propagation or breaking. When the Shamal wind weakens, this is often linked to a reduced pressure gradient between local high and low-pressure systems, a consequence of baroclinic structure that modifies the intensity of the dominant pressure patterns (Fig. 5.10a-c). This weakens the thermal low, which typically dominates the summer over southern Iraq and the Gulf region.

A weakened upper-level jet, acting as a waveguide, allows slowly propagation of Rossby waves. This slower movement enhances the persistence and intensity of embedded anticyclones. These upper-level anomalies often exhibit vertical tilt with those in the lower troposphere, especially over high terrain like the Zagros Mountains (Fig. 5.10a-c), reflecting increased atmospheric baroclinicity. These positive geopotential height anomalies over the Zagros extend over the thermal low, contributing to its weakening. This configuration weakens the low-level pressure gradient and disrupts the Shamal wind mechanism. Without this ventilation, surface temperatures rise, leading to enhanced upward motion of warm air overlying cooler air before events (Fig. 5.9a), intensifying heatwave conditions.

In contrast, Rossby wave breaking also leads to heatwave conditions, though through different mechanisms. The Shamal wind generally cools the region through ventilation. However, during RWB events, a persistent upper-level anticyclone, intensified by wave breaking, can increase the low-level pressure gradient and strengthen the Shamal wind. Despite stronger winds, anticyclonic conditions still promote subsidence and clear skies, increasing solar radiation and downward motion before events (Fig. 5.9b). These processes override the Shamal wind's cooling effect and contribute to heatwave development.

Both clusters are potentially associated with different patterns of the upper-level circulation of ISM. Figure 5.15a shows anomalies standardized in the Webster and Yang Monsoon Index (WYMI), which represents the vertical shear between zonal winds at 850 hPa and 200 hPa over the ISM region (Fig. 5.15b) (Webster and Yang, 1992). The WYMI for RWP events declines further into the negative phase in the days preceding the central day, suggesting disturbances in ISM circulation. For RWB events, the WYMI exhibits a more persistent negative phase of the ISM circulation.

These various anomalies of WYMI are closely linked to changes in the upper-level jet structure. One potential driver is enhanced heating over the Tibetan Plateau, which reduces the meridional temperature gradient and weakens the pressure gradient that sustains the subtropical westerly jet (Zeng et al., 2024; Zhu et al., 2021; Sha et al., 2020). As this jet weakens and shifts, upper-level divergence increases, which in turn strengthens the Tropical Easterly Jet (TEJ) (Liu et al., 2024; Huang et al., 2021). The evolution of the TEJ therefore coincides with the weakening, displacement, or reshaping of the subtropical westerly jet (Liu et al., 2024). Long-lasting Rossby wave trains can further reinforce the TEJ through persistent upper-level anticyclonic anomalies, which are reflected in the easterly flow (u-component at 200 hPa) of the WYMI (Zuo et al., 2013). Simultaneously, the baroclinic structures of these Rossby waves may suppress deep convection by maintaining high-pressure anomalies over the Zagros and southern Iran. These anomalies disrupt low-level convergence (u-component 850 hPa) and moisture transport, which in turn weaken the thermal low over southern Iraq and then attenuate the Shamal winds, thereby creating favorable conditions for RWP-driven heatwave events.

During RWB events, the intensified Tibetan Plateau height sustains the subtropical jet,

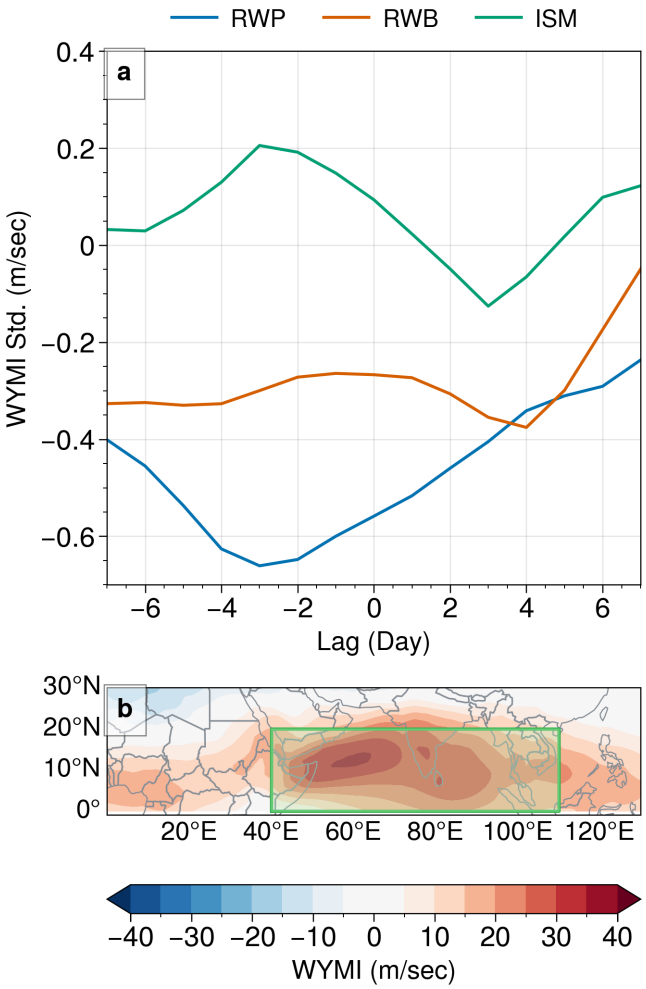

Figure 5.15: (a) Anomalies of the Webster and Yang Monsoon Index (WYMI) for RWP events (blue), RWB events (brown), and monsoon events (green); (b) Climatology of the WYMI based on all ensemble members during JJA for lead times between 14 and 46 days. The green box indicates the region spanning 0–20°N and 40–110°E used to define the WYMI, following Webster and Yang (1992).

enhancing its role as a waveguide for Rossby waves (Fig.5.12b and e). This favors the propagation of Rossby waves toward the Middle East, where their subsequent breaking occurs. The associated circulation enhances upper-level divergence, thereby strengthening the TEJ, which remains sustained before and during the events (Li et al., 2022; Chen and van Loon, 1987). Since the pressure patterns embedded within the Rossby wave do not substantially disrupt the convergence of the low-level inflow of ISM (i.e., westerly flow), the low-level thermal low to the south of our target area remains active. Although the WYMI exhibits a negative anomaly—indicating strong upper-level easterlies associated with strengthening of the TEJ—the weak low-level inflow constrains the development of

the monsoon circulation (Zuo et al., 2013; Pattanaik and Satyan, 2000). This weak inflow appears to be unrelated to the evolution of the low-level thermal low and that keeps the Shamal wind mechanism valid. The persistence of this mechanism is attributed to downstream upper-level anticyclones reinforcing low-level anticyclonic anomalies over the northern Arabian Peninsula, thereby increasing the pressure gradient and intensifying the Shamal wind (Fig.5.10d–f). The associated subsidence under these anticyclonic conditions further amplifies heatwave intensity (Fig. 5.9b).

Another group of heatwave events appears to be linked to ISM activity. During these events, the subtropical jet strengthens over northern Iraq, inhibiting the zonal eastward extension of upper-level anticyclonic anomalies (Fig. 5.13a). This configuration coincides with a strengthening of easterly flow over the Monsoon region. However, the WYMI exhibit a positive phase preceding the central day of the event, suggesting a strong inflow of the ISM (i.e., intensified low-level flow at 850 hPa; Fig. 5.15, green line). These conditions favor enhanced upward motion and the development of low-pressure anomalies that extend westward into the Arabian Peninsula. In turn, this promotes convection and cloudiness (Fig. 5.14), modifies pressure systems over the northern Arabian Peninsula, and disrupts the Shamal wind. The thermal low becomes increasingly influenced by ISM activity, expanding into the northern Arabian Peninsula (Zuo et al., 2013). This reduces the pressure gradient that typically drives the Shamal wind, resulting in its attenuation (Fig. 5.12b).

Chapter 6

Conclusions, Discussion, Outlook

The main question in this thesis is: **What are the dynamical drivers and predictability characteristics of extreme heatwave events over Iraq, and how do large-scale and regional processes interact to produce these events?**. However, this question shows sub-questions during our analysis that we attempt to summarize their answers and discuss here.

6.1 Research questions

What are the dominant circulation patterns giving rise to heatwave events affecting Iraq?

Our analysis shows that most heatwave events in Iraq are associated with large-scale upper-level circulation patterns that influence and modify local dynamics, creating favorable conditions for extreme surface temperatures. These patterns shape the evolution of extreme temperatures through two main dynamic pathways:

1. **Midlatitude Dynamics:** Heatwaves over Iraq are strongly influenced by midlatitude processes, particularly the propagation and breaking of **Rossby waves**. Based on ERA5 reanalysis data, we identified **29** heatwave events during the summer seasons of 1980–2022 that were associated with Rossby wave activity. The application of the **UNSEEN** approach using S2S data revealed a substantially larger sample of **199** events related to Rossby wave dynamics, drawn from two datasets (2021–2022) and comprising **10,560** hindcast members across 20 years and **2,448** real-time forecast members. The **upper-level subtropical jet stream** plays a dual role in modulating

these heatwave-inducing patterns. First, it acts as a **waveguide** for Rossby waves, allowing **quasi-stationary anticyclones** embedded in the wave train to become dominant and persist over downstream regions such as Iraq. Second, during Rossby wave breaking, the jet stream helps confine the associated **upper-level stationary anticyclones** over Iraq and its vicinity. These anticyclones enhance subsidence, suppress cloud formation, and promote adiabatic warming, creating favorable conditions for extreme surface temperatures.

2. **Tropical Influences:** Tropical circulation patterns, particularly the **Indian Summer Monsoon (ISM)** and associated **tropical upper-level jet**, can also contribute to heatwave development over Iraq. These influences were identified in **16** ERA5-based heatwave events and in **32** events using the **UNSEEN** approach with S2S data. Prolonged ISM activity, even when weak, can lead to thermodynamic conditions favorable for heatwave formation in Iraq, especially in the absence of strong midlatitude forcing. Shifts or weakening of the **upper-level subtropical jet stream** can allow the **Tropical Easterly Jet** to expand, widening the monsoon outflow region. This can enhance low-level monsoon inflow into Iraq, modifying the low-level thermal low-pressure system through increased deep convection, thereby contributing to extreme temperature conditions.

What is the role of the local process that is considered a key regional factor in heatwave evolution?

A key local factor in the evolution of heatwaves over Iraq is the presence and modulation of the low-level northwesterly jet known as the **Shamal winds**. These winds play a complex role in heatwave evolution. For example, their strengthening can enhance surface warming through dry advection, reduced humidity, and the suppression of cloud formation, factors that promote radiative heating. Another factor, the attenuation or weakening of the Shamal winds, can also contribute to heatwave intensification, as stable air and diminished ventilation lead to heat buildup near the surface, supporting the evolution of extreme heat events.

The Shamal wind mechanism is primarily driven by the pressure gradient between a low-level thermal low spanning over southern and southeastern Iraq and a local anticyclone located over the northern Arabian Peninsula. In addition, they are significantly influenced by the complex orography of Iraq and its surrounding region. For example, the presence of the Zagros mountains in Eastern Iraq intensifies the Shamal wind through a narrow channel. Heatwaves in both Rossby wave-related and Indian summer monsoon-related cases are linked to the Shamal wind modulation.

What is the interaction between large-scale dynamics (Rossby waves and monsoon circulation) and regional mechanisms (e.g., Shamal winds, topography) contributing to the intensity of Iraqi heatwaves?

Based on our results, three dominant Rossby wave patterns, along with monsoon-related activity, may be identified as the primary large-scale processes that influence the Shamal wind system and modify local atmospheric conditions contributing to heatwave intensity in Iraq. All these processes are linked to variations in the subtropical upper-level jet, which either weakens or shifts in position, leading to the development of he following heatwave scenarios:

1. **Quasi-Stationary Anticyclone Events (Barotropic Rossby Wave Pattern):** These events are associated with a long-lasting upper-level anticyclone that is embedded within slowly propagating Rossby waves (Chapter 3). The vertical structure is predominantly barotropic, supporting strong subsidence and surface warming across the Middle East, including Iraq, for several days. This anticyclonic flow also induces down-slope winds, similar to Foehn winds, on the lee side of the Zagros Mountains, further contributing to adiabatic heating. These down-slope winds suppress the gentle residual Shamal winds that typically develop due to Iraq's north-to-south topographic sloping, weakening their cooling effect. As demonstrated in the case study (Chapter 4), these dynamics intensify vertical advection, thereby promoting surface heat accumulation.

2. **Baroclinic Rossby Wave Events with Local Ridge Enhancement:** In this group, the Rossby wave pattern exhibits a more baroclinic structure, inducing or amplifying a local ridge that extends into the lower troposphere over the Zagros region and vicinity (Chapters 3 and 5). This configuration modifies the lower pressure systems, particularly weakening the low-level thermal low over southern Iraq. As a result, the pressure gradient that drives the Shamal wind tends to weaken, leading to Shamal wind attenuation. This attenuation reduces its cooling effect, thereby contributing to increased surface temperatures.

3. **Rossby Wave Breaking Events:** These events involve the breaking of Rossby waves, leading to the formation of an upper-level anticyclone that reinforces local high pressure over the northern Arabian Peninsula (Chapter 5). Although this configuration strengthens the surface pressure gradient and enhances the Shamal wind, the associated subsidence over northern Iraq leads to increased surface temperatures. In this case, the Shamal wind does not act as the cooling factor and instead advects warm air from higher-altitude northern Iraq toward the south. Combined with slow subsidence, this enhances adiabatic warming, further intensifying heatwave conditions.

4. **Monsoon-Connected Events:** Some events are linked to enhanced summer Monsoon activity over the Indian subcontinent (Chapter 5). The ISM circulation is associated with a broad thermal low spanning the tropics and extending northward into the Arabian Peninsula. This expansion alters the regional pressure gradients that typically drive the Shamal wind in Iraq. As the monsoon-induced low expands, the pressure gradient weakens or reverses, leading to modifications to the Shamal wind. This configuration enhances the heat accumulation tendency near the surface, creating favorable conditions for extreme heatwave development in Iraq.

Since heatwave events are strongly linked to large-scale circulation patterns, how well do Subseasonal to Seasonal (S2S) ensemble forecasts capture these events and their associated dynamics?

The high predictability of heatwave events in short-range forecasts is largely attributable to the long-lasting and spatial scale of the associated large-scale circulation patterns, such as quasi-stationary anticyclones. These pressure systems enhance the surface temperature signals and are well-resolved by numerical models due to their (i.e., anticyclones) slow evolution and large-scale structure. Notably, events associated with Rossby wave activity show relatively high predictability even at extended lead times. This is because Rossby waves are large-scale, slowly evolving features that are better captured by S2S models, which are designed to represent broad circulation patterns. The consistent representation of these wave structures in the models contributes to the reliable forecasting of heatwave events. Moreover, since the evolution of the Shamal wind is closely tied to the large-scale circulation, particularly the presence and configuration of Rossby waves, the accurate prediction of these broader dynamics enhances the forecast skill of regional features like the Shamal winds, despite their smaller spatial scale.

6.2 Limitations

Through our analysis in this thesis, several limitations were identified that may constrain the interpretation of the results. One fundamental challenge is the lack of observational data over Iraq, such as radiosonde data. Key variables such as surface and upper-air temperature, wind components, and wind profiles are either entirely unavailable or have significant gaps due to conflict and instability. In particular, the massive absence of temperature observations limits the ability to validate and assess the accuracy of the reanalysis heatwave events. This scarcity of ground-truth data presents a major limitation to fully evaluate the reliability of the results derived from ERA5 and S2S data. The other limitations are primarily related to the ERA5 reanalysis data and the Subseasonal to Seasonal (S2S) forecast datasets, which are discussed in detail below.

6.2.1 Limitations of ERA5 Reanalysis Data

- **Representation of Small-Scale and Local Processes:**

  Although ERA5 is among the most advanced reanalysis datasets currently available, its spatial resolution of approximately 30 km remains insufficient for accurately capturing small-scale and localized atmospheric processes (Belušić et al., 2018; Zhu and Atkinson, 2004). In particular, ERA5 struggles to represent the complex interactions between mesoscale circulation features and regional topographic influences, such as the Zagros Mountains and the surrounding terrain. For example, down-slope winds, such as Foehn-like winds, are often driven by the orographic forcing of the Zagros range and can lead to enhanced vertical advection of warm air, significantly increasing near-surface temperatures in affected regions. Similarly, the Sharqi wind, a hot and dry southeasterly wind that typically occurs during late spring and summer, contributes to extreme heat conditions over southern and central Iraq. These local wind systems interact with orography and thermal gradients in ways that are often not well represented in ERA5. As a result, the dataset may underestimate the intensity or miss the occurrence of heatwave events influenced by these sub-regional dynamics.

- **Biases in Extreme Temperatures:**

  ERA5 reanalysis datasets may underestimate or overestimate extreme temperature events due to model smoothing and limitations in data assimilation systems (Keune et al., 2025). These biases are particularly evident in regions with limited observational input, such as Iraq. For example, on 2 June 2006, a date identified as part of an ERA5-based heatwave event, the maximum temperature recorded at the Basra station in southern Iraq was approximately 1°C higher than the corresponding ERA5 grid point closest to the station.

- **Regional Biases:**

  Lavers et al. (2022) showed lower skill of ERA5 in representing key variables, such as precipitation and potential evaporation, in tropical regions, compared to its higher performance in higher latitudes. This limitation is potentially relevant for this study, as a subset of the identified heatwave events appears to be connected to tropical dynamics as Non-RW events in chapter 3, including monsoon-related activity. Heatwaves influenced by the Indian Summer Monsoon or tropical upper-level circulation could involve processes such as increased latent heat release, tropical wave propagation, or moisture transport, all of which are harder to resolve accurately in ERA5. Therefore, these aspects could be underrepresented in ERA5, which introduces uncertainty into the analysis of the events' dynamical drivers and intensity.

6.2.2 Limitations of S2S Forecast Data

Substantial limitations

- **S2S ECMWF Model Forecast as a Large-Scale Model:**

  The S2S ECMWF forecast model is considered a large-scale model due to its horizontal resolution, which limits its ability to capture mesoscale and local features. Up to day 15, the atmospheric model operates at a spectral resolution of Tco639 (approximately 16 km), and beyond day 15, it drops to Tco319 (approximately 32 km). Further, the corresponding wave model resolution is 0.25° up to day 15 and 0.5° thereafter. These spatial scales are well suited for resolving large-scale atmospheric features such as Rossby waves (spatial scales between 1,000–2,500 km), jet streams, and monsoon circulations. This resolution enables the model to represent planetary-scale dynamics effectively, as illustrated by the comparison between S2S forecasts and reanalysis in capturing Rossby wave patterns in the case study in Chapter 4. Although the S2S model provides higher spatial resolution than ERA5 during the first two weeks of forecasts, its resolution drops thereafter to match that of ERA5. As a result, similar limitations in representing small-scale features apply beyond the initial forecast period.

  Moreover, large-scale processes associated with active teleconnections, such as the El Niño–Southern Oscillation (ENSO) and the Madden-Julian Oscillation (MJO), can enhance the skill of S2S forecasts in the first 2 weeks (Maier-Gerber et al., 2021; Lee et al., 2018). For instance, sea surface temperature (SST) gradients driven by these teleconnections may influence the intensity and position of thermal lows over southern Iraq or the Indian summer monsoon system (Yan et al., 2021). However, overestimation or underestimation of these teleconnection signals in the model can lead to inaccuracies in the simulated physical response, for example, strengthening or weakening the Shamal winds. Such biases can alter regional ventilation patterns and either suppress or amplify the development of heatwaves, ultimately affecting the forecast's reliability in capturing extreme temperature events.

- **Uncertainty of model or processes:**

  Complex processes, such as convection, cloud formation, and surface fluxes, are mostly parameterized in simplified modules within S2S models. This simplification leads to uncertainty in estimating heatwaves and their duration, and such uncertainty increases with forecast lead time Dutra et al. (2021). Although this uncertainty was investigated in Chapter 5 to explore new physical drivers of heatwaves, it also limits the model's ability to represent the local and small-scale processes contributing to heatwave evolution, as identified through the UNSEEN approach.

  This limitation affects the predictability of heatwave events, particularly those driven by local or mesoscale processes. In Chapter 4, when evaluating the model's skill of

Non-RW events (even with small-sized events), the model showed limited or no skill in predicting the GHI (Geopotential height Index). Indeed, this result aligns with our understanding that large-scale processes did not primarily drive these heatwave events. This presents a challenge when evaluating the model's performance, as it lacks sufficient skill to capture heatwaves influenced by local or mesoscale dynamics. This underscores a key limitation in the model's ability to represent small-scale features, which are crucial for understanding and forecasting heatwave development in complex regions such as southern Iraq.

For instance, land–atmosphere interactions become particularly important during transitional periods, such as the onset of the monsoon, involving intricate feedbacks between soil moisture, surface heat fluxes, boundary layer dynamics, and atmospheric stability (Dutra et al., 2021). S2S models may inadequately represent the influence of surface warming on local convection and precipitation, especially in monsoon-affected regions. Additionally, soil–vegetation–atmosphere coupling plays a critical role through processes like evapotranspiration. Disruptions such as deforestation can reduce evapotranspiration, extend dry periods, and ultimately affect the timing and intensity of monsoon onset and withdrawal. These factors contribute to additional uncertainties in simulating heatwave behavior during monsoonal transitions.

- **Chaotic Nature of S2S Forecasts:**

  The S2S ECMWF model shows the highest forecast skill during the first week, as seen in the predictability of both Rossby wave and non-Rossby wave-related heatwave events in Chapter 4. However, in mid to far lead times, the forecast skill declines sharply due to the chaotic nature of the atmosphere, which imposes a fundamental limit on predictability (Shen et al., 2022; Maier-Gerber et al., 2021). The UNSEEN analysis in (Chapter 5) based on a perfect-model assumption, removes the influence of model error to isolate physical drivers. However, this idealized framework does not remove the intrinsic chaotic nature of the atmosphere and cannot fully capture all real-world complexities, meaning that the model's representation of physical drivers may still differ from reality.

S2S Data Handling limitations

- **Ensemble size and run frequency:**

  As discussed in Chapter 4, the S2S dataset employs 11 ensemble members for each hindcast year and 51 members for real-time forecasts. This small ensemble size of the hindcast years introduces sampling errors, for example, in the removal of the seasonal cycle, which is a critical step for anomaly-based analyses. This limitation also affects the assessment of forecast skill and predictability. Even though the case study analysis was built on the period 2018–2022, to avoid the small ensemble size, certain lead times are based on only 11 members, which may weaken the reliability

of performance metrics such as RMSE. Further, this limitation could have influenced the UNSEEN event analysis (Chapter 5), where only the S2S datasets for 2021 and 2022, along with their associated hindcasts, were used to explore the physical drivers of heatwaves. Although the UNSEEN approach generated many events, the analysis was restricted to only summer seasons. This short time window and limited ensemble size reduced the diversity of circulation patterns captured, making it more difficult to study rare or particularly complex heatwave events.

Furthermore, the S2S model runs only twice per week, creating gaps between initialization dates. This produces missing lag times for some events and reduces the temporal continuity to track event evolution or onset with precision.

- **Hindcast Length Limitation:**

  Due to the twice-weekly initialization of the S2S ECMWF model, we used a day-of-year approach to remove the seasonal cycle and linear trend. However, the available hindcast record spans only 20 years, which may be insufficient to robustly sample interannual modes (e.g., ENSO, MJO, NAO) or lower-frequency climate drivers that modulate Rossby wave activity and short-lived blocking patterns. Modes such as the Pacific Decadal Oscillation (PDO), Atlantic Multidecadal Oscillation (AMO), and monsoon onset/break phases evolve over much longer timescales. Moreover, linear trends related to anthropogenic climate change typically require more than 20 years to be reliably isolated. As a result, the 20-year hindcast may still carry residual long-term trends, potentially biasing anomaly detection and heatwave attribution.

- **Varying IFS model cycle:**

  The S2S ECMWF dataset employed different IFS model cycles across time, which vary in both vertical resolution and initialization sources. In Chapter 4, data from 2018–2022 were investigated to increase the ensemble size for skill assessment. For example, the data set of 2018 and part of 2019 were initialized using ERA-Interim (91 vertical levels), while the others used ERA5, which offers higher vertical resolution (137 levels). This vertical resolution difference affects the model's ability to represent inconsistencies in the atmospheric layers, particularly in the low-level atmosphere associated with the Shamal wind dynamic. At least 10 levels differ between these models just in the low levels, which can lead to errors in capturing low-level jets and near-surface temperature gradients, resulting in biases in both wind strength and heatwave-related surface temperatures.

  Furthermore, different initialization datasets (ERA-Interim and ERA5) contribute to discrepancies in thermal structures at the start of each forecast. These inconsistencies can propagate through the model and lead to divergent surface temperature forecasts, particularly in regions such as southern Iraq (the heatwave target area) and the northern Gulf. In these areas, differences in land–atmosphere coupling and initial thermal conditions between model cycles may further influence the representation of heatwaves. These inconsistencies also appear within the model itself when compared

to the initialization data. For example, during the real-time forecasts of 2020 (which used ERA5 as initial conditions), the IFS model cycle shows a noticeable gap between the ensemble mean and the reanalysis at the initial lead time, where a close agreement is typically expected since the forecast is just beginning. Figure(6.1) shows this gap in the SST variable during the May–July initialization period over the Arabian/Persian Gulf. Such discrepancies can lead to increased divergence throughout the lead time, potentially contributing to overestimated anomalies. Furthermore, a shift occurs at lead time day 15 due to the transition from the high-resolution forecast module to the extended-range S2S forecast configuration. This model switch introduces an additional limit, which may further affect the consistency and reliability of the heatwave events.

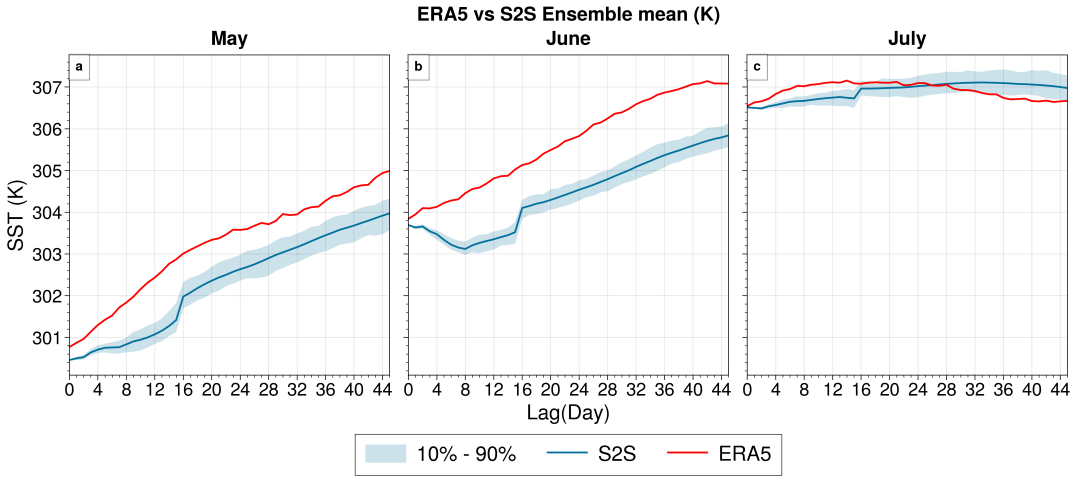

Figure 6.1: Sea Surface Temperature SST averaged over the Arabian/Persian Gulf of ERA5 (red) and S2S ensembles mean (blue) of the 2020 real-time dataset of May-July. Shading indicates percentiles of the ensemble members between 10-90%.

- **Data availability:**

  The S2S ECMWF model provides daily average values of 2-meter temperature (T2m) by default, which does not align with the variable used in ERA5 reanalysis data, where daily maximum T2m based on hourly data was used to define heatwave events. To address this inconsistency, Chapters 4 and 5 used available 6-hourly T2m data from the S2S model to approximate daily maximum temperature by selecting the highest value from each day. This technical limitation led us to employ the S2S data as a **Truth** throughout the analysis. In other words, we only investigated the dates of heatwaves identified in the reanalysis data to examine how they evolved in the S2S forecasts. This approach was based on the assumption that the first forecast step of the S2S output closely represents the initialized state, as early lead times are expected to reflect minimal forecast uncertainty and limited divergence due to atmospheric chaos.

Another limitation is the unavailability of some key variables needed for the analysis. For example, Potential Vorticity PV is only provided at the 320 K isentropic level in the S2S ECMWF dataset, which is insufficient for examining upper-level dynamics in tropical regions, especially the monsoon upper troposphere. Although it is theoretically possible to estimate PV using relative vorticity and interpolate it to the required pressure or isentropic levels, the limited vertical resolution of the model output makes such interpolation unreliable.

6.3 Research Outlook and Expansion

In this thesis, we aimed to provide a coherent understanding of heatwave events over Iraq during the summer season. In the following, we outline potential research pathways that are related to our findings of this work and highlight subjects that require further investigation in future studies.

Improving Representation of Small-Scale Processes

Our analysis is built on large-scale models, specifically ERA5 reanalysis and the S2S ECMWF forecasts. While these models effectively capture broad atmospheric patterns, they are insufficient in representing local and mesoscale processes that are critical to heatwave evolution, which were highlighted in the limitations. Future research could benefit significantly from incorporating high-resolution models able to resolve mesoscale dynamics. However, running such models (e.g., with 1–5 km resolution) at a continental or seasonal scale can be computationally expensive. Therefore, downscaling or nested regional simulation techniques using models such as ICON or WRF may provide enhanced insights. High-resolution modeling would better capture local features such as:

- Sharqi winds and Foehn-like down-slope winds.
- Orographic effects of the Zagros Mountains, such as the blocking effect, channeling.
- Small-scale land–atmosphere interactions in the lower troposphere.
- Mesoscale thermodynamic and dynamic processes, such as those driven by local topographic circulations, land–sea thermal contrasts, sea breezes or low-level jets, can play a role in the onset and persistence of heatwaves. These include local diabatic heating, enhanced subsidence associated with shallow anticyclonic systems, and adiabatic warming due to terrain-induced down-slope winds. Additionally, the presence of pre-existing warm and dry air masses could be amplified by mesoscale advection into the heatwave region.

In addition, regional climate models (e.g., CORDEX models) offer valuable platforms for testing various physical parameterizations that can improve the simulation of heatwave processes, especially in topographically complex and arid regions like Iraq. These models also enhance future climate projections by resolving regional-scale feedbacks and variability, thereby improving the assessment of heatwave trends and their potential impacts under different climate scenarios.

Upper-Level Circulation and Shamal Wind Evolution

As highlighted throughout this thesis, the Shamal wind plays a crucial role in driving heatwave dynamics across southern Iraq. A deeper understanding of its evolution is therefore essential to advancing knowledge of regional atmospheric processes. Typically, the Shamal wind is understood as a response to the surface pressure gradient between the low-level thermal low over southern Iraq and the local pressure high over the northern Arabian Peninsula. However, this balance is sensitive to modulation by large-scale atmospheric variability.

Teleconnection patterns such as ENSO and MJO can alter the strength and structure of the thermal low, thereby influencing the occurrence and intensity of the Shamal winds. Furthermore, upper-level monsoonal anticyclones may modulate the Shamal through mechanisms such as eddy shedding, upper-tropospheric wave activity, or shifts in the subtropical jet. These interactions can enhance or suppress the vertical and horizontal structure of the Shamal circulation.

Future research should aim to clarify how upper-level circulation patterns and teleconnection phases interact with surface features to influence the Shamal wind. Understanding this coupling is essential for improving predictions of regional heatwave behavior, particularly under future climate change scenarios.

Uncertainty of the S2S module in summer time

In this thesis, we investigated the S2S dataset to forecast heatwave events (Chapter 4) and expand the sample size for analyzing the physical drivers of heatwaves (Chapter 5). However, the uncertainty of the S2S model was not fully addressed in this study. The summer season (June–August) is characterized by active deep convection in the tropics, particularly in regions influenced by the Intertropical Convergence Zone (ITCZ) shift. Areas such as the southern Arabian Peninsula and India are strongly affected by monsoonal dynamics, making them critical for evaluating the performance and uncertainty of S2S forecasts. Understanding how model uncertainty manifests in these convectively active and dynamically complex regions is crucial for enhancing S2S forecast reliability and interpreting its

relevance to heatwave prediction.

Climate Change and Anthropogenic Influence

Future climate change scenarios could offer deeper insights into the mechanisms driving heatwaves by projecting how large-scale circulation patterns, local thermodynamics, and land–atmosphere interactions may evolve under increased greenhouse gas forcing. These scenarios can reveal potential shifts in the frequency, intensity, and spatial distribution of heatwaves, as well as changes in the relative importance of different physical drivers. In addition to natural variability, human activities, such as deforestation, urbanization, and industrial emissions, also contribute to the frequency and intensity of heatwaves. Assessing the combined effects of global climate change and regional anthropogenic factors is crucial for understanding future heatwave risks and developing more targeted adaptation strategies.

Appendix A

Chapter 3 plots

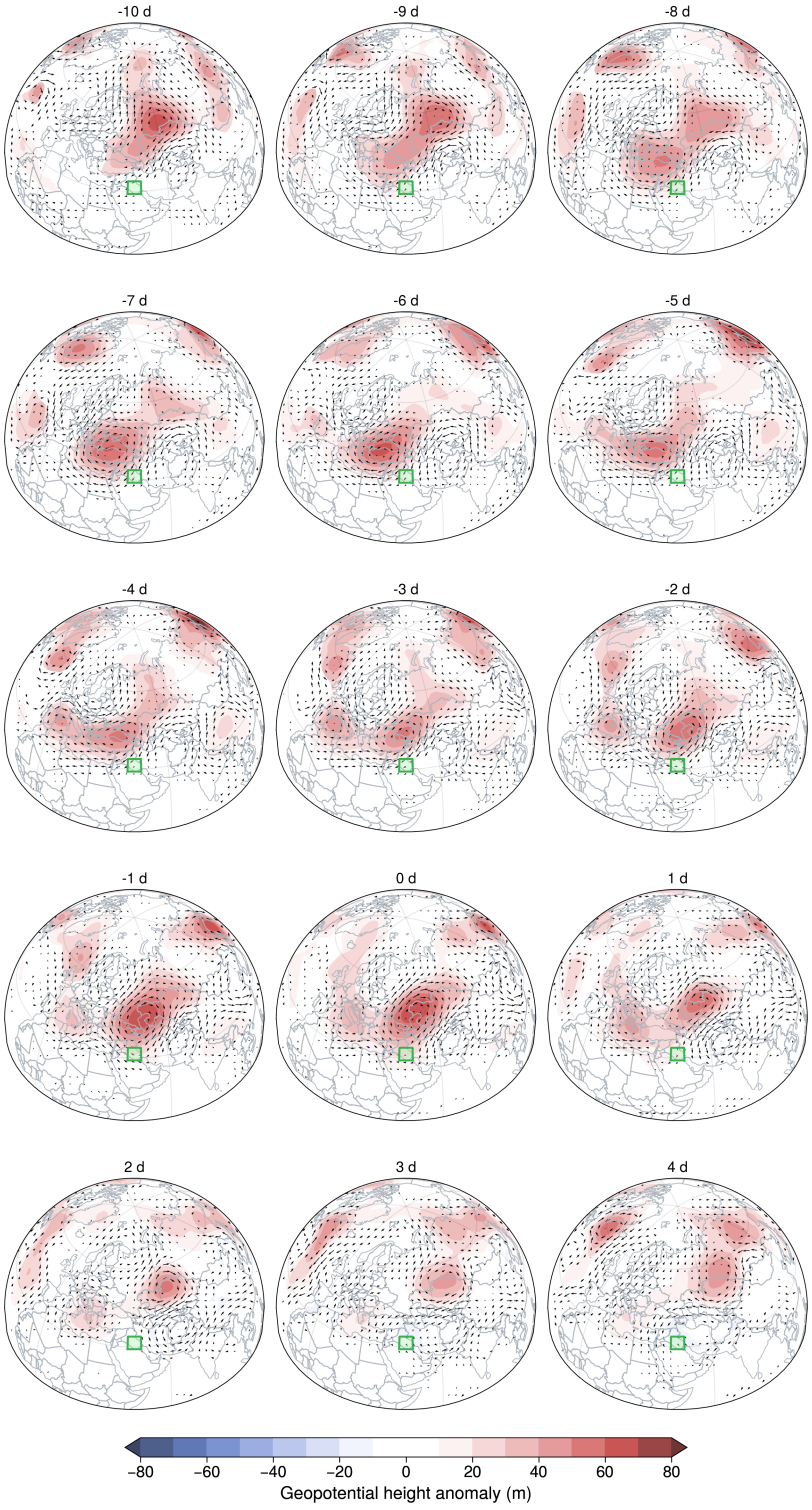

Figure A.1: Composite-mean evolution of geopotential height anomalies (shading) and horizontal wind anomalies (arrows) at 200 hPa. The green and red boxes mark the heatwave area. Only values that are statistically significant at the 95% confidence level are shown.

List of Figures

Bibliography

Ahmadalipour, A. and Moradkhani, H. (2018). Escalating heat-stress mortality risk due to global warming in the middle east and north africa (mena). *Environment International*, 117:215–225.

AL-Tamimi, Y. K., AL-Lami, A. M., AL-Shamarti, H. K. A., and AL-Maamory, S. K. (2020). Analysis of some extreme temperature indices over iraq. *MAUSAM*, 71(3):423–430.

Alexander, L. V., Zhang, X., Peterson, T. C., Caesar, J., Gleason, B., Klein Tank, A. M. G., Haylock, M., Collins, D., Trewin, B., Rahimzadeh, F., Tagipour, A., Rupa Kumar, K., Revadekar, J., Griffiths, G., Vincent, L., Stephenson, D. B., Burn, J., Aguilar, E., Brunet, M., Taylor, M., New, M., Zhai, P., Rusticucci, M., and Vazquez-Aguirre, J. L. (2006). Global observed changes in daily climate extremes of temperature and precipitation. *Journal of Geophysical Research: Atmospheres*, 111(D5).

Alexander, M. A., Bladé, I., Newman, M., Lanzante, J. R., Lau, N.-C., and Scott, J. D. (2002). The atmospheric bridge: The influence of enso teleconnections on air–sea interaction over the global oceans. *Journal of Climate*, 15(16):2205 – 2231.

Almazroui, M. (2020). Summer maximum temperature over the gulf cooperation council states in the twenty-first century: multimodel simulations overview. *Arabian Journal of Geosciences*, 13(12):477.

Ambrizzi, T. and Hoskins, B. J. (1997). Stationary rossby-wave propagation in a baroclinic atmosphere. *Quarterly Journal of the Royal Meteorological Society*, 123(540):919–928.

AMS, A. M. S. (2025). Glossary of meteorology : heat wave. `http://glossary.ametsoc.org/wiki/heatwave`.

Barnston, A. G. and Livezey, R. E. (1987). Classification, seasonality and persistence of low-frequency atmospheric circulation patterns. *Monthly Weather Review*, 115(6):1083 – 1126.

Barriopedro, D., García-Herrera, R., Ordóñez, C., Miralles, D. G., and Salcedo-Sanz, S. (2023). Heat waves: Physical understanding and scientific challenges. *Reviews of Geophysics*, 61(2):e2022RG000780.

Belušić, A., Prtenjak, M. T., Güttler, I., Ban, N., Leutwyler, D., and Schär, C. (2018). Near-surface wind variability over the broader adriatic region: insights from an ensemble of regional climate models. *Climate Dynamics*, 50(11):4455–4480.

Bonavita, M., Hólm, E., Isaksen, L., and Fisher, M. (2016). The evolution of the ecmwf hybrid data assimilation system. *Quarterly Journal of the Royal Meteorological Society*, 142(694):287–303.

Chakraborty, A. and Singhai, P. (2021). Asymmetric response of the indian summer monsoon to positive and negative phases of major tropical climate patterns. *Scientific Reports*, 11(1):22561.

Chatterjee, A., Anil, G., and Shenoy, L. R. (2022). Marine heatwaves in the arabian sea. *Ocean Science*, 18(3):639–657.

Chen, T.-C. and van Loon, H. (1987). Interannual variation of the tropical easterly jet. *Monthly Weather Review*, 115(8):1739 – 1759.

Chen, X., Zhong, Z., and Lu, W. (2017). Association of the poleward shift of east asian subtropical upper-level jet with frequent tropical cyclone activities over the western north pacific in summer. *Journal of Climate*, 30(14):5597 – 5603.

Christidis, N., Jones, G. S., and Stott, P. A. (2015). Dramatically increasing chance of extremely hot summers since the 2003 european heatwave. *Nature Climate Change*, 5(1):46–50.

Chronis, T., Raitsos, D. E., Kassis, D., and Sarantopoulos, A. (2011). The summer north atlantic oscillation influence on the eastern mediterranean. *Journal of Climate*, 24(21):5584–5596.

Coiffier, J. (2011). *Fundamentals of Numerical Weather Prediction*. Cambridge University Press.

Cullen, H. M., Kaplan, A., Arkin, P. A., and DeMenocal, P. B. (2002). Impact of the North Atlantic Oscillation on Middle Eastern Climate and Streamflow. *Climatic Change*, 55(3):315–338.

Dai, A., Genio, A. D. D., and Fung, I. Y. (1997). Clouds, precipitation and temperature range. *Nature*, 386(6626):665–666.

Du, R., Liu, C.-H., Li, X., and Lin, C.-Y. (2024). Interaction among local flows, uhi, coastal winds, and complex terrain: Effect on urban-scale temperature and building energy consumption during heatwaves. *Energy and Buildings*, 303:113763.

Dunstone, N., Smith, D. M., Hardiman, S. C., Hermanson, L., Ineson, S., Kay, G., Li, C., Lockwood, J. F., Scaife, A. A., Thornton, H., Ting, M., and Wang, L. (2023). Skilful predictions of the summer north atlantic oscillation. *Communications Earth & Environment*, 4(1):409.

Dutra, E., Johannsen, F., and Magnusson, L. (2021). Late spring and summer subseasonal forecasts in the northern hemisphere midlatitudes: Biases and skill in the ecmwf model. *Monthly Weather Review*, 149(8):2659 – 2671.

Egger, J. (1978). Dynamics of blocking highs. *Journal of Atmospheric Sciences*, 35(10):1788–1801.

El-Fandy, M. G. (1950). Effects of topography and other factors on the movement of lows in the middle east and sudan. *Bulletin of the American Meteorological Society*, 31(10):375–381.

FAO (2008). Iraq: From emergency to development – medium-term strategy for fao assistance to iraq. Accessed: 2025-06-12.

Faranda, D., Messori, G., Jezequel, A., Vrac, M., and Yiou, P. (2023). Atmospheric circulation compounds anthropogenic warming and impacts of climate extremes in europe. *Proceedings of the National Academy of Sciences*, 120(13):e2214525120.

Feitelson, E. and Tubi, A. (2017). A main driver or an intermediate variable? climate change, water and security in the middle east. *Global Environmental Change*, 44:39–48.

Fragkoulidis, G. (2022). Decadal variability and trends in extratropical rossby wave packet amplitude, phase, and phase speed. *Weather and Climate Dynamics*, 3(4):1381–1398.

Fragkoulidis, G., Wirth, V., Bossmann, P., and Fink, A. H. (2018). Linking northern hemisphere temperature extremes to rossby wave packets. *Quarterly Journal of the Royal Meteorological Society*, 144(711):553–566.

Francis, D. and Fonseca, R. (2024). Recent and projected changes in climate patterns in the middle east and north africa (mena) region. *Scientific Reports*, 14(1):10279.

Frich, P., Alexander, L. V., Della-Marta, P., Gleason, B., Haylock, M., Tank, A. M. G. K., and Peterson, T. (2002). Observed coherent changes in climatic extremes during the second half of the twentieth century. *Climate Research*, 19(3):193–212.

Gultepe, I., Sharman, R., Williams, P. D., Zhou, B., Ellrod, G., Minnis, P., Trier, S., Griffin, S., Yum, S. S., Gharabaghi, B., Feltz, W., Temimi, M., Pu, Z., Storer, L. N., Kneringer, P., Weston, M. J., Chuang, H.-y., Thobois, L., Dimri, A. P., Dietz, S. J., França, G. B., Almeida, M. V., and Neto, F. L. A. (2019). A review of high impact weather for aviation meteorology. *Pure and Applied Geophysics*, 176(5):1869–1921.

Hajat, S., Proestos, Y., Araya-Lopez, J.-L., Economou, T., and Lelieveld, J. (2023). Current and future trends in heat-related mortality in the mena region: a health impact assessment with bias-adjusted statistically downscaled cmip6 (ssp-based) data and bayesian inference. *The Lancet Planetary Health*, 7(4):e282–e290.

Hersbach, H., Bell, B., Berrisford, P., Hirahara, S., Horányi, A., Muñoz-Sabater, J., Nicolas, J., Peubey, C., Radu, R., Schepers, D., Simmons, A., Soci, C., Abdalla, S., Abellan, X., Balsamo, G., Bechtold, P., Biavati, G., Bidlot, J., Bonavita, M., De Chiara, G., Dahlgren, P., Dee, D., Diamantakis, M., Dragani, R., Flemming, J., Forbes, R., Fuentes, M., Geer, A., Haimberger, L., Healy, S., Hogan, R. J., Hólm, E., Janisková, M., Keeley, S., Laloyaux, P., Lopez, P., Lupu, C., Radnoti, G., de Rosnay, P., Rozum, I., Vamborg, F., Villaume, S., and Thépaut, J.-N. (2020). The era5 global reanalysis. *Quarterly Journal of the Royal Meteorological Society*, 146(730):1999–2049.

Hirsch, A. L. and King, M. J. (2020). Atmospheric and land surface contributions to heatwaves: An australian perspective. *Journal of Geophysical Research: Atmospheres*, 125(17):e2020JD033223. e2020JD033223 2020JD033223.

Hochman, A., Marra, F., Messori, G., Pinto, J. G., Raveh-Rubin, S., Yosef, Y., and Zittis, G. (2022). Extreme weather and societal impacts in the eastern mediterranean. *Earth System Dynamics*, 13(2):749–777.

Holton, J. R. (2004). *An Introduction to Dynamic Meteorology*. Academic Press, San Diego, CA, 4th edition. p. 10.

Horton, R. M., Mankin, J. S., Lesk, C., Coffel, E. D., and Raymond, C. (2016). A review of recent advances in research on extreme heat events. *Current Climate Change Reports*, 2:242–259.

Hoskins, B. and Woollings, T. (2015). Persistent extratropical regimes and climate extremes. *Current Climate Change Reports*, 1(3):115–124.

Huang, S., Wang, B., Wen, Z., and Chen, Z. (2021). Enhanced tropical eastern indian ocean rainfall breaks down the tropical easterly jet–indian rainfall relationship. *Journal of Climate*, 34(8):3039 – 3048.

Hurrell, J. W. (1995). Decadal trends in the north atlantic oscillation: Regional temperatures and precipitation. *Science*, 269(5224):676–679.

Hurrell, J. W. and Deser, C. (2009). North atlantic climate variability: The role of the north atlantic oscillation. *Journal of Marine Systems*, 78(1):28–41.

IPCC (2022). *The Ocean and Cryosphere in a Changing Climate: Special Report of the Intergovernmental Panel on Climate Change; Extremes, Abrupt Changes and Managing Risks*, page 589–656. Cambridge University Press.

IPCC (2023). *Annex VII: Glossary*, page 2215–2256. Cambridge University Press.

Isaksen, L., Bonavita, M., Buizza, R., Fisher, M., Haseler, J., Leutbecher, M., and Raynaud, L. (2010). Ensemble of data assimilations at ecmwf.

Jiménez-Esteve, B. and Domeisen, D. I. (2022). The role of atmospheric dynamics and large-scale topography in driving heatwaves. *Quarterly Journal of the Royal Meteorological Society*, 148(746):2344–2367.

Kautz, L.-A., Martius, O., Pfahl, S., Pinto, J. G., Ramos, A. M., Sousa, P. M., and Woollings, T. (2022). Atmospheric blocking and weather extremes over the euro-atlantic sector – a review. *Weather and Climate Dynamics*, 3(1):305–336.

Keikhosravi, Q., Khaledi, S., and Yahyavi, A. (2020). Investigating foehn phenomena in the west alborz mountains and its effect on the amount of thermal stress mountains in the vegetation cover using landsat 8 images. *Scientific- Research Quarterly of Geographical Data (SEPEHR)*, 29(113):43–56.

Keune, J., Di Giuseppe, F., Barnard, C., Damasio da Costa, E., and Wetterhall, F. (2025). Era5–drought: Global drought indices based on ecmwf reanalysis. *Scientific Data*, 12(1):616.

Kovats, R. S. and Hajat, S. (2008). Heat stress and public health: A critical review. *Annual Review of Public Health*, 29(1):41–55. PMID: 18031221.

Krichak, S. O., Breitgand, J. S., and Feldstein, S. B. (2012). A conceptual model for the identification of active red sea trough synoptic events over the southeastern mediterranean. *Journal of Applied Meteorology and Climatology*, 51(5):962–971.

Kueh, M.-T. and Lin, C.-Y. (2020). The 2018 summer heatwaves over northwestern Europe and its extended-range prediction. *Scientific Reports*, 10(1):19283.

Lang, A. L., Pegion, K., and Barnes, E. A. (2020). Introduction to special collection: "bridging weather and climate: Subseasonal-to-seasonal (s2s) prediction". *Journal of Geophysical Research: Atmospheres*, 125(4):e2019JD031833. e2019JD031833 2019JD031833.

Lavers, D. A., Simmons, A., Vamborg, F., and Rodwell, M. J. (2022). An evaluation of era5 precipitation for climate monitoring. *Quarterly Journal of the Royal Meteorological Society*, 148(748):3152–3165.

Lee, C.-Y., Camargo, S. J., Vitart, F., Sobel, A. H., and Tippett, M. K. (2018). Subseasonal tropical cyclone genesis prediction and mjo in the s2s dataset. *Weather and Forecasting*, 33(4):967 – 988.

Lehmann, J. and Coumou, D. (2015). The influence of mid-latitude storm tracks on hot, cold, dry and wet extremes. *Scientific Reports*, 5(1):17491.

Li, Y., Huang, S., and Wen, Z. (2022). The influence of the stratospheric quasi-biennial oscillation on the tropical easterly jet over the maritime continent. *Geophysical Research Letters*, 49(16):e2022GL098940. e2022GL098940 2022GL098940.

Liu, S., Huang, S., Tan, Y., Wen, Z., Chen, X., and Guo, Y. (2024). Characteristics and mechanisms of the interannual variability of the northwest–southeast shift of the tropical easterly jet's core in july. *Journal of Climate*, 37(11):3219 – 3235.

Loughnan, M. (2014). *Geodate*, 27(1):7–10.

LU, R. (2004). Associations among the components of the east asian summer monsoon system in the meridional direction. *Journal of the Meteorological Society of Japan. Ser. II*, 82(1):155–165.

Luo, B., Luo, D., Zhuo, W., Xiao, C., Dai, A., Simmonds, I., Yao, Y., Diao, Y., and Gong, T. (2023). Increased summer european heatwaves in recent decades: Contributions from greenhouse gases-induced warming and atlantic multidecadal oscillation-like variations. *Earth's Future*, 11(8):e2023EF003701. e2023EF003701 2023EF003701.

Luo, D. and Cha, J. (2012). The north atlantic oscillation and the north atlantic jet variability: Precursors to nao regimes and transitions. *Journal of the Atmospheric Sciences*, 69(12):3763 – 3787.

Madolli, M. J., Himanshu, S. K., Patro, E. R., and De Michele, C. (2022). Past, present and future perspectives of seasonal prediction of indian summer monsoon rainfall: A review. *Asia-Pacific Journal of Atmospheric Sciences*, 58(4):591–615.

Maier-Gerber, M., Fink, A. H., Riemer, M., Schoemer, E., Fischer, C., and Schulz, B. (2021). Statistical–dynamical forecasting of subseasonal north atlantic tropical cyclone occurrence. *Weather and Forecasting*, 36(6):2127 – 2142.

Malinowski, Malinowski, J. C. (2002). Iraq: A geography. Retrieved June 13, 2025.

McGregor, G. (2024). *Synoptic Scale Atmospheric Processes and Heatwaves*, pages 207–259. Springer International Publishing, Cham.

Miyakoda, K. and Sirutis, J. (1985). Extended range forecasting. In Saltzman, B., editor, *Issues in Atmospheric and Oceanic Modeling*, volume 28 of *Advances in Geophysics*, page 55–85. Elsevier.

Mofidi, A. and Zarrin, A. (2022). On the existence of summer shamal wind induced by the zagros mountains in the middle east. *Geophysical Research Letters*, 49(18):e2022GL100151. e2022GL100151 2022GL100151.

Muslih, K. D. (2014). Identifying the climatic conditions in iraq by tracking down cooling events in the north atlantic ocean in the period 3000–0 bc. *Miscellanea Geographica*, 18(3):40–46.

Nasrallah, H. A., Nieplova, E., and Ramadan, E. (2004). Warm season extreme temperature events in kuwait. *Journal of Arid Environments*, 56(2):357–371.

Neira, M., Erguler, K., Ahmady-Birgani, H., AL-Hmoud, N. D., Fears, R., Gogos, C., Hobbhahn, N., Koliou, M., Kostrikis, L. G., Lelieveld, J., Majeed, A., Paz, S., Rudich, Y., Saad-Hussein, A., Shaheen, M., Tobias, A., and Christophides, G. (2023). Climate change and human health in the eastern mediterranean and middle east: Literature review, research priorities and policy suggestions. *Environmental Research*, 216:114537.

NOAA (1998). *Monthly Global Climate Report for June 1998*. National Centers for Environmental Information (NCEI). Accessed: 2025-02-11.

Ntoumos, A., Hadjinicolaou, P., Zittis, G., and Lelieveld, J. (2020). Updated assessment of temperature extremes over the middle east–north africa (mena) region from observational and cmip5 data. *Atmosphere*, 11(8).

Pattanaik, D. R. and Satyan, V. (2000). Fluctuations of tropical easterly jet during contrasting monsoons over india: A gcm study. *Meteorology and Atmospheric Physics*, 75(1):51–60.

Perkins, S. E. (2015). A review on the scientific understanding of heatwaves—their measurement, driving mechanisms, and changes at the global scale. *Atmospheric Research*, 164:242–267.

Perrone, T. J. (1979). Winter shamal in the persian gulf.

Pothapakula, P. K., Primo, C., Sørland, S., and Ahrens, B. (2020). The synergistic impact of enso and iod on indian summer monsoon rainfall in observations and climate simulations – an information theory perspective. *Earth System Dynamics*, 11(4):903–923.

Rao, P. G., Hatwar, H. R., Al-Sulaiti, M. H., and Al-Mulla, A. H. (2003). Summer shamals over the arabian gulf. *Weather*, 58(12):471–478.

Rao, T. N., Saikranthi, K., Radhakrishna, B., and Rao, S. V. B. (2016). Differences in the climatological characteristics of precipitation between active and break spells of the indian summer monsoon. *Journal of Climate*, 29(21):7797 – 7814.

Raymond, C., Horton, R. M., Zscheischler, J., Martius, O., AghaKouchak, A., Balch, J., Bowen, S. G., Camargo, S. J., Hess, J., Kornhuber, K., Oppenheimer, M., Ruane, A. C., Wahl, T., and White, K. (2020). Understanding and managing connected extreme events. *Nature Climate Change*, 10(7):611–621.

Richardson, L. F. (1922). Weather prediction by numerical process. by lewis f. richardson. cambridge (university press), 1922. 4°. pp. xii + 236. 30s.net. *Quarterly Journal of the Royal Meteorological Society*, 48(203):282–284.

Rodwell, M. J. and Hoskins, B. J. (1996). Monsoons and the dynamics of deserts. *Quarterly Journal of the Royal Meteorological Society*, 122(534):1385–1404.

Rousi, E., Kornhuber, K., Beobide-Arsuaga, G., Luo, F., and Coumou, D. (2022). Accelerated western european heatwave trends linked to more-persistent double jets over eurasia. *Nature Communications*, 13(1):3851.

Roxy, M. K., Ritika, K., Terray, P., Murtugudde, R., Ashok, K., and Goswami, B. N. (2015). Drying of indian subcontinent by rapid indian ocean warming and a weakening land-sea thermal gradient. *Nature Communications*, 6(1):7423.

Russo, S., Dosio, A., Graversen, R. G., Sillmann, J., Carrao, H., Dunbar, M. B., Singleton, A., Montagna, P., Barbola, P., and Vogt, J. V. (2014). Magnitude of extreme heat waves in present climate and their projection in a warming world. *Journal of Geophysical Research: Atmospheres*, 119(22):12,500–12,512.

Russo, S., Sillmann, J., and Fischer, E. M. (2015). Top ten european heatwaves since 1950 and their occurrence in the coming decades. *Environmental Research Letters*, 10(12):124003.

Salman, S. A., Shahid, S., Ismail, T., Chung, E.-S., and Al-Abadi, A. M. (2017). Long-term trends in daily temperature extremes in iraq. *Atmospheric Research*, 198:97–107.

Screen, J. A. and Simmonds, I. (2014). Amplified mid-latitude planetary waves favour particular regional weather extremes. *Nature Climate Change*, 4(8):704–709.

Sha, Y., Ren, X., Shi, Z., Zhou, P., Li, X., and Liu, X. (2020). Influence of the tibetan plateau and its northern margins on the mid-latitude westerly jet over central asia in summer. *Palaeogeography, Palaeoclimatology, Palaeoecology*, 544:109611.

Shaltout, M. and Eladawy, A. (2024). Unveiling marine heatwave dynamics in the persian /arabian gulf and the gulf of oman: A spatio-temporal analysis and future projections. *Deep Sea Research Part II: Topical Studies in Oceanography*, 218:105435.

Shen, B.-W., Pielke, R., Zeng, X., Cui, J., Faghih-Naini, S., Paxson, W., Kesarkar, A., Zeng, X., and Atlas, R. (2022). The dual nature of chaos and order in the atmosphere. *Atmosphere*, 13(11).

Simpson, I. R., Seager, R., Shaw, T. A., and Ting, M. (2015). Mediterranean summer climate and the importance of middle east topography. *Journal of Climate*, 28(5):1977–1996.

Singh, A., Thakur, S., and Adhikary, N. C. (2020). Influence of climatic indices (amo, pdo, and enso) and temperature on rainfall in the northeast region of india. *SN Applied Sciences*, 2(10):1728.

Smith, D. K., Renfrew, I. A., Dorling, S. R., Price, J. D., and Boutle, I. A. (2021). Sub-km scale numerical weather prediction model simulations of radiation fog. *Quarterly Journal of the Royal Meteorological Society*, 147(735):746–763.

Sowers, J., Vengosh, A., and Weinthal, E. (2011). Climate change, water resources, and the politics of adaptation in the middle east and north africa. *Climatic Change*, 104(3):599–627.

Spaeth, J. and Birner, T. (2022). Stratospheric modulation of arctic oscillation extremes as represented by extended-range ensemble forecasts. *Weather and Climate Dynamics*, 3(3):883–903.

Sun, J., Wang, H., and Yuan, W. (2008). Decadal variations of the relationship between the summer north atlantic oscillation and middle east asian air temperature. *Journal of Geophysical Research: Atmospheres*, 113(D15).

Tanarhte, M., Hadjinicolaou, P., and Lelieveld, J. (2015). Heat wave characteristics in the eastern mediterranean and middle east using extreme value theory. *Climate Research*, 63:99–113.

Thompson, V., Dunstone, N. J., Scaife, A. A., Smith, D. M., Slingo, J. M., Brown, S., and Belcher, S. E. (2017). High risk of unprecedented uk rainfall in the current climate. *Nature Communications*, 8(1):107.

Trenberth, K. E. and Hurrell, J. W. (1994). Decadal atmosphere-ocean variations in the pacific. *Climate Dynamics*, 9(6):303–319.

Tyrlis, E., Lelieveld, J., and Steil, B. (2013). The summer circulation over the eastern mediterranean and the middle east: influence of the south asian monsoon. *Climate Dynamics*, 40(5):1103–1123.

Vallis, G. K. (2017). *Atmospheric and Oceanic Fluid Dynamics: Fundamentals and Large-Scale Circulation*. Cambridge University Press, Cambridge, UK, 2nd edition. p. 5.

Varela, R., Rodríguez-Díaz, L., and deCastro, M. (2020). Persistent heat waves projected for middle east and north africa by the end of the 21st century. *PLOS ONE*, 15(11):1–18.

Ventura, S., Miró, J. R., Peña, J. C., and Villalba, G. (2023). Analysis of synoptic weather patterns of heatwave events. *Climate Dynamics*, 61(9):4679–4702.

Waha, K., Krummenauer, L., Adams, S., Aich, V., Baarsch, F., Coumou, D., Fader, M., Hoff, H., Jobbins, G., Marcus, R., Mengel, M., Otto, I. M., Perrette, M., Rocha, M., Robinson, A., and Schleussner, C.-F. (2017). Climate change impacts in the middle east and northern africa (mena) region and their implications for vulnerable population groups. *Regional Environmental Change*, 17(6):1623–1638.

Wallace, J. M. and Hobbs, P. V. (2006). *Atmospheric Science: An Introductory Survey*. Academic Press, San Diego, CA, 2nd edition. p. 23.

Wang, N., Dee, S., Hu, J., Steiger, N., and Thirumalai, K. (2024). Pdo and amo modulation of the enso–asian summer monsoon teleconnection during the last millennium. *Journal of Geophysical Research: Atmospheres*, 129(1):e2023JD039638. e2023JD039638 2023JD039638.

Wang, Y., Nordio, F., Nairn, J., Zanobetti, A., and Schwartz, J. D. (2018). Accounting for adaptation and intensity in projecting heat wave-related mortality. *Environmental Research*, 161:464–471.

Webster, P. J. and Yang, S. (1992). Monsoon and enso: Selectively interactive systems. *Quarterly Journal of the Royal Meteorological Society*, 118(507):877–926.

White, C. J., Carlsen, H., Robertson, A. W., Klein, R. J., Lazo, J. K., Kumar, A., Vitart, F., Coughlan de Perez, E., Ray, A. J., Murray, V., Bharwani, S., MacLeod, D., James, R., Fleming, L., Morse, A. P., Eggen, B., Graham, R., Kjellström, E., Becker, E., Pegion, K. V., Holbrook, N. J., McEvoy, D., Depledge, M., Perkins-Kirkpatrick, S., Brown, T. J., Street, R., Jones, L., Remenyi, T. A., Hodgson-Johnston, I., Buontempo, C., Lamb, R., Meinke, H., Arheimer, B., and Zebiak, S. E. (2017). Potential applications of subseasonal-to-seasonal (s2s) predictions. *Meteorological Applications*, 24(3):315–325.

Wirth, V., Riemer, M., Chang, E. K. M., and Martius, O. (2018). Rossby wave packets on the midlatitude waveguide—a review. *Monthly Weather Review*, 146(7):1965–2001.

WMO (2020). Wmo statement on the state of the global climate in 2019. page 44.

WMO, W. M. O. (1992). International meteorological vocabulary = vocabulaire météorologique international = vocabulario meteorológico internacional. vol:182:p:784. World Meteorological Organization.

Wolf, G., Brayshaw, D. J., Klingaman, N. P., and Czaja, A. (2018). Quasi-stationary waves and their impact on european weather and extreme events. *Quarterly Journal of the Royal Meteorological Society*, 144(717):2431–2448.

Woollings, T., Barriopedro, D., Methven, J., Son, S.-W., Martius, O., Harvey, B., Sillmann, J., Lupo, A. R., and Seneviratne, S. (2018). Blocking and its response to climate change. *Current Climate Change Reports*, 4(3):287–300.

Wu, Y. and Xue, W. (2024). Data-driven weather forecasting and climate modeling from the perspective of development. *Atmosphere*, 15(6).

Yan, Y., Liu, B., and Zhu, C. (2021). Subseasonal predictability of south china sea summer monsoon onset with the ecmwf s2s forecasting system. *Geophysical Research Letters*, 48(24):e2021GL095943. e2021GL095943 2021GL095943.

Yang, L., Liu, X., and Qian, F. (2020). Research on water thermal effect on surrounding environment in summer. *Energy and Buildings*, 207:109613.

Yu, Y., Notaro, M., Kalashnikova, O. V., and Garay, M. J. (2016). Climatology of summer shamal wind in the middle east. *Journal of Geophysical Research: Atmospheres*, 121(1):289–305.

Zaitchik, B. F., Evans, J. P., and Smith, R. B. (2007). Regional impact of an elevated heat source: The zagros plateau of iran. *Journal of Climate*, 20(16):4133 – 4146.

Zeng, Z., Yang, S., Wang, Z., Luo, H., and Deng, K. (2024). Weakened subtropical westerlies and their deflection by the tibetan plateau contribute to drying southeastern china in early spring. *Geophysical Research Letters*, 51(16):e2024GL109795. e2024GL109795 2024GL109795.

Zhang, R., Sun, C., Zhu, J., Zhang, R., and Li, W. (2020). Increased european heat waves in recent decades in response to shrinking arctic sea ice and eurasian snow cover. *npj Climate and Atmospheric Science*, 3(1):7.

Zhang, X., Hegerl, G., Zwiers, F. W., and Kenyon, J. (2005). Avoiding inhomogeneity in percentile-based indices of temperature extremes. *Journal of Climate*, 18(11):1641–1651.

Zhu, M. and Atkinson, B. W. (2004). Observed and modelled climatology of the land–sea breeze circulation over the persian gulf. *International Journal of Climatology*, 24(7):883–905.

Zhu, Q., Liu, Y., Shao, T., Luo, R., and Tan, Z. (2021). Role of the tibetan plateau in northern drought induced by changes in the subtropical westerly jet. *Journal of Climate*, 34(12):4955–4969.

Zittis, G., Hadjinicolaou, P., Almazroui, M., Bucchignani, E., Driouech, F., El Rhaz, K., Kurnaz, L., Nikulin, G., Ntoumos, A., Ozturk, T., Proestos, Y., Stenchikov, G., Zaaboul, R., and Lelieveld, J. (2021). Business-as-usual will lead to super and ultra-extreme heatwaves in the middle east and north africa. *npj Climate and Atmospheric Science*, 4(1):20.

Zuo, Z., Yang, S., Zhang, R., Jiang, P., Zhang, L., and Wang, F. (2013). Long-term variations of broad-scale asian summer monsoon circulation and possible causes. *Journal of Climate*, 26(22):8947 – 8961.

Acknowledgments

First and foremost, I would like to express my deepest gratitude to my supervisor, **Thomas Birner**, for his continuous support, guidance, and encouragement throughout my PhD journey. His dedication, constructive feedback, and willingness to share knowledge gave me the opportunity to grow academically and personally. I would also like to thank **Meteorological Institute, Ludwig Maximilians University** for providing the essential facilities, including server access and computational resources, which were crucial for my research. My sincere appreciation also goes to my home institution, **Mustansiryah University**, for granting me the fellowship and supporting my academic development. I am grateful to my research group for their valuable discussions, feedback, and collaboration, which enriched my work. Special thanks to my second supervisor, **Hella Garny**, for his insightful comments and helpful discussions. I am also thankful to **Philip Rupp**, for his significant contribution and guidance throughout the writing and publication process of the paper. I would also like to extend my thanks to **Aman Gupta**, who was the first person to help me when I arrived Munich, and whose support made a big difference at the beginning of my journey. I am very grateful to **Jonas Spaeth** for his consistent help and advice, particularly regarding the S2S aspects of my thesis. My thanks also go to **Frederik Harzer**, who was always generous with his time and knowledge in helping me solve technical and coding issues. Through my project, I had the opportunity to hold many meetings and discussions with scientists who provided valuable feedback and suggestions. I am thankful to **Edwin Gerber**, **Tiffany Shaw**, **Isla Simpson**, and **Stephan Pfahl** for their insightful comments, which enriched my research. I would like to thank **Alaa Al-Lami**, **Ali Ni'ma**, **Munya Al-Zuhairi**, **Ali Mohammed**, **Basim Al-Knani**, and **Arkan Mozan** for their assistance in obtaining the official documents related to my fellowship. Further thanks go to **Hadil Al-Shouhani** and **Sama Al-Dabbagh** for their time and effort in our discussions on circulation influences over Iraq. Last but not least, my deepest appreciation goes to my family. Their patience, love, and sacrifices have been the foundation of my journey. I know that the demands of this work led me to fall short in my responsibilities toward them; for that, I am truly sorry. I am forever grateful for their understanding and endless support, even when I could not always express it. To everyone who has supported me, directly or indirectly, throughout this journey, I offer my heartfelt thanks.